

University of Nevada, Reno

**Photoionization of the Cerium Isonuclear Sequence
and Cerium Endohedral Fullerene**

A dissertation submitted in partial fulfillment of the
requirements for the degree of Doctor of Philosophy in
Physics

by
Mustapha Habibi

Prof. Ronald A. Phaneuf/Dissertation Advisor

May, 2009



THE GRADUATE SCHOOL

We recommend that the dissertation
prepared under our supervision by

MUSTAPHA HABIBI

entitled

**Photoionization Of The Cerium Isonuclear Sequence And Cerium Endohedral
Fullerene**

be accepted in partial fulfillment of the
requirements for the degree of

DOCTOR OF PHILOSOPHY

Ronald A. Phaneuf, Ph. D., Advisor

Jeffrey S. Thompson, Ph. D., Committee Member

Peter Winkler, Ph. D., Committee Member

Paul Neill, Ph. D., Committee Member

Mohammed S. Fadali, Ph. D., Graduate School Representative

Marsha H. Read, Ph. D., Associate Dean, Graduate School

May, 2009

*To the souls of my mother and my father, to my beloved wife
and daughters,
to all my family, friends and colleagues for their love and
unconditional support.*

Abstract

This dissertation presents an experimental photoionization study of the cerium isonuclear sequence ions in the energy range of the 4d inner-shell giant resonance. In addition, single and double photoionization and photofragmentation cross sections of the cerium endohedral ion $\text{Ce}@C_{82}^+$ were also measured and studied in the 4d excitation-ionization energy range of cerium. Relative and absolute cross-section measurements were performed at undulator beamline 10.0.1 of the Advanced Light Source (ALS) for nine parent cerium ions: $\text{Ce}^+ - \text{Ce}^{9+}$. Double-to-single ionization cross-section ratios were measured for photoionization of the endohedral $\text{Ce}@C_{82}^+$ and empty fullerene C_{82}^+ molecular ions. The merged ion and photon beams technique was used to conduct the experiments. Multiconfiguration Hartree-Fock calculations were performed as an aid to interpret the experimental data. Four Rydberg series for $4d \rightarrow nf$ ($n \geq 4$) and $4d \rightarrow np$ ($n \geq 6$) autoionizing excitations were assigned using the quantum defect theory for the Ce^{3+} photoionization cross section. The experimental data show the collapse of the nf wavefunctions ($n \geq 4$) with increasing ionization stage as outer-shell electrons are stripped from the parent ion. The nf orbital collapse occurs partially for Ce^{2+} and Ce^{3+} ion and completely for Ce^{4+} , where these wavefunctions penetrate the core region of the ion. A strong contribution to the

total oscillator strength was observed in the double and triple photoionization channels for low charge states (Ce^+ , Ce^{2+} , and Ce^{3+}), whereas most of the 4d excitations of the higher charge states decay by ejection of one electron.

Acknowledgements

To accomplish a Ph.D. degree was one of the greatest dreams of my parents, I hope from the deepest of my heart that I have fulfilled their wish and that they are proud of me. It has been a privilege and a great opportunity to work under the supervision of Doctor Phaneuf, who was always patient and effectively present when I needed help and advice, especially during experiments and while I was writing this dissertation. Thank you Ron for your continuous support and encouragements over the course of this work. I would like to express my gratitude to many people without whom this work would not have come to light. Thank you Dr. David A. Kilcoyne at the ALS; I really appreciate your help, continuous support and valuable advice. Thank you Dr. Alejandro Aguilar at the ALS for your help and support. Thank you Dr. Alfred Müller from Giessen for your help, support and tremendous effort in analyzing the cerium endohedral data. Special thanks to Dr. Stefan Schippers from Giessen for his ORIGIN macros which allowed me to do a more efficient analysis of the data in much less time it would have taken without these macros. Special thanks are due also to Dr. Ulyana Safronova for her Hartree-Fock and relativistic many body perturbation theory calculations which helped a lot in analyzing the experimental data. I thank all my present and past research group members in the

physics department at UNR; Dr. Ronald A. Phaneuf, Dr. Mohammad F. Gharaibeh, Dr. Miao Lu, Dr. Ghassan A. Alna'washi, David A. Esteves and Jing C. Wang, for helping me in performing the experiments and learning the merged-beams technique. I would like to thank the members serving on my committee: Dr. Jeffrey S. Thompson, Dr. Peter Winkler, Dr. Paul Neill and Dr. M. Sami Fadali. Finally, I thank my family and especially my beloved wife for struggling along this journey with me. Thank you for all your love, and unconditional support.

Reno, Nevada

Mustapha Habibi

May, 2009

Table of Contents

Abstract	i
Acknowledgements	iii
Table of Contents	vi
List of Tables	vii
List of Figures	ix
1 Introduction	1
1.1 Motivations and Objectives	1
1.2 Preceding Experimental Efforts	2
1.3 Organization of Dissertation	3
2 Theoretical background	6
2.1 Introduction	6
2.2 Giant Resonance	6
2.3 Photoionization Cross Section and Oscillator Strength	7
2.4 Quantum Defect Theory	10
2.5 Hartree-Fock Method	11
3 Undulator Beamline 10.0.1 and the Experimental Techniques	14
3.1 Introduction	14
3.2 Synchrotron Radiation	15
3.2.1 ALS Beamline 10.0.1	16
3.2.2 Energy Calibration	18
3.3 Merged-Beams Apparatus	20
3.3.1 ECR Ion Source	20
3.3.2 Merged-Beams Technique	23
3.3.3 Absolute Cross-Section Measurements	25

3.3.4	Uncertainty Analysis	29
4	Ce⁺ Photoionization Measurements	31
4.1	Introduction	31
4.2	Single Photoionization of Ce ⁺	31
4.3	Double Photoionization of Ce ⁺	33
4.4	Triple Photoionization of Ce ⁺	34
4.5	Quadruple Photoionization of Ce ⁺	35
5	Ce²⁺ Photoionization Measurements	39
5.1	Introduction	39
5.2	Ce ²⁺ Single Photoionization	40
5.3	Ce ²⁺ Double Photoionization	41
5.4	Ce ²⁺ Triple Photoionization	42
6	Ce³⁺ Photoionization Measurements	46
6.1	Introduction	46
6.2	Single Photoionization of Ce ³⁺	46
6.3	Double Photoionization of Ce ³⁺	49
7	Ce⁴⁺ Photoionization Measurements	53
7.1	Introduction	53
7.2	Single Photoionization of Ce ⁴⁺	53
7.3	Double Photoionization of Ce ⁴⁺	56
7.4	Comparison with Hartree-Fock Calculations	57
8	Photoionization Measurements for Ce⁵⁺, Ce⁶⁺, and Ce⁷⁺	61
8.1	Introduction	61
8.2	Ce ⁵⁺ Photoionization Measurements	62
8.3	Ce ⁶⁺ Photoionization Measurements	63
8.4	Ce ⁷⁺ Photoionization Measurements	65
8.5	Analysis and Discussion	66
9	Photoionization Measurements for Ce⁸⁺ and Ce⁹⁺	69
9.1	Introduction	69
9.2	Ce ⁸⁺ Photoionization Measurements	69
9.3	Ce ⁹⁺ Photoionization Measurements	73
10	Photoionization and Photofragmentation Measurements of Endohedral Ce@C₈₂⁺	78
10.1	Introduction	78
10.2	Ce@C ₈₂ ⁺ Single Photoionization Measurements	79

10.3 Ce@C ₈₂ ⁺ Double Photoionization Measurements	84
10.4 Ce@C ₈₂ ⁺ Photofragmentation Measurements	86
11 Summary, Conclusions and Future Outlook	88
11.1 Summary and Conclusions	88
11.1.1 Cerium Ions	88
11.1.2 Cerium Endohedral Fullerene	91
11.2 Outlook	92
References	95
Publications	104

List of Tables

1.1	Photoionization measurements of positively charged ions in the 4d excitation region.	4
3.1	Ruling densities and photon energy ranges for the three gratings on BL 10.0.1.	18
3.2	Photon energy calibration for the Middle Energy Grating.	19
3.3	Typical experimental parameters for absolute photoionization cross-section measurements.	27
3.4	Typical uncertainties in spectroscopy and absolute modes for cross-section measurements.	30
4.1	Oscillator strengths (f) of the different photoionization channels of the La-like Ce^+	37
5.1	Ground state and metastable states of the Ba-like Ce^{2+}	40
5.2	Oscillator strengths of the three photoionization channels of the Ba-like Ce^{2+}	44
6.1	Typical cross-section measurements parameters for photoionization of Ce^{7+} at 136.65 eV.	51
7.1	Oscillator strengths (f) of the two photoionization channels of the Xe-like Ce^{4+}	59
8.1	Ground state and metastable states of the Te-like Ce^{6+}	63
8.2	Ground state and metastable states of the Sb-like Ce^{7+}	65

8.3	Comparison of Lorentzian fits to the photoionization cross sections of Ce^{5+} , Ce^{6+} , and Ce^{7+}	67
9.1	Ground state and metastable states of Sn-like Ce^{8+}	70
9.2	Ground state and metastable states of In-like Ce^{9+}	73
11.1	Summary of energy ranges and resolutions of cerium ions experiments.	90

List of Figures

2.1	photoionization cross section profiles	9
3.1	Schematic drawing of the IPB endstation	15
3.2	Schematic layout of the ALS	16
3.3	Schematic layout of Beamline 10.0.1 at the ALS.	17
3.4	Schematic drawing of the ECR ion source at the IPB endstation	20
3.5	Axial magnetic field intensity in the vicinity of the plasma chamber	21
3.6	Radial magnetic field configuration of the ECR	21
3.7	Schematic drawing of the ECR ion source and vacuum at the IPB endstation	24
3.8	Typical beam-intensity profiles for absolute photoionization cross-section measurements.	26
3.9	NIST-calibrated quantum efficiencies and measured photon flux ratios of the AXUV and SXUV photodiodes used for the photoionization measure- ments with cerium ions	28
4.1	Experimental single photoionization of Ce^+	32
4.2	Experimental double photoionization of Ce^+	33
4.3	Experimental triple photoionization of Ce^+	35
4.4	Experimental quadruple photoionization of Ce^+	36
4.5	The total experimental photoionization cross section of Ce^+	38
5.1	Single photoionization cross section of Ce^{2+}	41
5.2	Double photoionization cross section of Ce^{2+}	42
5.3	Triple photoionization cross section of Ce^{2+}	43
5.4	Total photoionization cross section of Ce^{2+}	45

6.1	Experimental single photoionization cross section of Ce^{3+}	47
6.2	Rydberg fits for the single photoionization cross section of Ce^{3+}	48
6.3	Experimental double photoionization cross section of Ce^{3+}	49
6.4	Rydberg fits for the double photoionization cross section of Ce^{3+}	50
6.5	Experimental double photoionization cross section of Ce^{3+}	52
7.1	Single photoionization cross section of Ce^{4+}	54
7.2	4d→4f transitions in the single photoionization of Ce^{4+} metastable states and 4d→6p transitions in the single photoionization of Ce^{4+} ground-state	55
7.3	4d→5f transitions in the single photoionization of Ce^{4+} ground-state . . .	57
7.4	Double photoionization cross section of Ce^{4+}	58
7.5	Comparison of experimental and calculated single photoionization cross sections of Ce^{4+}	60
8.1	Single photoionization cross-section of Ce^{5+}	62
8.2	Single photoionization cross-section of Ce^{6+}	64
8.3	Single photoionization cross-section of Ce^{7+}	66
8.4	Comparison of the photoionization cross sections of Ce^{5+} , Ce^{6+} , and Ce^{7+}	68
9.1	Single photoionization cross section of Ce^{8+}	71
9.2	Comparison of high and low energy resolutions photoionization cross sec- tions of Ce^{8+}	72
9.3	Photoionization cross-section measurements of Ce^{9+} at 0.1 eV energy res- olution	74
9.4	Photoionization cross-section of Ce^{9+}	75
9.5	Comparison of high and low energy resolutions photoionization cross sec- tions of Ce^{9+}	76
10.1	Contamination in the $\text{Ce}@C_{82}^+$ endohedral fullerene beam	80
10.2	Single photoionization cross-section measurements for $\text{Ce}@C_{82}^+$	81
10.3	Charge state of cerium ion inside the endohedral fullerene	82
10.4	Contribution of the single photoionization cross section of Ce^{3+} to the single photoionization excess cross section of $\text{Ce}@C_{82}^+$	83

10.5	Double photoionization cross-section measurements for $\text{Ce}@C_{82}^+$	84
10.6	Contribution of 4d excitations of Ce^{3+} to the double photoionization cross section of $\text{Ce}@C_{82}^+$	85
10.7	Photofragmentation cross-section measurements for $\text{Ce}@C_{82}^+$	87
11.1	Total photoionization cross sections for the cerium isonuclear sequence from Ce^+ through Ce^{9+}	94

Chapter 1

Introduction

1.1 Motivations and Objectives

The experimental study of the nature and character of atoms and ions has always been a challenge for scientists. Photoionization experiments on multiply-charged ions are important as probes of electronic correlation and relativistic effects along isonuclear and isoelectronic series, and provide data to benchmark atomic theory and models in plasma physics and astrophysics. Presented in this thesis is an experimental investigation over a wide range of charge states of multiply-charged cerium ions. The focus of this investigation was photoionization processes involving 4d electrons along the isonuclear series of cerium ions. The objective was to provide as complete a picture as possible of the ion charge-state dependences of the observed features in the photon energy range of 4d electron excitation and ionization.

Photoionization data for members of the lanthanide group (atomic numbers Z from 57 to 71) are of increasing astrophysical interest in connection with studies of nucleosynthesis and star formation, since a considerable number of lines belong to the third spectrum (doubly-charged ions), corresponding to the dominant charge state in hot, chemically

peculiar (CP) stars [5]. Cowley reported in 1976 that cerium is the most abundant lanthanide element in the so-called Ap stars [5, 21], which emit strong spectral lines of metallic elements. In 1997, Bord, Cowley and Norquist considered the abundance of cerium in the spectrum of the silicon star HD 200311 and performed the first quantitative study of the Ce^{2+} spectrum [14].

1.2 Preceding Experimental Efforts

Photoionization experiments on several isoelectronic and isonuclear sequences were conducted during the last thirty years to study systematics of electron correlation and relativistic effects in the photon energy region of 4d inner-shell excitation of atoms and atomic ions with different numbers of electrons in their outer shells. Photoionization cross-section measurements for Ba, Ba^+ and Ba^{2+} ions were performed by Lucatorto *et al.* at the National Bureau of Standards using the dual laser plasma (DLP) technique [37]. They concluded that most of the 4d absorption oscillator strengths of Ba and Ba^+ are in the continuum, whereas the Ba^{2+} cross section is dominated by strong discrete transitions. Bizau and his research team studied the Ba^{q+} ($q = 2 - 6$) and Xe^{q+} ($q = 3 - 7$) isonuclear sequences using a merged-beams technique at the SuperACO synchrotron light source in France and the Miyake undulator beam line in Denmark [7 - 12]. Their measurements indicate a dominance of discrete resonances for Ba^{4+} . O'Sullivan and collaborators have measured the 4d photoabsorption of I^{q+} ions ($q = 0 - 2$) using the DLP technique [38], concluding that the dominant features arise from $4d \rightarrow \epsilon f$ excitation

manifested by a shape resonance in neutral iodine, and from $4d \rightarrow nf$ discrete transitions in I^{2+} . The isonuclear sequence of Cs through Cs^{4+} was studied by Cummings *et al.* using the DLP technique [22]. Absolute photoionization cross-section measurements for Xe^{4+} , Xe^{5+} and Xe^{6+} ions were performed at the Advanced Light Source (ALS) in Berkeley by Aguilar *et al.* using the ion-photon merged-beams technique in support of the development of an extreme ultraviolet lithography light source at a wavelength of 13.5 nm.

Table 1.1 summarizes the photoionization experiments performed with positively-charged ions in the 4d excitation region. Most of the experimental work related to 4d-shell excitation region focused on xenon and xenon-like ions.

1.3 Organization of Dissertation

The organization of this dissertation is as follows. Chapter 2 presents brief descriptions of the photoionization process and of two theoretical methods that were applied to interpret the measurements; the quantum defect theory and the Hartree-Fock approximation. Chapter 3 describes the technique of merging counter-propagating beams of multiply-charged cerium ions and monochromatized synchrotron radiation to determine photoionization cross sections. Chapters 4 through 9 present and analyze photoionization cross-section measurements for Ce^{q+} ions ($q = 1 - 9$). Measurements of 4d excitation of an encapsulated cerium atom inside a C_{82}^+ fullerene molecular ion cage are presented in Chapter 10. Finally, a summary of this work, conclusions and an outlook for the future are presented in Chapter 11. An appendix contains publications of photoionization work

Table 1.1: Photoionization measurements for positively-charged ions in the 4d excitation region, in increasing chronological order.

Target (eV)	Energy Range (eV)	Reference	Publication year
Ba ⁺ , Ba ²⁺	85-150	[37]	1981
La ³⁺	95-140	[51]	1995
Ba ⁺	90-143	[52]	1995
I ⁺ , I ²⁺	60-150	[38]	1996
Xe ⁺	60-150	[55]	1996
Xe ⁺ , Ba ⁺ , Eu ⁺	60-160	[53]	1996
Xe ²⁺	52-150	[56]	1998
Xe ⁴⁺ - Xe ⁷⁺	55-160	[10]	2000
Sb ⁺ - Sb ⁴⁺	30-100	[46]	2000
I ⁺ , I ²⁺	45-140	[47]	2000
Cs ⁺ - Cs ⁴⁺	80-160	[22]	2001
Xe ⁺ - Xe ²⁺	50-130	[1]	2001
Xe ⁺	80-140	[49]	2001
Ba ²⁺ - Ba ⁶⁺	95-150	[7]	2001
Cs ⁺ , Ba ⁺ , Ba ²⁺	40-185	[50]	2002
Sm ²⁺	100-170	[12]	2003
Eu ⁺	130-145	[54]	2005
Xe ³⁺	37.5-115	[48]	2005
Xe ³⁺ - Xe ⁶⁺	30-160	[11]	2006
Xe ⁴⁺ - Xe ⁶⁺	89-117	[45]	2006

in which the author of this dissertation has participated.

Chapter 2

Theoretical background

2.1 Introduction

Ionization of atoms and molecules by photons is a dominant process in the universe. In many systems, the photoionization process is a fundamental probe of their properties and structures. Since the development of the theory of the photoelectric effect by Einstein in 1891, for which he received the Nobel prize, the quantum theory began to flourish and succeeded to explain most of the physical phenomena that were unexplainable by classical physics theories. The theory of the dual particle-wave nature of light opened more interesting windows for investigation of matter and light interactions.

2.2 Giant Resonance

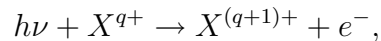
The term "giant resonance" originates from nuclear physics. Giant resonances in nuclei were observed for the first time by Baldwin and Klaiber in 1947 in measurements of x-ray photon-induced fission [70, 71]. In atomic physics, the origin of giant resonances is the collective excitation of an entire electron subshell, which was first observed in photoexcitation of solids [72, 73]. These autoionizing excitations are characterized by a

strong oscillator strength that depends on the occupancy of the subshell being excited. Excitation of a filled 4d subshell, for example, exhibits a broad asymmetric $4d \rightarrow \epsilon f$ resonance for neutral atoms and low-charge-state ions, as observed in photoionization of Xe [74]. Below the 4d threshold, strong and narrow $4d \rightarrow nf$ and $4d \rightarrow np$ resonances can occur for higher charge states depending on the atomic number Z of the ion. In molecular physics, giant resonances have been observed in the photoionization of fullerenes, hollow closed-shell molecules composed solely of carbon atoms. Two distinct resonances attributed to electric-dipole-excited collective electron oscillation modes were observed in these molecules. A strong surface plasmon resonance occurs at a photon energy near 21 eV for the C_{60}^+ molecular ion. A second resonance attributed to a volume plasmon excitation occurs near 41 eV [41].

2.3 Photoionization Cross Section and Oscillator Strength

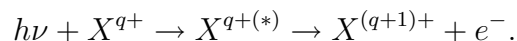
The binding energy of an electron in an atom or molecule is the minimum energy required to free that electron from the Coulomb potential well due to the nucleus and neighboring electrons, i.e. to ionize it. The ionization potential of an atom, molecule, or ion is the binding energy of an electron in the ground or lowest occupied energy level. Photoionization can result from absorption of a photon by an atomic or molecular system, if the photon energy exceeds the ionization potential. Two processes could be involved in this interaction. Direct or non-resonant photoionization is the consequence of the absorption of a photon whose energy matches or exceeds the binding energy of the electron being

ejected from the atom or the ion. For positive ions, this process is manifested as a step-function rise of the photoionization cross section at the threshold or minimum photon energy, falling off monotonically with increasing photon energy. Direct photoionization may be represented by the following pathway:



where h is Planck's constant and ν is the photon frequency.

Indirect or resonant photoionization may result from excitation of a core electron to a discrete state whose energy is greater than the ionization potential. In this case, the photon energy must match the energy difference between the initial and final states, so it is a resonant process. There is a high probability that such a multiply-excited system will minimize the excess energy by a so-called Auger or autoionization process in which one or more electrons may be ejected. This process is manifested in the cross section as a resonance and may be represented as follows:



Interference may occur if both resonant and direct photoionization channels at a certain photon energy have the same final state. In this case, an asymmetric Fano-Beutler line profile for the resonance [60, 61] will be produced. More details about interference effects are given in reference [67]. These processes are illustrated in Figure 2.1.

The photoionization cross section σ in megabarns ($1\text{Mb} = 10^{-18}\text{cm}^2$) is given in terms

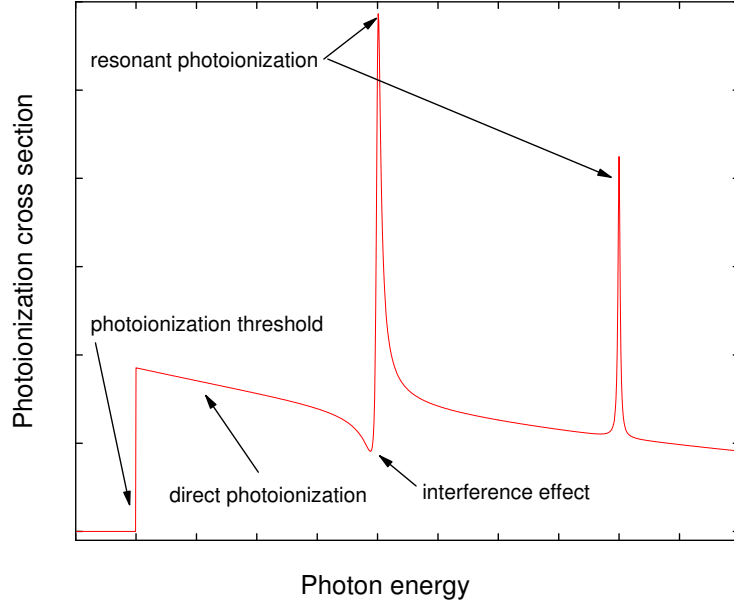


Figure 2.1: Generic photoionization cross section.

of the differential oscillator strength per unit energy df/dE (eV^{-1}) by [69]:

$$\sigma(E) = (2\pi a_o)^2 \alpha R \frac{df}{dE} = 109.7618 \frac{df}{dE}, \quad (2.3.1)$$

where a_o is the Bohr radius, α is the fine structure constant, and R is the Rydberg constant. The weighted oscillator strength of an electron transition between two quantum states $|i\rangle$ and $|f\rangle$ is given by:

$$gf = (2J_i + 1)f_{if} = \frac{1}{3R}(E_f - E_i) \left| \langle i | -e \sum_{k=1}^N \mathbf{r}_k | f \rangle \right|^2, \quad (2.3.2)$$

where J_i and $(2J_i+1)$ are the total angular momentum and the statistical weight of the initial state, respectively. The integral (in brackets) represents the reduced matrix element of the electric dipole moment, of which the squared value yields the electric dipole line strength. N is the number of electrons in the system. Integrating the cross

section σ (Mb) in equation 2.3.1 between two energies E_1 and E_2 (eV) yields the average oscillator strength \bar{f}_{12} :

$$\bar{f}_{12} = 9.1106 \times 10^{-3} \int_{E_1}^{E_2} \sigma(E) dE. \quad (2.3.3)$$

This formula was used to calculate the total photoionization oscillator strengths for the cerium ions reported in this dissertation. According to the Thomas-Reiche-Kuhn sum-rule, the total oscillator strength of the transitions originating from the 4d subshell of the cerium ions is equal to the number of electrons populating it, which is ten. Photo-excitation of an electron is governed in the LS -coupling scheme by the following selection rules:

$$\Delta S = 0,$$

$$\Delta L = 0 \text{ or } \pm 1, \text{ and } L_i + L_f > 0,$$

$$\Delta J = 0 \text{ or } \pm 1, \text{ and } J_i + J_f > 0,$$

$$\Delta \pi = \pm 1.$$

S , L and J are the spin, orbital and total angular momenta, respectively, and π is the parity operator. The last rule is a consequence of the odd parity of the electric dipole operator.

2.4 Quantum Defect Theory

Quantum defect theory is based on a hydrogenic model where an electron far enough from the nucleus (large r) experiences a Coulomb potential equivalent to that exerted by an effective point charge at the nucleus. The effective Coulomb potential resulting from

the screening of the nuclear charge Ze by the N_c core electrons, is given by:

$$V_{eff}(r) = \frac{-(Z - N_c)e^2}{r} \quad (2.4.1)$$

More discussion and details concerning this theory are given by Seaton in reference [42].

The analysis of the Ce^{3+} photoionization cross section in Chapter 6 was based on the quantum defect form of the Rydberg formula:

$$E_n = E_{limit} - \frac{R_{Ce}(Z - N_c)^2}{(n - \delta_n)^2}, \quad (2.4.2)$$

where E_n is the transition energy, E_{limit} is the ionization potential of the electron being excited to the corresponding final state ($n = \infty$), Ze is the nuclear charge, and N_c is the number of the core electrons. The dimensionless quantum defect parameter δ_n is a measure of the departure of the energy level E_n from a pure hydrogenic value for which $\delta_n = 0$ and accounts for the finite size of the non-hydrogenic ion core, which is significant for the cerium isonuclear sequence. The Rydberg constant R_{Ce} for cerium ions is given by

$$R_{Ce} = \frac{\mu e^4}{4\pi\hbar c}, \quad (2.4.3)$$

where $\mu = (1/m_e + 1/M_{Ce})^{-1}$ is the reduced mass of the electron-nucleus system of the cerium ion, e and m_e are the charge and the mass of the electron, respectively, \hbar is the reduced Planck constant, and M_{Ce} is the mass of the cerium ion nucleus.

2.5 Hartree-Fock Method

Identification of the resonant features in the measured photoionization cross sections requires knowledge of the electronic energy levels of the ion. Computer codes based on

the Hartree-Fock approximation are readily available to calculate the energies of these levels, and one was used [28] to interpret the measurements in this dissertation.

Based on the approximation of an average central potential created by the nucleus and the ion core, and the exchange interaction between electrons, the Hartree-Fock method is widely used to solve the many-electron problem. This leads to an effective quantum-mechanical description in which the many-electron problem is reduced to solving a number of coupled single-particle equations. The total wavefunction of the system described by N one-electron spin-orbitals $\psi_i(x_j)$ is given by a Slater determinant:

$$\psi = \frac{1}{\sqrt{N!}} \begin{vmatrix} \psi_1(x_1) & \psi_1(x_2) & \dots & \psi_1(x_N) \\ \psi_2(x_1) & \psi_2(x_2) & \dots & \psi_2(x_N) \\ \vdots & \vdots & \vdots & \vdots \\ \cdot & \cdot & \cdot & \cdot \\ \psi_N(x_1) & \psi_N(x_2) & \dots & \psi_N(x_N) \end{vmatrix} \quad (2.5.1)$$

This determinant is antisymmetric under particle exchange, taking into consideration the Pauli exclusion principle which states that no two electrons can have the same quantum numbers and occupy the same state simultaneously. A variational principle is used to minimize the expectation value of the total Hamiltonian with respect to the single-electron wavefunctions ψ_i ,

$$\frac{\delta}{\delta\psi_i} \left[\langle H \rangle - \sum_j \varepsilon_j \int |\psi_j|^2 dr \right] = 0, \quad (2.5.2)$$

where H is the Hamiltonian of the system and ε_j are Lagrange multipliers representing the electron binding energies and resulting from the normalization condition imposed on the ψ_i wavefunctions. These calculations lead to a set of N one-electron equations, called

the Hartree-Fock equations:

$$\left(\frac{-p_i^2}{2m} - \frac{Ze^2}{r} + \sum_j e^2 \int d\mathbf{r}' \frac{|\psi_j(\mathbf{r}')|^2}{|\mathbf{r} - \mathbf{r}'|} \right) \psi_i(\mathbf{r}) - \sum_j \delta_{\sigma_i \sigma_j} e^2 \int d\mathbf{r}' \frac{\psi_j^*(\mathbf{r}') \psi_i(\mathbf{r}')}{|\mathbf{r} - \mathbf{r}'|} \psi_j(\mathbf{r}) = \varepsilon_i \psi_i(\mathbf{r}) \quad (2.5.3)$$

where \mathbf{r} and \mathbf{r}' are the position vectors of the electrons. The first and second terms in the left-hand side of this equation represent the electron kinetic energy and the electron-nucleus Coulomb interaction, respectively. The third term represents the electron-electron Coulomb potential and the last term, known as the exchange term, is non-zero only when electrons with the same spin σ_i are considered. The exchange term makes the Hartree-Fock equations hard to solve in most cases. The central field approximation allows a separation of the orbital component of the wavefunction into radial and angular parts. The one-electron equations are then solved by a self-consistent method.

Chapter 3

Undulator Beamline 10.0.1 and the Experimental Techniques

3.1 Introduction

The photoionization cross-section measurements reported in this dissertation were performed using a merged-beams apparatus. Details of this technique are given in this chapter. Figure 3.1 presents a schematic layout of the ion-photon-beam (IPB) endstation at the Advanced Light Source (ALS). Multicharged cerium ions were produced in an electron cyclotron resonance (ECR) ion source, then extracted from the ion source by a potential difference of 4kV or 6 kV, electrostatically steered and focused. A 60° magnetic-dipole mass spectrometer selected ions from the beam according to their mass-per-charge ratio. The ion beam was then merged onto the axis of a counter-propagating beam of monochromatized synchrotron radiation by a 90° spherical electrostatic deflector. The two beams were merged and interacted over a common path of 130 cm. A 45° dipole magnet demerged the primary and product ions from the photon beam and separated them according to their charges. Two types of measurements were performed with this apparatus. In spectroscopy mode, the relative yield of photoions was measured

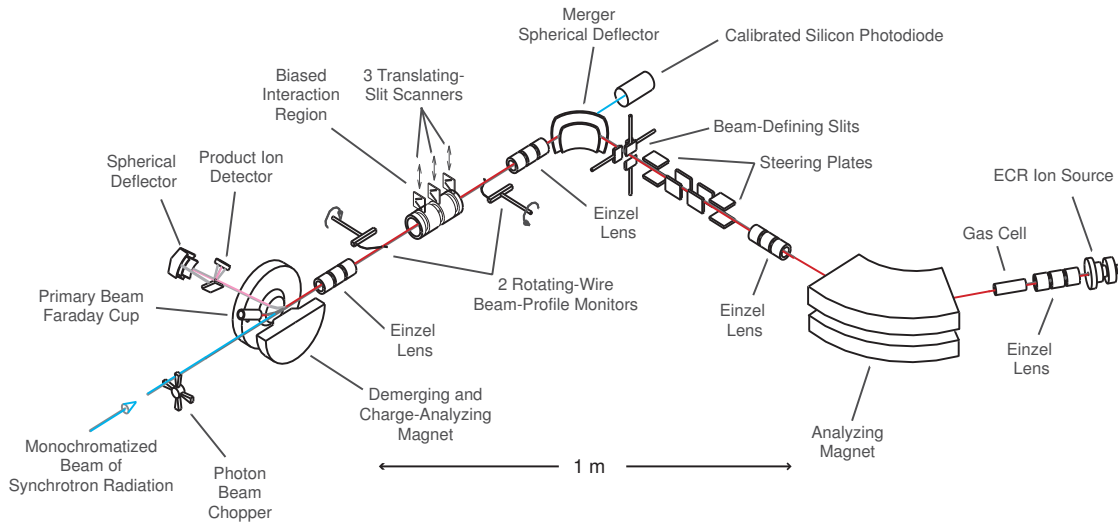


Figure 3.1: Schematic drawing of the IPB endstation at the ALS undulator beamline 10.0.1.

as the photon energy was changed in small steps. In this case, photoions produced along the entire 130-cm path were detected to optimize signal collection. In absolute mode, the photoion signal was recorded at discrete photon energies under well-characterized experimental conditions. In this case, energy-labelled product ions were detected only from a central electrically-biased interaction region of length 29.4 cm in which spatial intensity profiles of the beams were carefully measured *in situ* to quantify their overlap.

3.2 Synchrotron Radiation

Emission of synchrotron radiation is a consequence of accelerating a charged particle in a curved path. At relativistic speeds, the emitted radiation takes the form of a narrow cone tangent to the trajectory of the accelerated particle. This phenomenon occurs whenever a relativistic charged particle undergoes a change in direction while passing through a

transverse magnetic field. The theory of synchrotron radiation, established in 1946 by Schwinger [65], is the framework of most recent calculations concerning this phenomenon.

3.2.1 ALS Beamline 10.0.1

A third-generation electron synchrotron radiation source producing vacuum ultraviolet light with very high brightness and photon flux, called the Advanced Light Source, was developed at Lawrence Berkeley National Laboratory in 1994. Figure 3.2 shows a schematic layout of this light source. A thermionic gun serves as a generator of electrons which are then accelerated in bunches by a 4-meter-long linear accelerator (Linac) into a

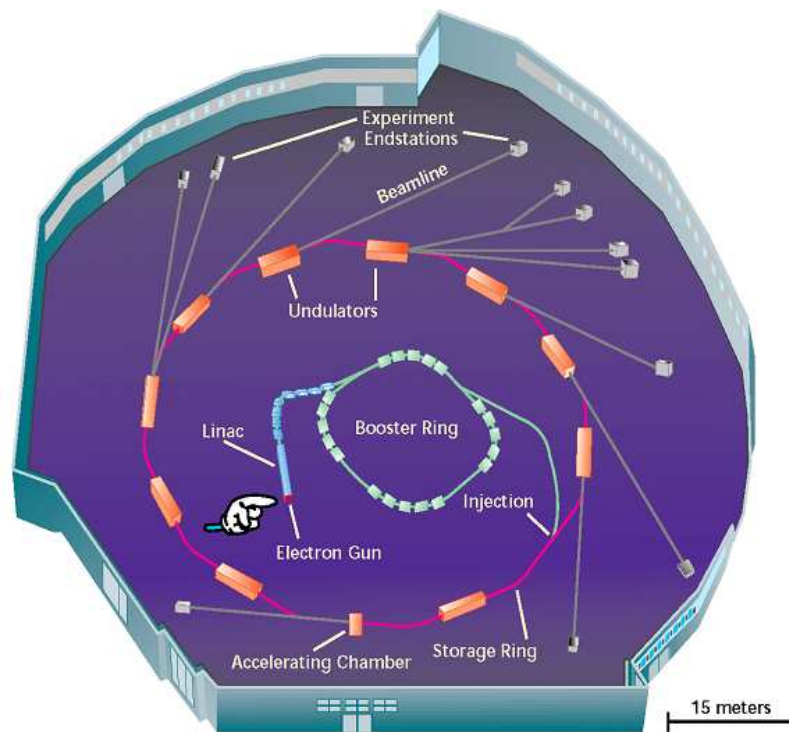


Figure 3.2: Schematic layout of the ALS showing the injection system, insertion devices and beamlines [66].

linac-to-booster transfer line at 50 MeV. The electrons are injected into the booster ring where they are accelerated to an energy of 1.5 GeV for injection into the storage ring, where they are further accelerated to 1.9 GeV and stored for periods of typically 8 hours. Various magnetic devices installed in the perimeter of the storage ring keep the electron beam on the desired trajectory with high precision. The maximum electron current in the storage ring after a refill was 0.4 A, which decayed exponentially with time to ~ 0.2 A in 8 hours.

A 4.55-meter-long undulator with a 10-cm period and 43 full periods serves beamline 10.0.1. Over a photon energy range from 17 to 360 eV, beamline 10.0.1 provides an intense photon beam of up to 10^{14} photons/s with high brightness and spectral resolution. Figure 3.3 shows a schematic layout of the beamline optical elements. Synchrotron radiation from the undulator is directed and focused horizontally by a spherical mirror (M1) then vertically by another spherical mirror (M2) with demagnification of 8 allowing the photon beam to pass through a small entrance slit. The beam diameter is typically

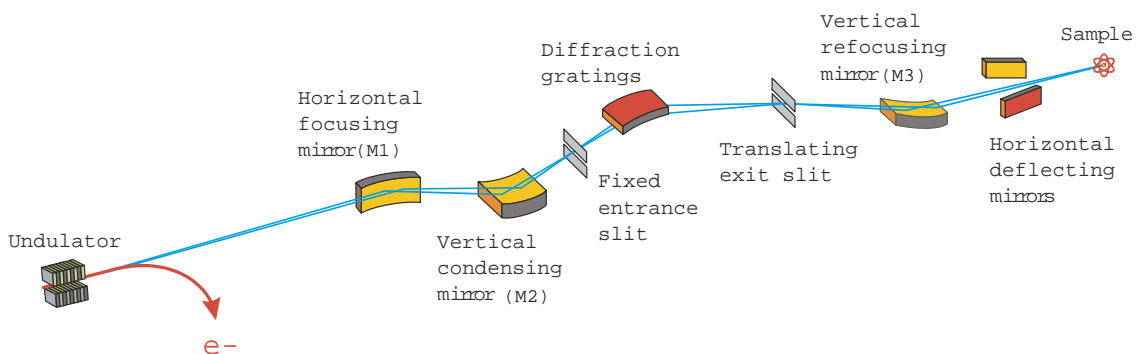


Figure 3.3: Schematic layout of Beamline 10.0.1 at the ALS [67].

Table 3.1: Ruling densities and photon energy ranges (with optimum photon flux) for the three gratings on beamline 10.0.1.

Grating	Ruling Density (lines/mm)	Energy Range (eV)
Low Energy Grating	380	17 – 75
Middle Energy Grating	925	40 – 170
High Energy Grating	2100	100 – 360

less than 1 mm.

A spherical grating monochromator (SGM) composed of a fixed-position entrance slit, three interchangeable spherical grazing-incidence gratings and a translating exit slit was designed so that the angle between the entrance and exit slits remains constant at 165° . The rulings and energy ranges for each grating are listed in Table 3.1. The photon beam energy is selected by the SGM and the photon flux is simultaneously optimized by adjusting gap between the undulator magnets. The energy resolution is determined by the SGM entrance and exit slit widths. A third spherical mirror (M3) refocuses the beam vertically and directs the monochromatized photon beam to the endstation on the beamline. References [67] and [75] contain more details about the beamline optics and synchrotron radiation.

3.2.2 Energy Calibration

The three diffraction gratings on the beamline are mechanically interchangeable, which affects the photon energy calibration that is only reproducible within approximately 0.1% each time the grating is changed. Therefore, it is necessary to accurately calibrate the photon energy scale for each experiment using well-known resonances. A gas cell isolated

Table 3.2: Photon energy references for calibration of the Middle Energy Grating.

Ions	Resonance (eV)	Calibration (eV)	Process	Apparatus	Reference
Ar	246.927	123.464	$2p_{3/2}^{-1}$ 3d, 2^{nd} order	gas cell	[76]
Ar	244.390	122.195	$2p_{3/2}^{-1}$ 4s, 2^{nd} order	gas cell	[76]
Kr	91.200	91.200	$3d_{5/2}^{-1}$ 5p	gas cell	[76]
Kr	91.200	45.600	$3d_{5/2}^{-1}$ 5p, 2^{nd} order	gas cell	[76]
Ce ⁴⁺	128.38	128.38	4d – nf	IPB	this experiment
Ce ⁴⁺	131.14	131.14	4d – nf	IPB	this experiment
Ce ⁹⁺	134.63	134.63	4d – nf	IPB	this experiment
Ce ⁹⁺	136.43	136.43	4d – nf	IPB	this experiment
Ce ⁹⁺	138.95	138.95	4d – nf	IPB	this experiment

by a thin aluminum vacuum window is installed on a different branch of the beamline and serves this purpose. A potential difference is applied between two parallel plates to collect photoionized ions from neutral gas at mTorr pressure. Well-calibrated photon-ion data taken earlier at the IPB endstation was also used to calibrate the photon energy of similar experiments performed later. Since the photon and ion beams are counter-propagating in the IPB endstation, corrections for the Doppler effect were necessary to account for the energy shift in the reference frame of the ion beam. This correction is made using the well-known Doppler formula:

$$E_{corr}^{\gamma} \approx \frac{E_{lab}^{\gamma}}{1 - v_i/c} \quad (3.2.1)$$

where E_{lab}^{γ} and E_{corr}^{γ} are the nominal and Doppler-corrected photon energies, respectively, v_i is the velocity of the ions inside the interaction region, and c is the speed of light in vacuum. Typical corrections for the present experiments ranged from 10 meV to 140 meV, depending on the ion mass and charge. Table 3.2 presents the reference energies used to

calibrate the middle energy grating. Resonances diffracted in second order by the grating provided additional calibration energies in the range of interest. The photon intensity was maximized by setting the undulator gap appropriately.

3.3 Merged-Beams Apparatus

3.3.1 ECR Ion Source

Photoionization measurements of multiply-charged positive ions were made possible using a magnetically-confined plasma device, a 10 GHz all-permanent-magnet electron-cyclotron-resonance ion source (ECRIS) [62, 63]. Figure 3.4 shows the configuration of the ECR ion source at the IPB endstation of the ALS [68]. The cyclotron motion of electrons, confined in a ‘magnetic bottle’ consisting of four permanent ring magnets and a hexapole magnet array, is resonantly excited by a microwave electromagnetic field of frequency 10 GHz. The plasma discharge is axially trapped by a magnetic mirror

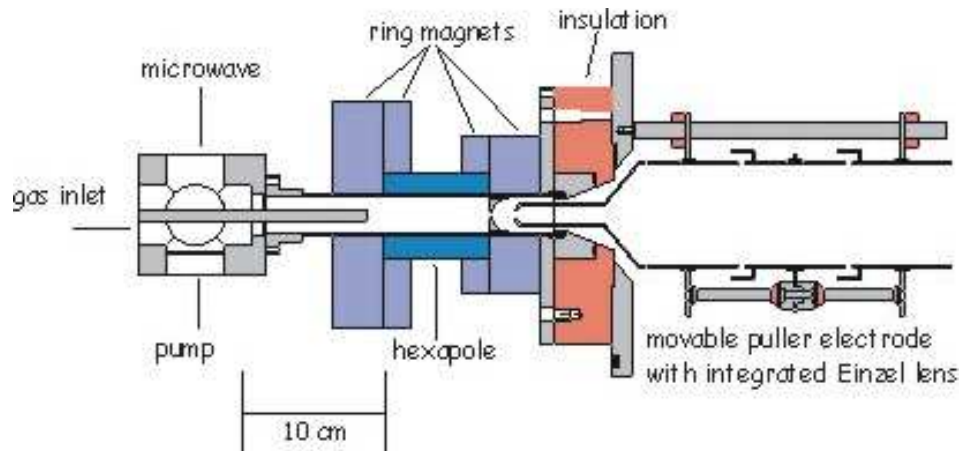


Figure 3.4: Schematic drawing of the ECR ion source at the IPB endstation at the ALS undulator beam line 10.0.1 [68].

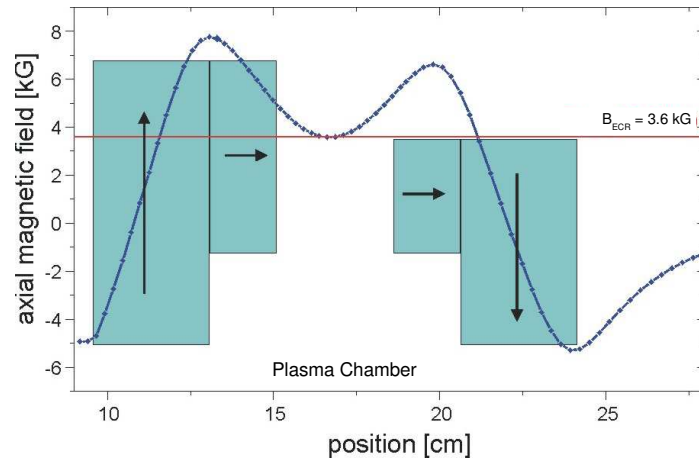


Figure 3.5: Axial magnetic field intensity in the vicinity of the plasma chamber [68].

formed by four permanent magnets; two with 16 cm outer diameter (OD), and two with 11 cm OD. The configuration of the axial magnetic field inside the cylindrical plasma chamber is shown in Figure 3.5. Radial confinement of electrons in the plasma chamber is provided by 24 permanent magnets arranged in a hexapole configuration, as shown

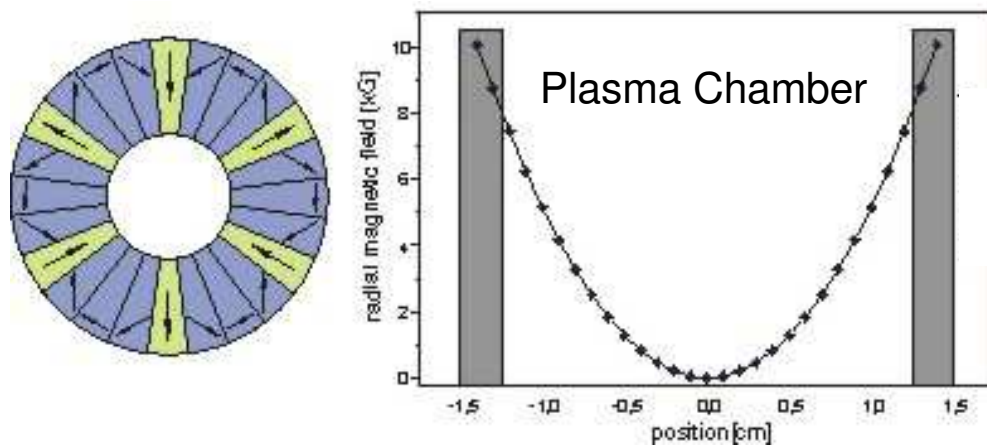


Figure 3.6: Radial magnetic field configuration and intensity inside the plasma chamber [68].

in Figure 3.6. The axial magnetic field intensity B near the mid-point of the plasma chamber was chosen to match a cyclotron resonance frequency f_{cr} for the electrons of 10 GHz :

$$B = \frac{m_e}{e} 2\pi f_{cr} = 3.576 \text{ kG}, \quad (3.3.1)$$

where e and m_e are the charge and the mass of the electron, respectively. Detailed descriptions of the production of multiply charged ions by ECR ion sources and their characteristics have been reported [29, 30, 62, 63, 64].

The electromagnetic radiation that heats the electrons at the cyclotron resonance frequency is furnished by a microwave generator system, consisting of a microwave frequency signal generator and an 8–18 GHz traveling-wave-tube amplifier with a maximum continuous-wave output power of 250 Watts. This microwave system is protected from reflected power by a magnetic circulator situated in the waveguide path. The transmitted and reflected powers are monitored by directional couplers connected to RF power meters. A commercial kapton window, transparent at 10 GHz, is used as a vacuum break between atmospheric pressure and a typical source vacuum pressure of 10^{-7} Torr. A mylar sheet of 0.2 mm thickness, also transparent at 10 GHz, is used as a voltage break to insulate the high voltage part of the ECRIS from the rectangular waveguide at ground potential. The transition from rectangular to circular waveguide is accomplished by a coupler called a ‘magic cube’. This coupler produces the TM_{01} mode inside the cylindrical waveguide connected to the plasma chamber. A translatable tuning plunger is installed on one side of the magic cube, which acts as an RF multimode cavity to optimize the coupling of the microwaves into the plasma. The ion source plasma chamber is cooled by a flow of

deionized water through the double-walled stainless-steel plasma chamber. A water flow switch is interlocked to the microwave amplifier to protect the NdFeB permanent magnets that would be irreversibly damaged by thermal demagnetization if a temperature above 40 °C were reached.

A small resistively heated oven located outside the injection end of the plasma chamber is used to evaporate non-gaseous materials into the ion source plasma discharge. Due to the extreme temperature required to evaporate metallic cerium, even at very low vapor pressure (oven power > 200 Watts to produce only a few hundred pA of ion current), a cerium metallocene powder was used for the experiments. Since it is extremely air and moisture sensitive, the Tris(cyclopentadienyl)cerium powder ($((C_5H_5)_3Ce)$) was loaded into the oven under argon gas using a glove bag. This volatile material yielded stable cerium ion beam currents of tens of nA with less than one Watt of oven power. Argon and nitrogen support gases were introduced to facilitate a stable plasma discharge. A typical oven charge of 0.5 g delivered Ce ion beams for 24 hours or more.

3.3.2 Merged-Beams Technique

The ion beam formation and transport system upstream of the analyzing magnet is shown in Figure 3.7. A mixture of positive ions from the plasma discharge passes through the extraction aperture under the effect of a strong electric field created between the plasma chamber, at positive high voltage (4 or 6 kV), and the puller electrode at ground potential. This mixture is then focused by a cylindrical einzel lens, steered and centered by four pairs of horizontal and vertical electrostatic plates. Pairs of horizontal and vertical beam

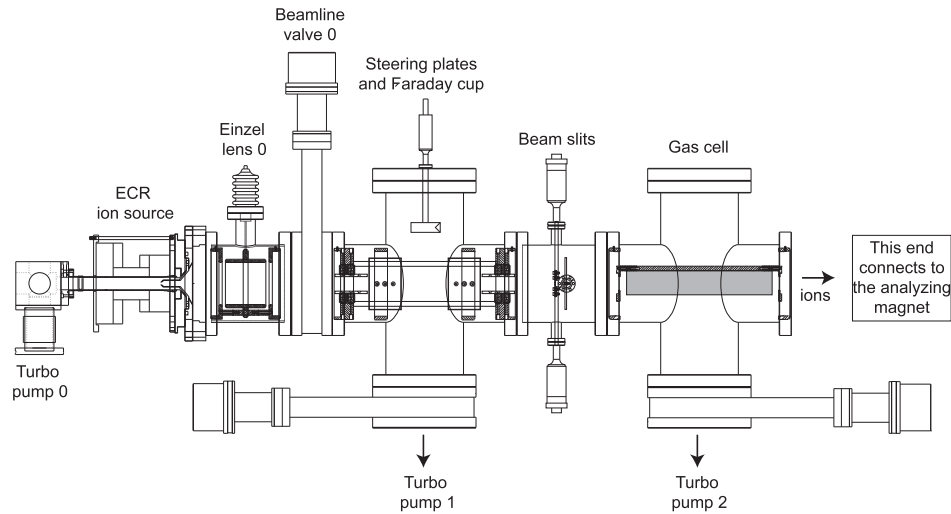


Figure 3.7: Schematic drawing of the ECR ion source and vacuum system at the IPB endstation at the ALS [67].

slits, made of razor blades, are situated upstream and downstream of a 60° dipole analyzing magnet, allowing optimization of the ion beam size and mass-per-charge resolution. A desired ion beam is selected according to its mass-per-charge ratio by the analyzing magnet, collimated and re-centered by an einzel lens and another set of four pairs of electrostatic plates. The selected ion beam is then merged by spherical electrostatic deflector plates (merger) onto the axis of a counter-propagating beam of synchrotron radiation. After interaction with the photon beam, the product and the primary ions are demerged and separated by a 45° dipole magnet, and independently collected by a primary beam Faraday cup and a single-particle photoion detector, respectively. More details about this apparatus and technique may be found in the dissertation of A. Aguilar [67].

3.3.3 Absolute Cross-Section Measurements

Among the many advantages of the merged-beams technique is the ability to measure absolute cross sections for photoionization of ions. A biased interaction region permits energy-labelling of the product ions and an accurate definition of the path along which the photon-ion interaction takes place. Depending on the primary and product ion charges, a positive or negative potential of 1–2 kV was applied to the cylindrical interaction chamber. This controlled the spatial separation of these beams in the analyzer, and thereby optimized the signal-to-background ratio and simultaneous transport of the ion beams to the detector and Faraday cup.

Absolute cross-section measurements are typically performed at a number of discrete photon energies (at least three) where, if possible, no narrow resonant features occur in the photoion-yield spectrum. Measurements of experimental parameters, which include the parent ion beam current I^+ (A), photodiode current I^γ (A) and two-dimensional form factors $F(z)$ (cm^{-2}) along the axis of the interaction region, allow determination of the absolute cross section σ_{pi} (cm^2) at a given photon energy $h\nu$ (eV):

$$\sigma_{pi}(h\nu) = \frac{S q e^2 v_i \epsilon}{I^+ I^\gamma \Omega \Delta F_L}. \quad (3.3.2)$$

S is the photoion signal count rate per second, qe is the electric charge of the parent ion (C), v_i is the velocity of the primary ions inside the interaction chamber (cm/s), ϵ is the quantum efficiency of the photodiode (number of electrons produced per incident photon), Ω and Δ are the photoion collection and detection efficiencies (both nominally = 100% for this experiment), respectively. The spatial overlap of the photon and ion

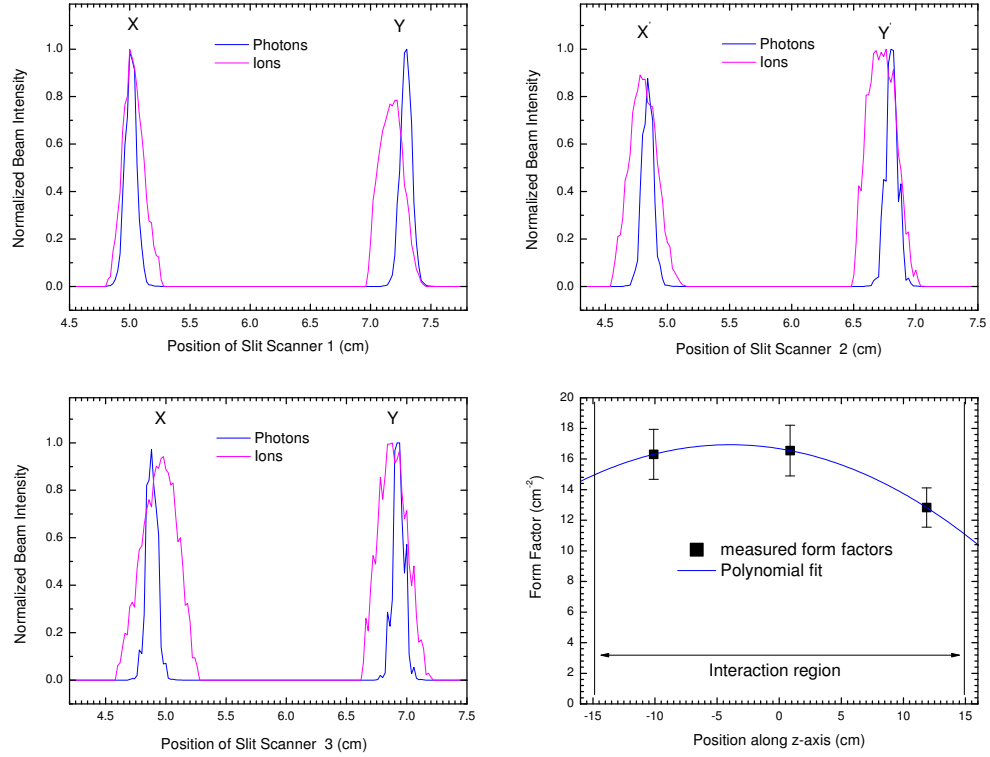


Figure 3.8: Typical beam-intensity profiles for absolute photoionization cross-section measurements.

beams is measured by three translating-slit scanners placed at the two ends and at the center of the interaction region. These scanners operate in x–y planes perpendicular to the interaction axis (z) of the beams. Each slit scanner contains two orthogonal slits of width 0.28 mm made of razor blades that measure the beam intensities along the x and y axes. Form factors $F(z_i)$ are determined at three positions along the interaction region axis (4.39 cm, 15.38 cm and 26.4 cm from the entrance aperture of the interaction chamber);

$$F(z_i) = \frac{\int \int I^+(x, y) I^\gamma(x, y) dx dy}{\int \int I^+(x, y) dx dy \int \int I^\gamma(x, y) dx dy}. \quad (3.3.3)$$

These three measured form factors are interpolated/extrapolated by an exact second

order polynomial which is then integrated analytically over the length of the interaction path to get the integral form factor F_L (cm^{-1}). Typical measured beam profiles are shown in Figure 3.8 and typical parameters for photoionization cross-section measurements are given in Table 3.3.

Table 3.3: Typical experimental parameters for absolute cross-section measurements for photoionization of Ce^{7+} at 134.65 eV photon energy and 0.1 eV resolution.

Parameter	Value
Ion mass	142 amu
Interacting ion energy	38.5 keV
Interacting ion velocity, v_i	2.304×10^7 cm/s
Ion beam current, I^+	16.3 nA
Photodiode current, I^γ	49.0 μA
Photodiode quantum efficiency, ϵ	18.77 electrons/photon
Photon flux	1.63×10^{13} photons/s
Interaction path length, L	29.4 cm
Interaction region potential, V_{int}	-1.5 kV
Ce^{8+} signal rate, S	496 s^{-1}
Form factor: F_L	355.93 cm^{-1}
Photoion collection efficiency, Ω	100%
Photoion detection efficiency, Δ	100%
Cross section, σ	1.36×10^{-16} cm^2

Accurate photon flux measurements are of critical importance in determining absolute cross sections. For this purpose, two NIST-calibrated photodiodes were used. Prior to August, 2007, an AXUV-type silicon x-ray photodiode was used for measurements. Because of a subsequently detected sensitivity loss due to prolonged exposure to the

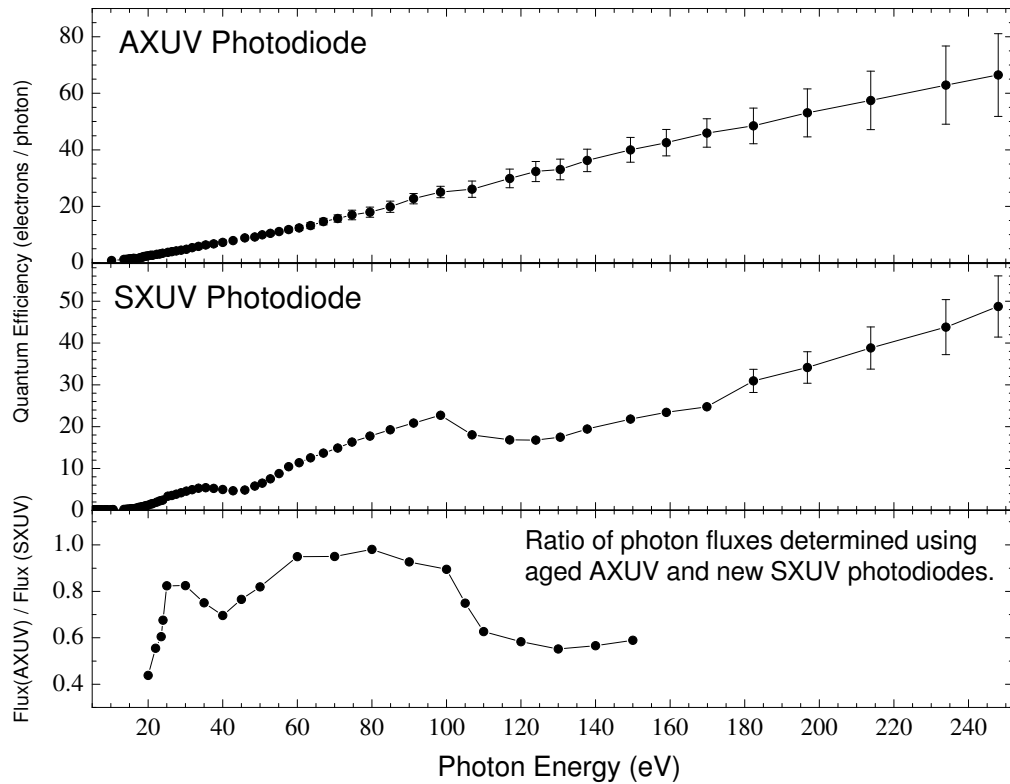


Figure 3.9: NIST-calibrated quantum efficiencies and measured photon flux ratios of the AXUV and SXUV photodiodes used for the photoionization measurements with cerium ions.

intense photon flux, especially at low photon energies, the AXUV-type photodiode was replaced by a radiation-hardened SXUV-type photodiode that served for all subsequent measurements. Figure 3.9 presents the NIST-calibrated quantum efficiencies of each photodiode and the ratio of the measured apparent photon fluxes with each after prolonged photon exposure of the AXUV-type photodiode. The photon flux measurements that had been made prior to August, 2007 using the AXUV-type photodiode were subsequently corrected using the ratio curve in the bottom panel of Figure 3.9.

3.3.4 Uncertainty Analysis

The merged-beams technique is one of the most accurate methods to measure photoionization cross sections of positively-charged ions and molecules. As in every experimental measurement, many sources of uncertainty arise. Merging ion and photon beams and measuring the outcome of their interaction leads to the following considerations:

- Uncertainty in collecting and detecting the parent ions.
- Uncertainty in the absolute sensitivity of the photon detector and photocurrent measurements.
- Uncertainty in the spatial overlap of the two beams, which is measured at only three discrete points along the interaction path and does not give complete information about their interaction.
- Uncertainty in the collection and detection efficiencies of the product ions.
- Statistical uncertainty in the product ion signal count-rate measurements.

Table 3.4 presents the measurement uncertainties for spectroscopy and absolute modes of the IPB endstation at the ALS [78]. In each case, the total uncertainties are given by the quadrature sum of individual sources, estimated at the 90% confidence level. It is important to note that for the endohedral metallofullerene $\text{Ce}@C_{82}^+$ photoionization, the total uncertainty is estimated between $\pm 30\%$ and $\pm 50\%$. Such a large uncertainty is due to an estimated and possibly varying C_{94}^+ ($m/q = 1128$) component of the primary $\text{Ce}@C_{82}^+$ ($m/q = 1124$) ion beam.

Table 3.4: Typical uncertainties in spectroscopy and absolute modes for photoionization cross-section measurements estimated at the 90% confidence level.

Source	Spectroscopy	Absolute	Total
Counting statistics	2%	5%	5%
Photoion collection efficiency, Ω	–	10%	10%
Photoion detection efficiency, Δ	–	3%	3%
Parent ion collection efficiency	–	2%	2%
Ion current measurement, I^+	2%	2%	3%
Photodiode responsivity, ϵ	5%	15%	16%
Photodiode current measurement, I^γ	2%	2%	3%
Beam profile measurement	–	10%	10%
Beam overlap integral, F_L	–	5%	5%
Interaction length, L	–	2%	2%
Quadrature sum	6%	22%	23%

Chapter 4

Ce⁺ Photoionization Measurements

4.1 Introduction

Absolute cross sections for single, double, triple and quadruple photoionization of Ce⁺ are presented in this chapter. Measurements were made in the energy range from 105 eV to 160 eV at a constant photon energy resolution of 100 meV. Ce⁺ is a Lanthanum-like ion which has the ground state electronic configuration $4d^{10}5s^25p^64f5d^2$ and the ground state term $^4H^o_{7/2}$ (ionization potential of 10.849 eV [27]). Significant oscillator strength is observed in the double and triple photoionization channels accounting for 39% and 47% of the total photoionization oscillator strength respectively.

4.2 Single Photoionization of Ce⁺

The Ce²⁺ photoion yield from photoionization of Ce⁺ was recorded as the photon energy was scanned from 105 eV to 160 eV. Individual scans were performed at a nominal photon energy resolution of 0.1 eV and joined together to create a photoionization spectrum, which was normalized to five absolute cross-section measurements by taking the average

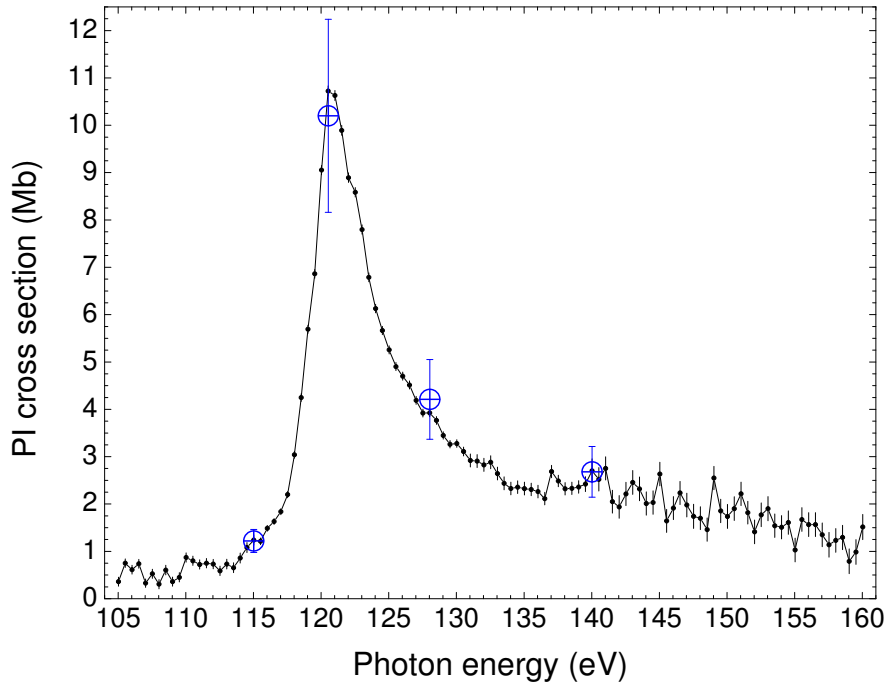


Figure 4.1: Single photoionization cross-section measurement for Ce^+ at 0.1 eV photon energy resolution. The large circles with error bars are absolute measurements.

of the ratios of the absolute measurements to the normalized signal counts at the corresponding energies and at the same resolution. The results are shown in Figure 4.1. No significant resonant structure is observed in the cross section. Rather, one broad asymmetric resonance dominates the cross section in the energy range where 4d excitations are expected and extends to the 4d continuum. This feature is attributed to $4d \rightarrow \epsilon f$ transitions.

Structure attributed to $4d \rightarrow np$ ($n \geq 6$) autoionization transitions is evident in the cross section above 135 eV with a small contribution to the total oscillator strength. So-called 'satellite' transitions are probably present above the 4d ionization threshold corresponding to 4d ionization with excitation of one 4f or 5d electron or two 5d electrons

[9] (see also page 2849 of ref. [36]). However, their contribution to the total oscillator strength is very small.

4.3 Double Photoionization of Ce^+

Figure 4.2 shows the absolute double photoionization cross section for Ce^+ in the energy range 105 - 160 eV at 0.1 eV energy resolution. Double photoionization is attributed mostly to the $4d \rightarrow \epsilon f$ ionization followed by single autoionization competing with multiple autoionization channels. A possible scheme for this process is:

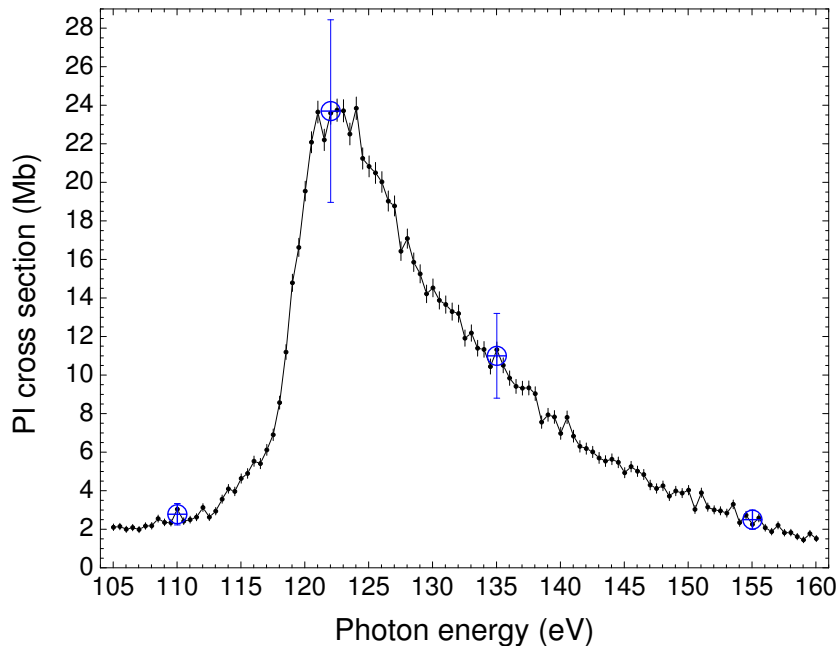
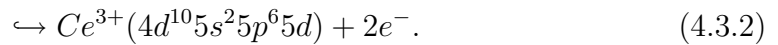
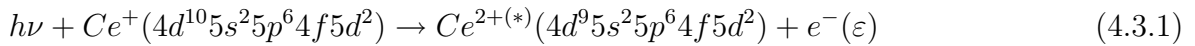
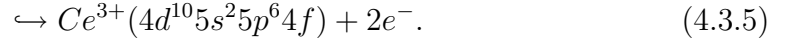
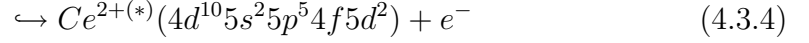
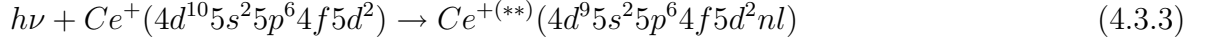


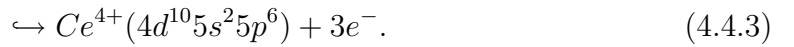
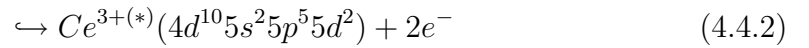
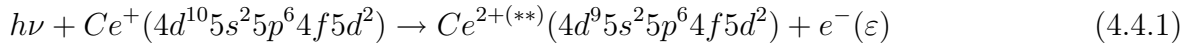
Figure 4.2: Double photoionization cross section of Ce^+ at 0.1 eV photon energy resolution. The large circles with error bars are absolute measurements .

The weak resonant transitions present in the cross section below the 4d ionization threshold could be due to $4d \rightarrow nl$ ($n \geq 6$ and $l = 1$ or $n \geq 4$ and $l = 3$) excitations decaying by sequential ejection of two Auger electrons:

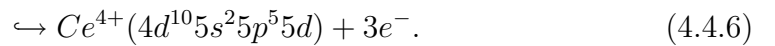
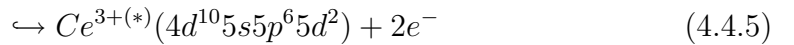
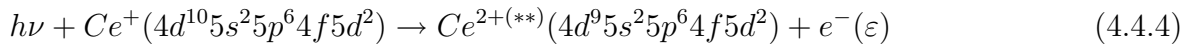


4.4 Triple Photoionization of Ce^+

Figure 4.3 shows the absolute triple photoionization cross section for Ce^+ in the energy range from 105 eV to 160 eV at 0.1 eV energy resolution. The strongest transitions are due to direct photoionization followed by the ejection of two sequential Auger electrons. Two autoionization paths are suggested for this process:



or



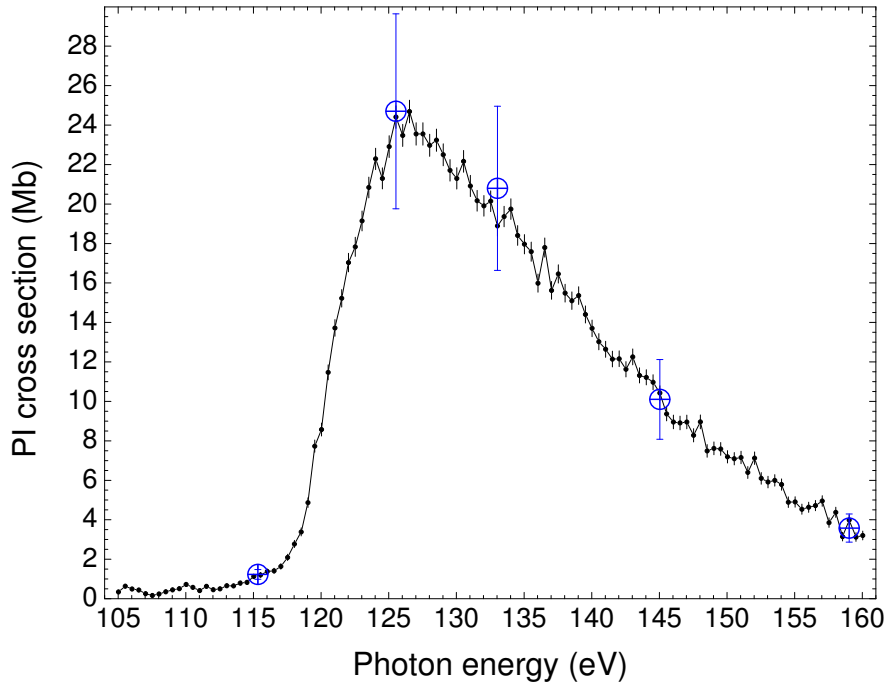
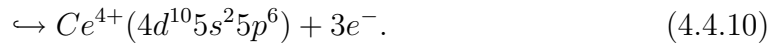
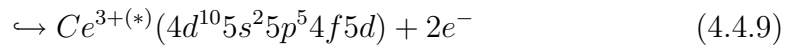
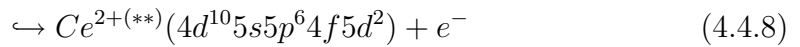
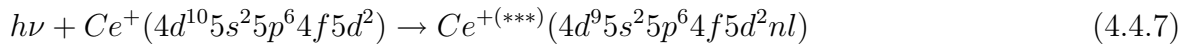


Figure 4.3: Triple photoionization cross section of Ce^+ at 0.1 eV photon energy resolution. The large circles with error bars are absolute measurements.

The weak resonant structure in the cross section likely arises from excitation of a 4d electron to a higher energy state followed by ejection of three Auger electrons:



4.5 Quadruple Photoionization of Ce^+

Figure 4.4 shows the relative yield of four times photoionized Ce^+ in the energy range 130 - 160 eV at an energy resolution of 0.1 eV. Although quadruple photoionization

measurements were made under similar conditions as the other photoionization channels, absolute measurements were not possible in this case because the 4:1 charge state ratio prevented simultaneous collection of the Ce^{4+} photoion signal and the Ce^+ primary ion beam. Thus the cross section scale for the results presented here should be considered approximate. Nevertheless, one may conclude that the contribution of this channel to the total photoionization cross section is very weak.

The transitions observed in the spectrum are attributed to direct photoionization of

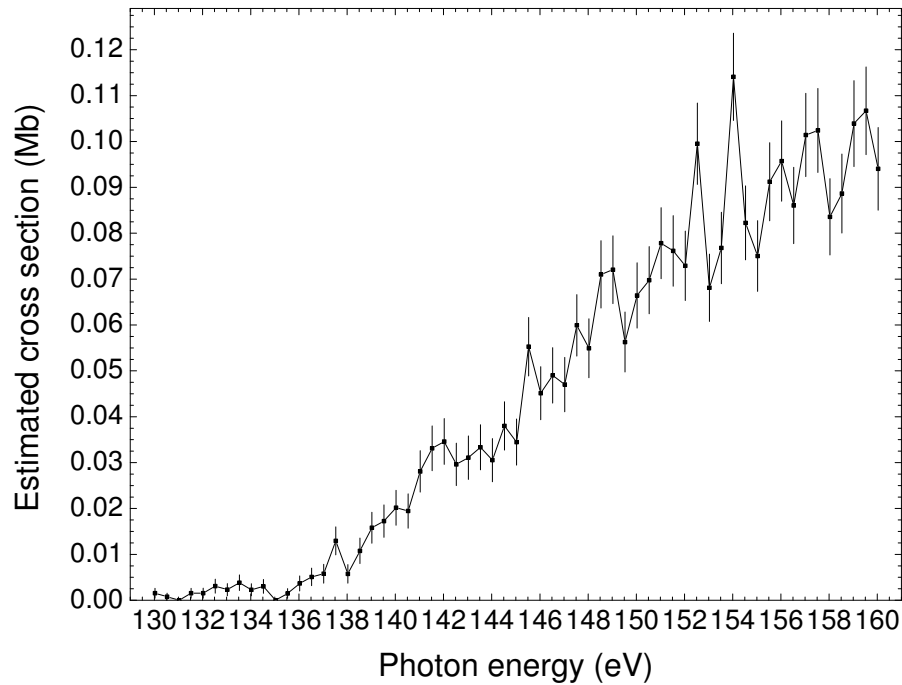
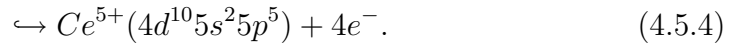
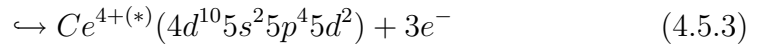
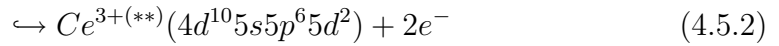
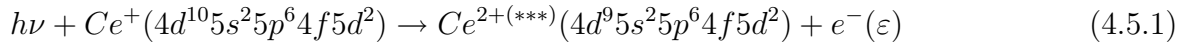


Figure 4.4: Quadruple photoionization cross section of Ce^+ at 0.1 eV photon energy resolution.

Table 4.1: Oscillator strengths (f) of the different photoionization channels of the La-like Ce^+ .

Final Charge State	Energy Range (eV)	f	Partial Contribution (%)
2	105-160	1.55	14.2
3	105-160	4.18	38.6
4	105-160	5.10	47.2
Total	105-160	10.8	100

the 4d electron followed by three autoionizations :



The contributions of single, double, and triple ionization channels to the total photoionization cross section of Ce^{2+} are compared in Figure 4.5. Also presented are the double-to-single and triple-to-single photoionization cross-section ratios (bottom panels). Integration of the cross section for each channel over the experimental energy range shows the dominance of triple photoionization, which constitutes nearly half of the total photoionization oscillator strength of Ce^+ in this energy range. Partial oscillator strengths for single and multiple photoionization of the Ce^+ ion are presented in Table 4.1.

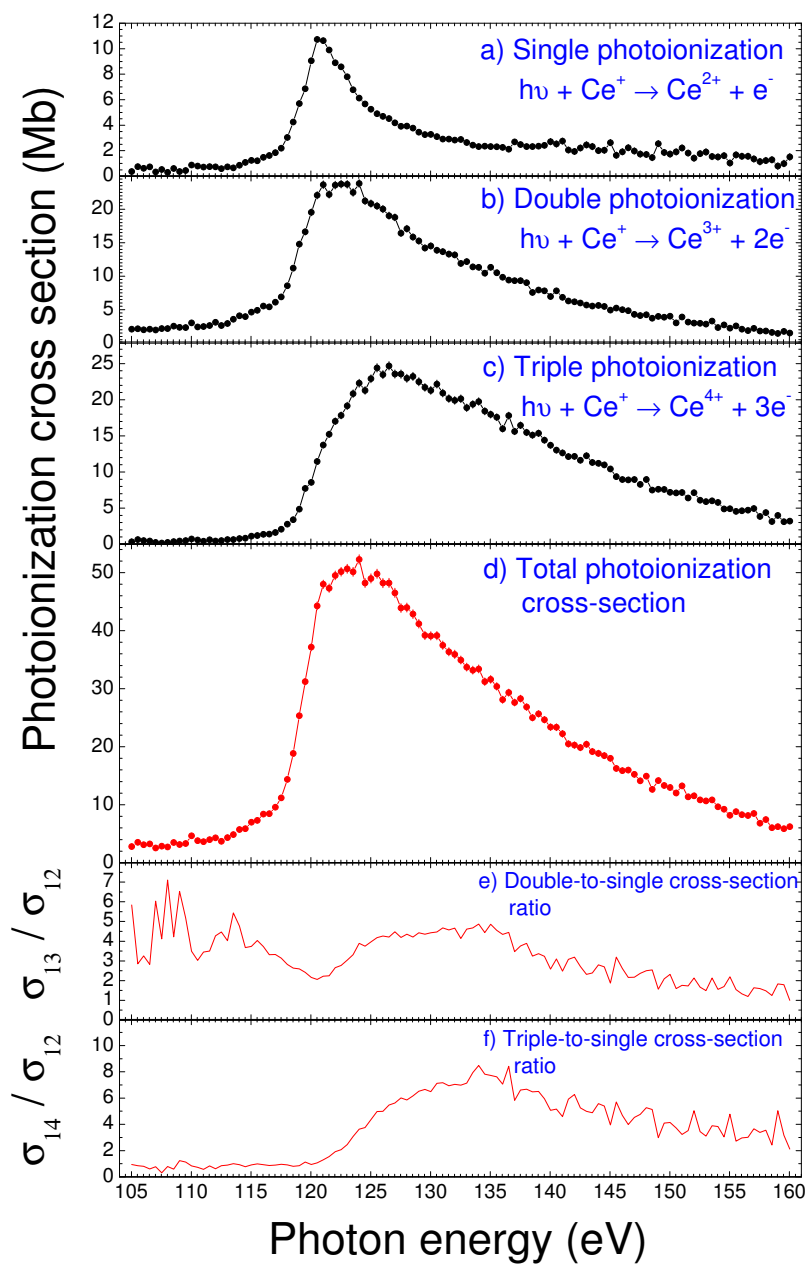


Figure 4.5: Total photoionization cross section of Ce^+ at 0.1 eV photon energy resolution (panel d)). Single, double, and triple photoionization graphs (panels a), b) and c), respectively) are shown for comparison of the contributions of each channel to the total cross section. e) and f) Double-to-single and triple-to-single cross-section ratios, respectively.

Chapter 5

Ce²⁺ Photoionization Measurements

5.1 Introduction

Single, double and triple absolute photoionization cross sections for Ce²⁺ ion are presented in this chapter. Experiments were performed in the 4d giant resonance energy region. The spectroscopic scans were normalized to absolute cross-section measurements performed at the same energy resolution. The Barium-like Ce²⁺ has the ground-state electronic configuration [Kr]4d¹⁰5s²5p⁶4f² and the ground-state term ³H₄, with two metastable states ³H₅ and ³H₆ lying above the ground state by 0.189 eV and 0.388 eV, respectively [27]. Minimum oven and microwave powers were used during the experiments to produce Ce²⁺ ions in the ECR ion source in order to minimize the metastable population in the primary ion beam. However, a mixture of initial states in the primary beam is to be expected. Table 5.1 shows the NIST tabulated energy levels for Ce²⁺ ion for the even-parity [Kr]4d¹⁰5s²5p⁶4f² and odd-parity [Kr]4d¹⁰5s²5p⁶4f¹5d¹ configurations.

Table 5.1: Ground state and metastable states of Ba-like Ce^{2+} as tabulated in the NIST database [27].

Configuration	Term	J	Level (eV)
[Xe]4f ²	³ H	4	0.000
		5	0.189
		6	0.388
[Xe]4f5d	¹ G ^o	4	0.406
[Xe]4f ²	³ F	2	0.467
		3	0.591
		4	0.621
[Xe]4f5d	¹ D ^o	2	0.815
[Xe]4f5d	³ P ^o	0	1.435
		1	1.44
		2	1.567

5.2 Ce^{2+} Single Photoionization

The Ce^{3+} photoionization signal was measured as the energy was scanned from 105 eV to 174 eV at a resolution of 0.1 eV and then normalized to four absolute cross-section measurements at discrete energies with the same energy resolution. Figure 5.1 shows the dominance of direct photoionization above 127.5 eV, constituting 38% of the total oscillator strength of 4.04 in the single-photoionization channel. The resonant photoionization cross section due to autoionizing excitations of the 4d inner shell to 4f and np ($n \geq 6$) outer shells are evident in the spectrum below 127.5 eV. Identification of 4d \rightarrow np Rydberg series was not possible due to the small oscillator strengths of these transitions compared to those of 4d \rightarrow 4f transitions. In addition, the photon energy resolution and step size of 0.1 eV used in this experiment were not enough to separate all the resonances.

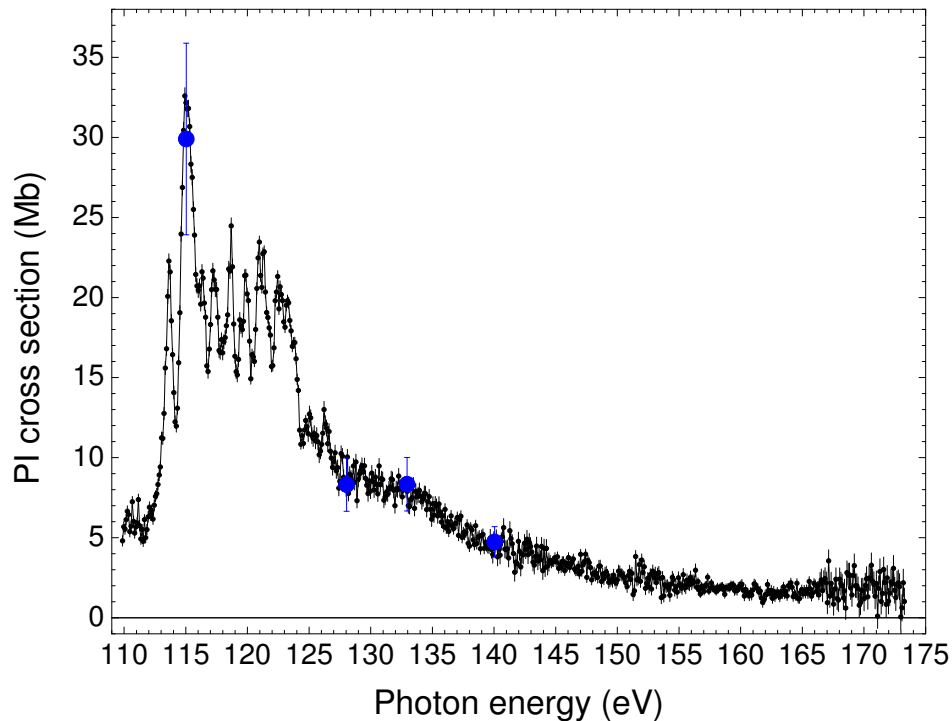


Figure 5.1: Single photoionization cross section of Ce^{2+} at 0.1 eV photon energy resolution. The dots with large error bars are absolute measurements.

5.3 Ce^{2+} Double Photoionization

Double photoionization cross-section measurements for Ce^{2+} were performed in the energy range 105 - 170 eV at 0.1 eV resolution and are presented in Figure 5.2. A broad asymmetric shape resonance dominates the cross section where 4d excitations are expected and extends to the 4d continuum, similar to that observed in photoionization of Ce^+ . This is attributed to $4d \rightarrow \epsilon f$ direct photoionization accompanied by double autoionization. Resonant photoionization attributed to $4d \rightarrow 4f$ excitations followed by double autoionization are evident in the cross section below 127 eV. Features due to $4d \rightarrow np$ autoionizing excitations may also be present in the double photoionization

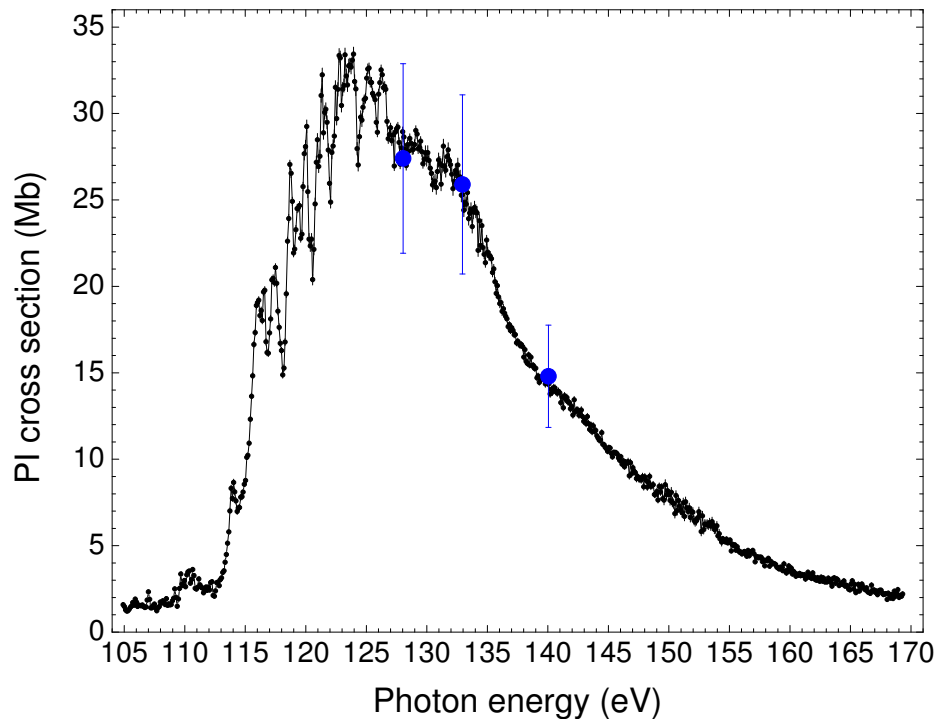


Figure 5.2: Double photoionization cross section of Ce^{2+} at 0.1 eV Photon energy resolution. The dots with large error bars are absolute measurements.

cross section. However, calculations indicated their contribution to the total oscillator strength to be relatively small.

5.4 Ce^{2+} Triple Photoionization

Figure 5.3 presents measurements of the cross section for triple photoionization of Ce^{2+} in the energy range from 120 eV to 160 eV at 0.1 eV resolution. The onset in the cross section gives a triple-ionization threshold of 123.5 ± 1.3 eV, which compares to the NIST value of 122.5 eV [27]. Possible weak resonant features likely result from excitation of the 4d electrons to higher energy states followed by emission of three Auger electrons. A

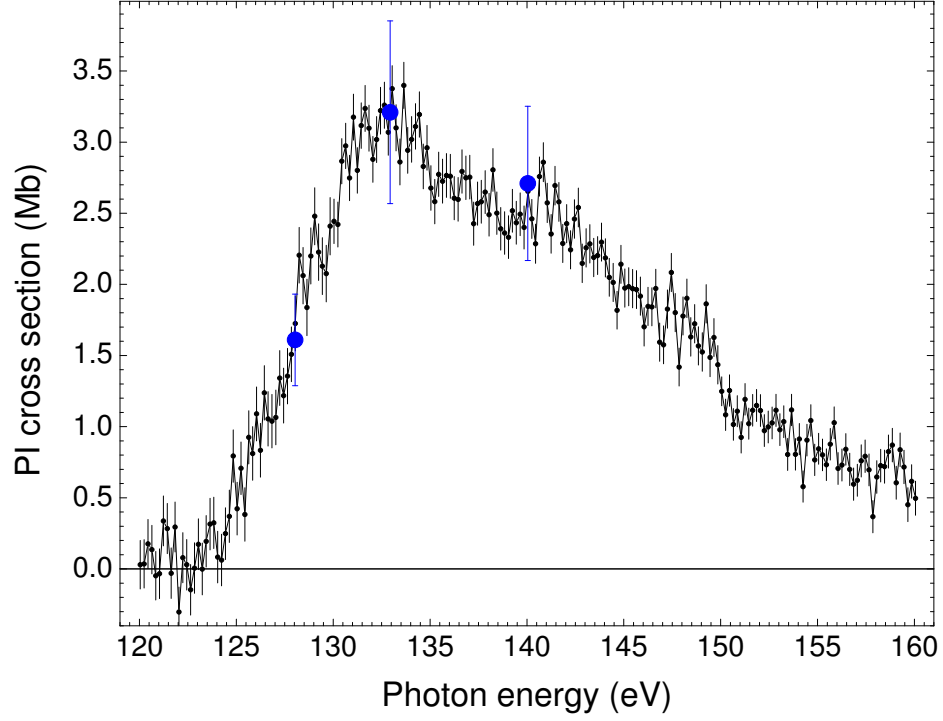
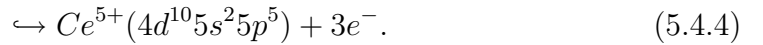
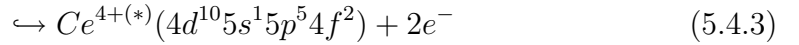
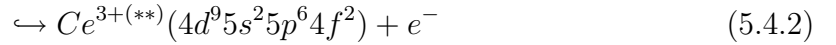
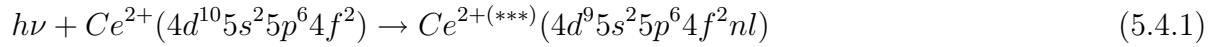


Figure 5.3: triple photoionization cross-section of Ce^{2+} at 0.1 eV photon energy resolution. The circles with large error bars are absolute measurements.

possible pathway for this process is:



This scheme describes decay of the initial 4d core vacancy state by sequential Auger processes, for which there are other possibilities.

The contributions of single, double, and triple ionization channels to the total photoionization cross section of Ce^{2+} are compared in Figure 5.4. Also presented are the

Table 5.2: Oscillator strengths (f) for single, double, and triple photoionization of Ba-like Ce^{2+} .

Final Charge State	Energy Range (eV)	f	Partial Contribution (%)
3	110-173	4.04	33.4
4	105-169	7.47	61.7
5	120-160	0.59	4.9
Total		12.10	100.0

double-to-single and triple-to-single photoionization cross-section ratios (bottom panels). Integration of the cross section for each channel over the experimental energy range shows the dominance of double photoionization, which constitutes more than half of the total photoionization oscillator strength of Ce^{2+} in this energy range. Partial oscillator strengths for single and multiple photoionization of the Ce^{2+} ion are presented in Table 5.2. Since Auger decay of the 4d vacancy states dominates compared to radiative decay, the total oscillator strength in Table 5.2 corresponds to the total photoabsorption oscillator strength. A value greater than 10 (the number of 4d electrons) is not surprising, since direct photoionization of 5s, 5p and 4f electrons is also possible in this energy range.

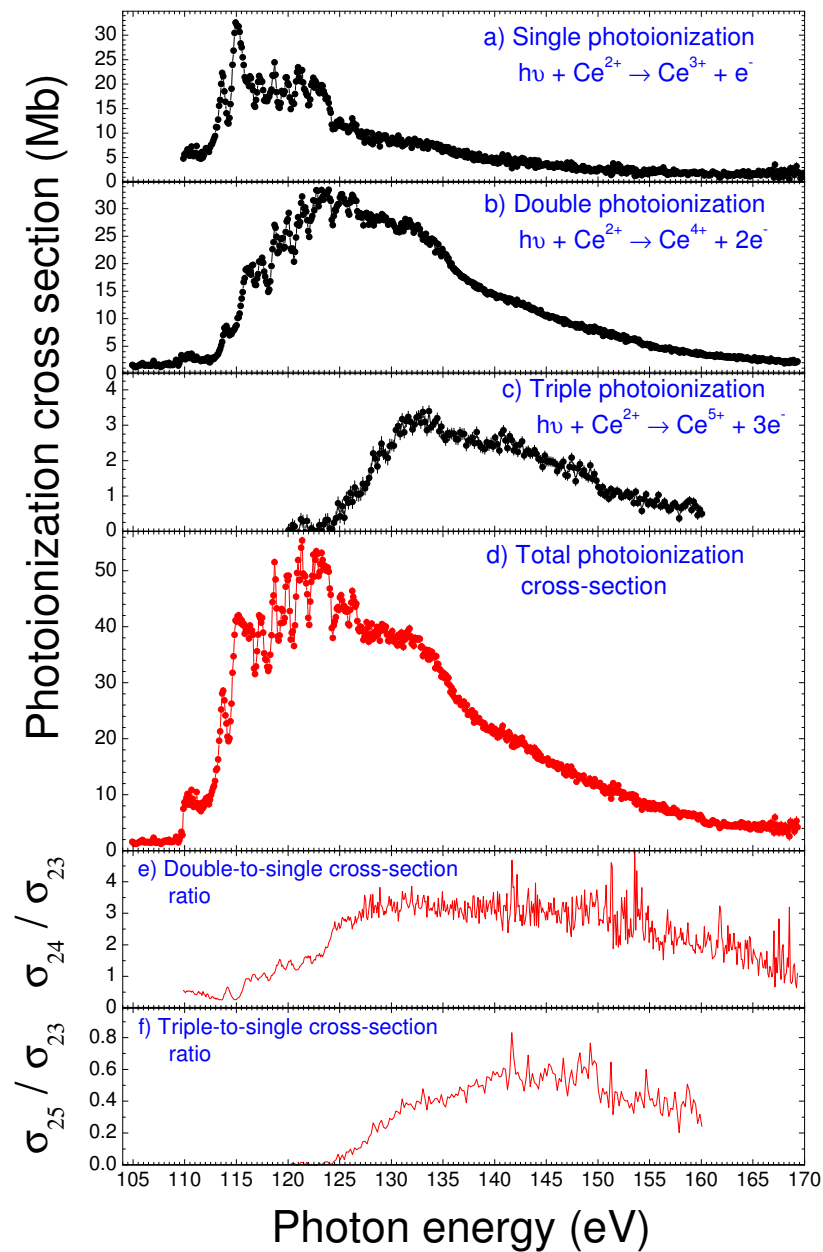


Figure 5.4: Total photoionization cross section of Ce^{2+} at 0.1 eV Photon energy resolution (panel d). Single, double, and triple photoionization cross sections (panels a, b, and c) are shown for comparison of the contribution of each channel to the total cross section. Panels e and f present ratios of double-to-single and triple-to-single photoionization cross sections of Ce^{2+} , respectively.

Chapter 6

Ce³⁺ Photoionization Measurements

6.1 Introduction

Absolute single and double photoionization cross-section measurements were performed for the Ce³⁺ ion in the energy range of the 4d giant resonance. The Cs-like Ce³⁺ has the ground-state electronic configuration 4d¹⁰5s²5p⁶4f¹ with the ground-state term ²F_{5/2}^o and the metastable term ²F_{7/2}^o, for which the fine-structure splitting is 0.279 eV [27]. Four Rydberg series have been assigned, with the aid of the online Cowan code [28] and the quantum defect theory [42], for single and double photoionization of this ion including 4d → nf and 4d → np autoionizing excitations. The NIST tabulated single and double ionization thresholds for Ce³⁺ ion are 36.757 eV and 102.307 eV, respectively [27].

6.2 Single Photoionization of Ce³⁺

Ce⁴⁺ product ions were counted as the photon energy was scanned from 105 eV to 150 eV at a resolution of 0.1 eV and then normalized to absolute cross-section measurements at four discrete energies. The single photoionization cross-section for Ce³⁺, presented in Figure 6.1, is dominated by 4d → nf and 4d → np autoionizing excitations. Two

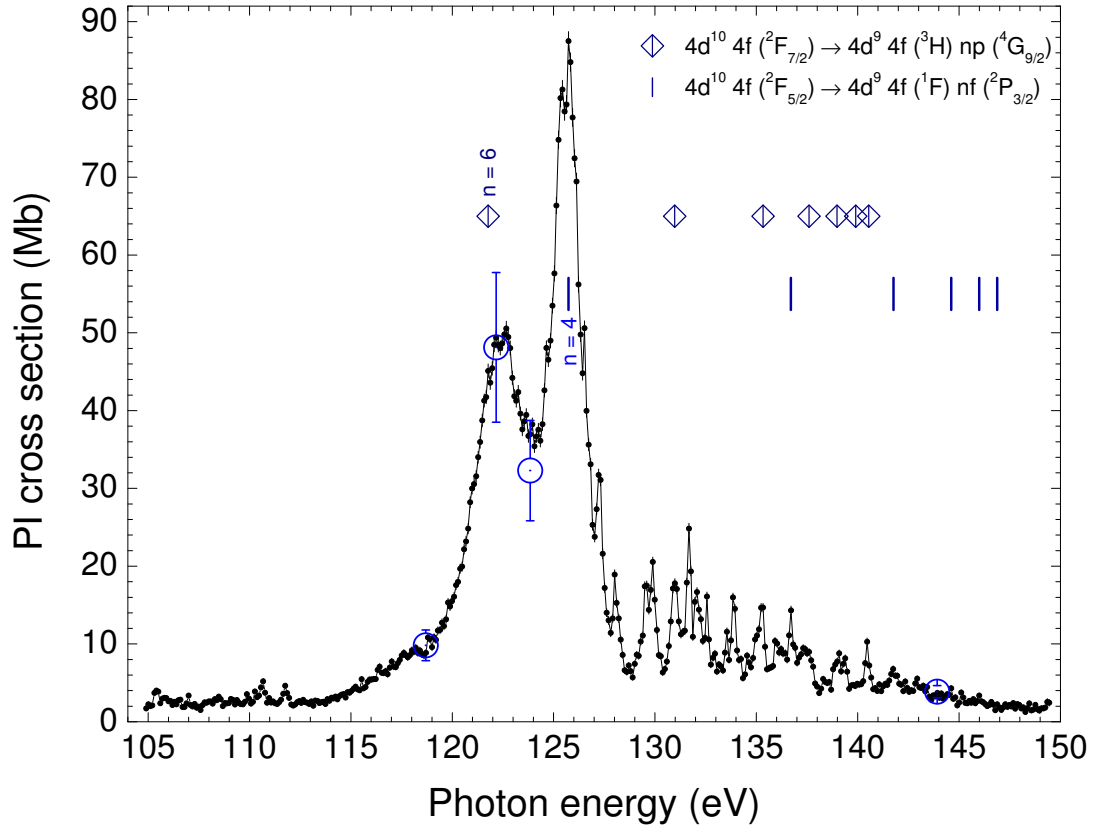


Figure 6.1: Single photoionization cross section of Ce^{3+} at 0.1 eV energy resolution. Two Rydberg series of autoionizing excitations of 4d inner-shell electrons to nf and np orbitals were identified.

Rydberg series resulting from transitions of 4d electrons to excited nf and np orbitals were assigned. Figure 6.2 presents two fits of the experimental resonance energies as functions of the principal quantum number by use of Rydberg formula. The first Rydberg series is a result of autoionizing excitations of Ce^{3+} in the ground state to $4d^9 5s^2 5p^6 4f^1 ({}^1F) nf^1 {}^2P_{3/2}$ ($n \geq 4$) states converging to the $4d^9 5s^2 5p^6 4f^1 {}^1F$ limit of Ce^{4+} . The calculated energy limit (E_{limit}) for this series is 150.21 eV using the Cowan code [28], compared to the fit value of 150.48 eV using the quantum defect theory. The second Rydberg

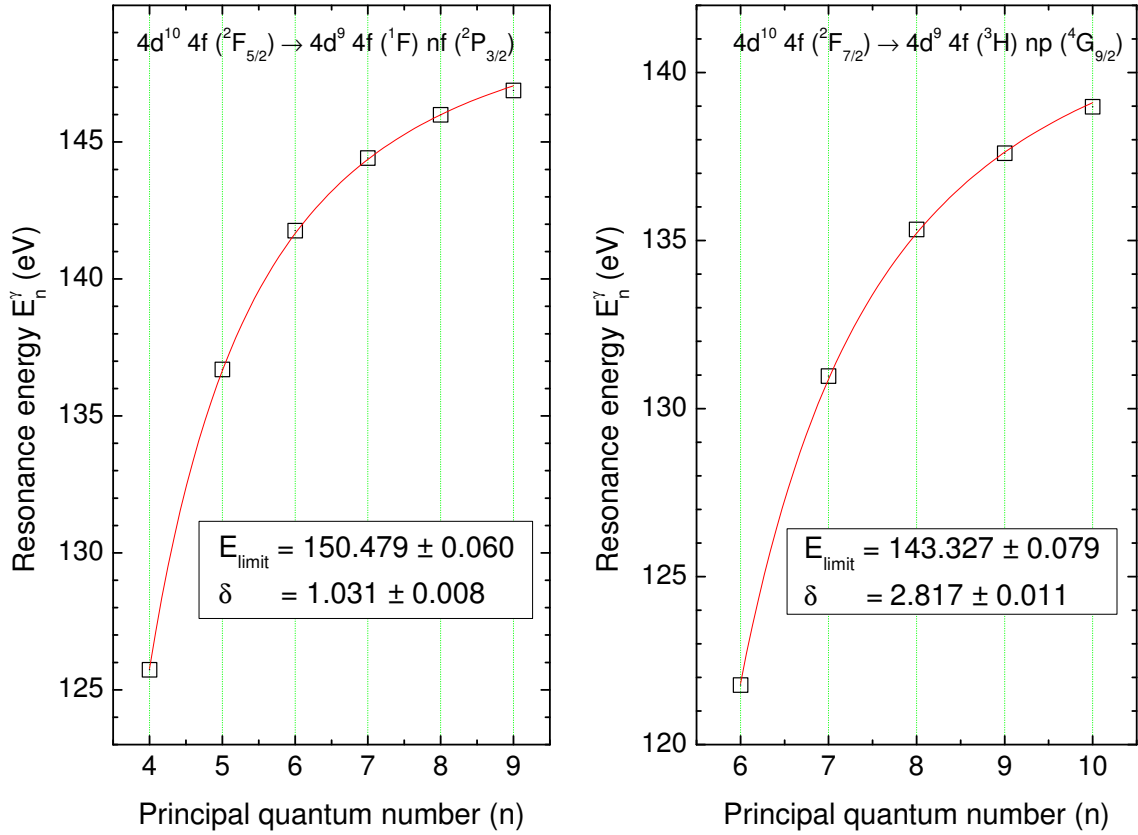


Figure 6.2: Rydberg fits for the $4d^{10}4f^1nf^1 2P_{3/2}$ and $4d^{10}4f^1np^1 4G_{9/2}$ series originating from the $2F_{5/2}$ ground state and the $2F_{7/2}$ metastable state, respectively, in the single photoionization cross section of Ce^{3+} . The series limit E_{limit} and quantum defect parameter δ are given for each series.

series originates from excitations of 4d electrons of Ce^{3+} in the $2F_{7/2}^o$ metastable state to $4d^9 5s^2 5p^6 4f^1 (3H) np^1 4G_{9/2}$ ($n \geq 6$) states converging to the $4d^9 5s^2 5p^6 4f^1 3H$ limit of Ce^{4+} . The energy limit 143.327 eV of this series is in good agreement with the Cowan code calculated energy of 143.336 eV [28].

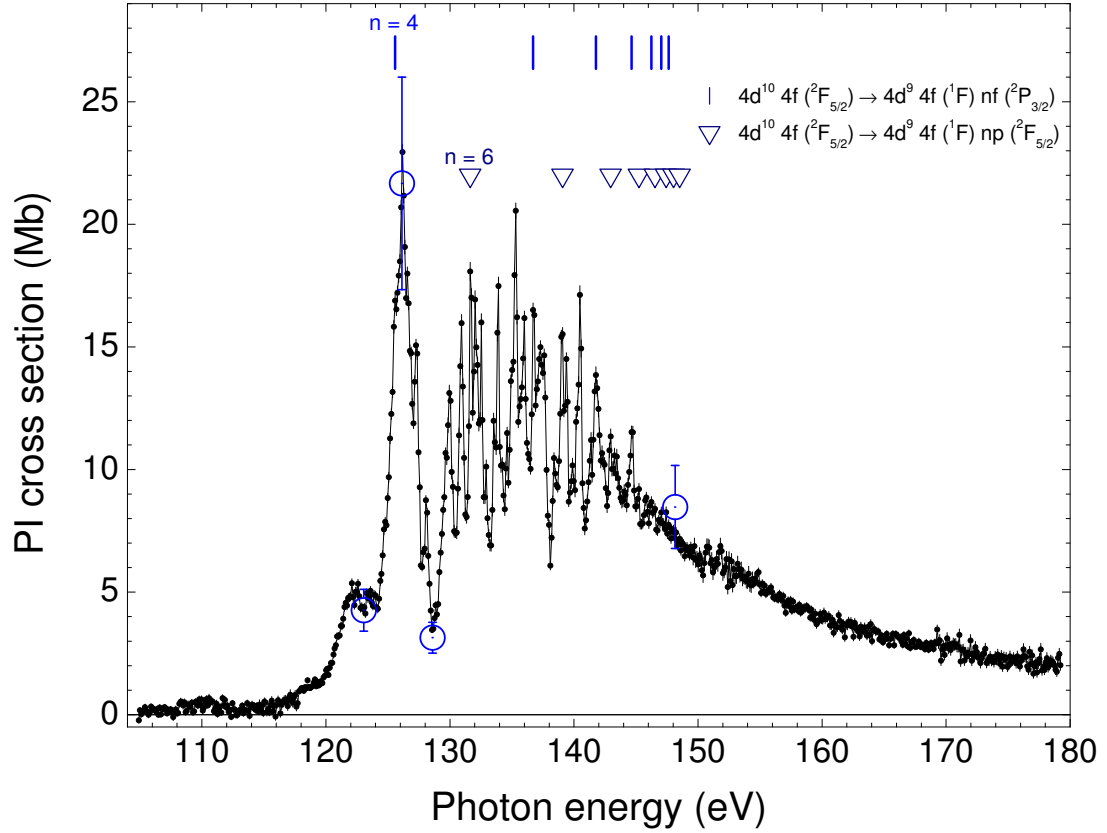
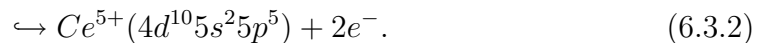
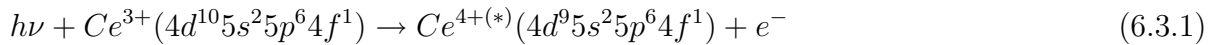


Figure 6.3: Double photoionization cross section of Ce^{3+} at 0.1 eV energy resolution. Two Rydberg series of autoionizing excitations of 4d inner-shell electrons to nf and np orbitals of Ce^{3+} were identified.

6.3 Double Photoionization of Ce^{3+}

Figure 6.3 shows the double photoionization cross-section measurements for Ce^{3+} from 105 eV to 180 eV photon energy at 0.1 eV resolution. Direct photoionization accompanied by autoionization dominates the cross section above 150 eV. This can be represented by the following process:



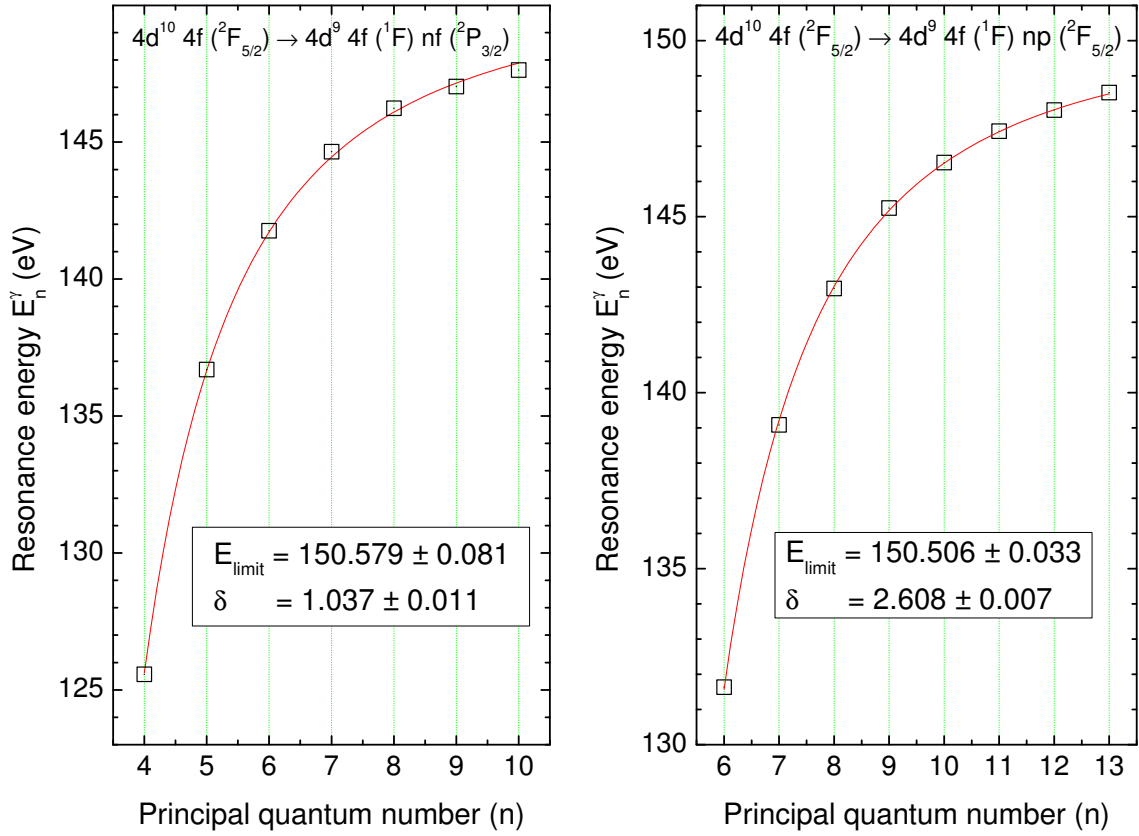


Figure 6.4: Rydberg fits for the $4d^{10}4f^1nf^1 \ ^2P_{3/2}$ and $4d^{10}4f^1np^1 \ ^2F_{5/2}$ series originating from the $^2F_{5/2}$ ground state, in the double photoionization cross section of Ce^{3+} .

Resonant photoionization cross section features observed below 150 eV originate from excitations of 4d electrons to higher energy orbitals nf and np followed subsequently by emission of two Auger electrons. Two Rydberg series were assigned in the double photoionization cross section of Ce^{3+} , both originating from the ground state. The first series results from excitation from the ground state to the $4d^9 5s^2 5p^6 4f^1(1F)nf^1 \ ^2P_{3/2}$ final state, which is identical to the first series observed in the single photoionization cross section. An increase of the double-to-single photoionization cross-section ratio for the higher

Table 6.1: Oscillator strengths (f) of the two photoionization channels of the Cs-like Ce^{3+} .

Final Charge State	Energy Range (eV)	f	Partial Contribution (%)
2	105-150	5.03	58
3	105-180	3.64	42
Total		8.67	100

members of this series at increasing photon energy indicates the competition between different autoionizing channels (see bottom panel of Figure 6.5). The second Rydberg series arises from excitations of Ce^{3+} in the ground state to $4d^9 5s^2 5p^6 4f^1(^1F)np^1\ ^2F_{5/2}$ final states. No identifications were made of Rydberg series due to double photoionization from the metastable state.

The contributions of single and double photoionization channels to the total photoionization cross section of Ce^{3+} are presented in Figure 6.5 and oscillator strengths associated with these channels are presented in Table 6.1.

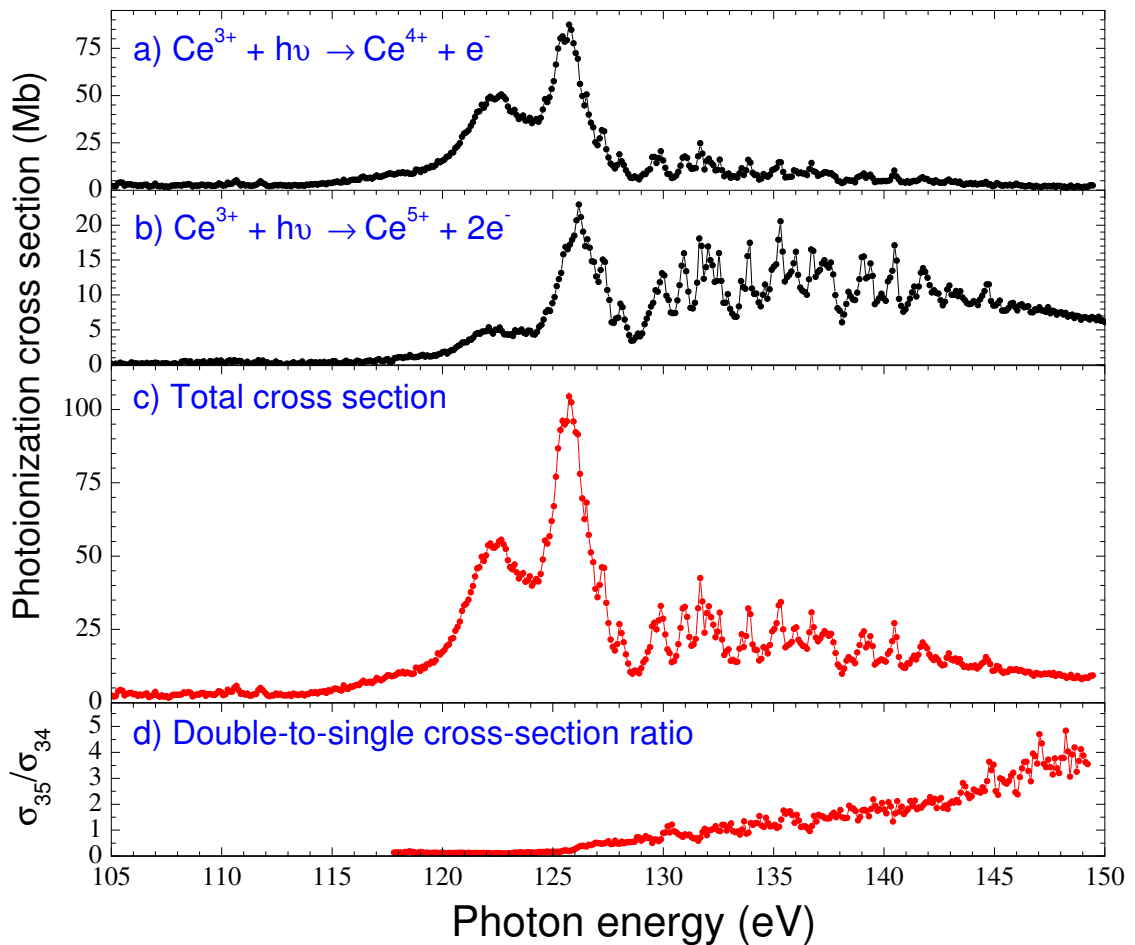


Figure 6.5: Total photoionization cross section for Ce^{3+} at 0.1 eV energy resolution (panel c). Single and double photoionization cross sections (panels a and b) are shown to compare their partial contributions to the total cross section. Panel d presents the double-to-single photoionization cross-section ratio of Ce^{3+} .

Chapter 7

Ce⁴⁺ Photoionization Measurements

7.1 Introduction

The closed-shell Xe-like Ce⁴⁺ has the ground-state electronic configuration [Kr]4d¹⁰5s²5p⁶ and the ground-state term ¹S₀. Long-lived metastable states with the electronic configuration [Kr]4d¹⁰5s²5p⁵4f are found very important to interpret the experimental data, as noted by Kjeldsen (see the discussion on pages R356 and R357 of reference [25]). Ions in the metastable states were estimated to account for 25% of the parent ion beam. Multi-configuration Hartree-Fock calculations were performed using the Cowan code [19, 20] to identify structure in the experimental data.

7.2 Single Photoionization of Ce⁴⁺

The Ce⁵⁺ photoion signal was measured as the photon energy was scanned from 110 eV to 150 eV at a constant resolution of 0.1 eV. The photoion yield was normalized to the absolute cross-section measurements which were performed at the same energy resolution. Figure 7.1 shows the single photoionization cross section of Ce⁴⁺ in the 4d inner-shell excitation region. The structure below 129.6 eV is mostly due to 4d¹⁰5s²5p⁵4f

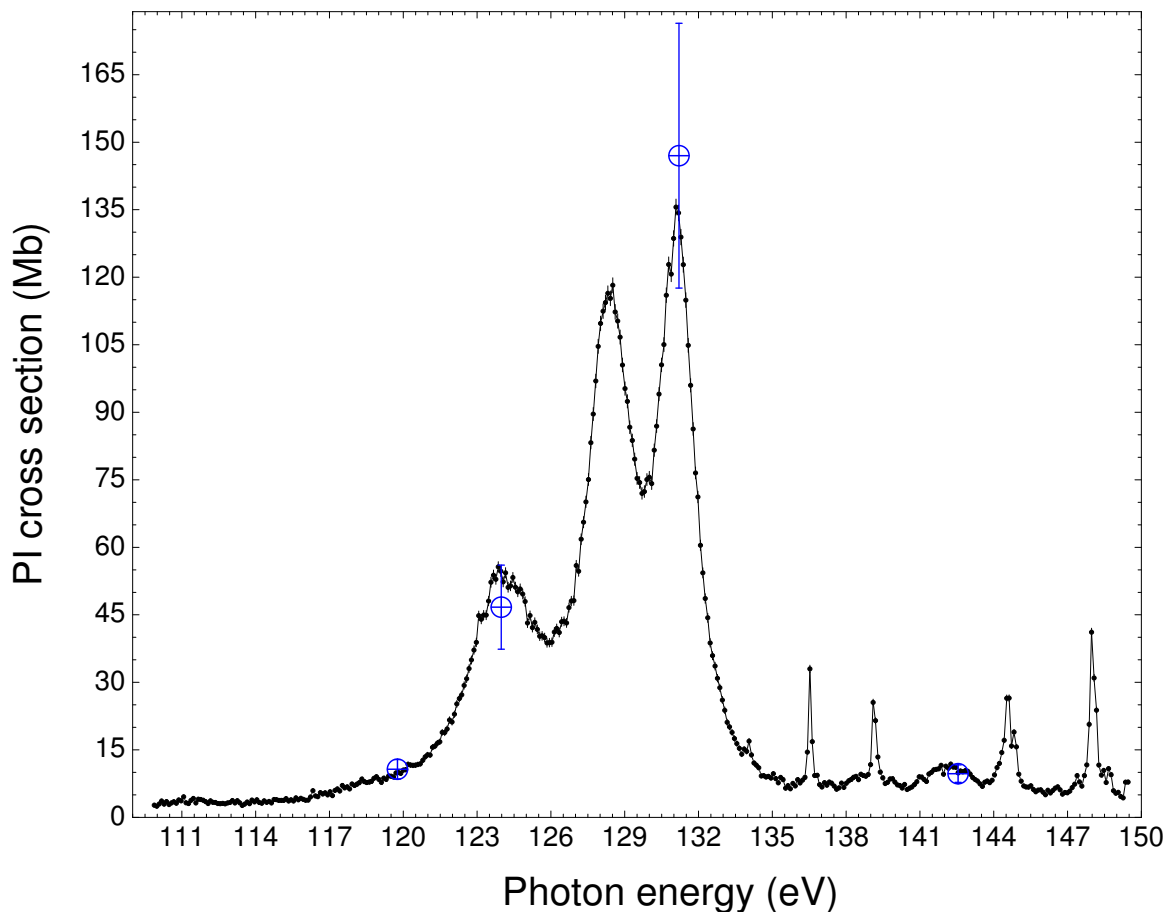


Figure 7.1: Single photoionization cross-section measurements for Ce^{4+} at 0.1 eV energy resolution. The large circles with error bars are absolute measurements to which the spectrum has been normalized.

→ $4d^9 5s^2 5p^5 4f^2$ transitions followed by ejection of an Auger electron. However, the peaks are very broad, especially below 126 eV (see Figure 7.2 (top)). Direct photoionization of the $5s^2$ sub-shell is also possible in this energy region, although its contribution to the total cross section is relatively small. The strongest resonance at 131.09 eV is assigned to $4d^{10} 5p^6 \ ^1S_o \rightarrow 4d^9 5p^6 (4f \ ^2F) \ ^3D_1$ excitation followed by autoionization. Resonances

near and including the strongest peak (129.7 - 135 eV) are attributed to the fine structure of the final states of the $4d^9 5p^6 4f$ configuration. The structures at 136.52 eV and

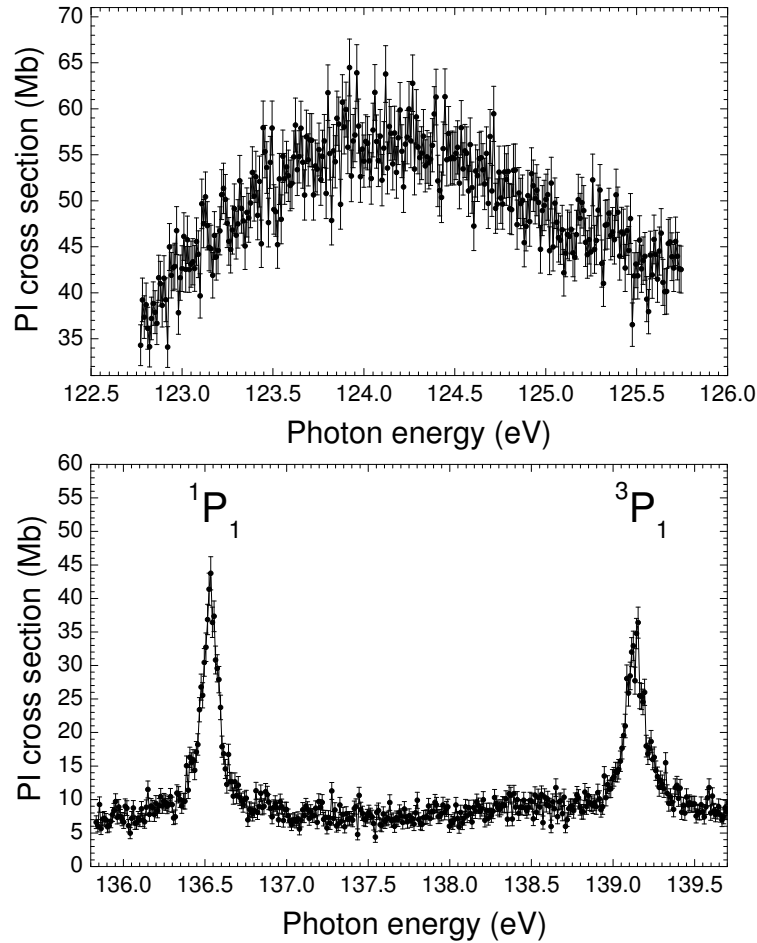


Figure 7.2: Top: $4d \rightarrow 4f$ transitions in the single photoionization of Ce^{4+} metastable states at 0.05 eV energy resolution. Bottom: $4d \rightarrow 6p$ transitions (1P_1 and 3P_1 final states) in the single photoionization of the Ce^{4+} ground-state at 0.05 eV energy resolution.

139.09 eV are assigned to excitation of 4d electrons from the ground state to 6p excited states. The first peak is attributed to the $4d^9 5p^6 (6p \ ^2P) ^1P_1$ final state and the second to $4d^9 5p^6 (6p \ ^2P) ^3P_j$ final states. The measured energy splitting between the 1P_1 and

3P_1 fine states is 2.57 eV, which compares to a calculated value of 2.65 eV. At this energy resolution, the first resonance appears more symmetric than the second due to the hyperfine structure splittings in the latter, which is evident in measurements performed at 0.05 eV resolution (see Figure 7.2 (bottom)). The structure near 144.6 eV and 148 eV arises from the transitions $4d^{10}5p^6\ ^1S_o \rightarrow 4d^95p^6(5f\ ^2F)^3D_j$ and $4d^{10}5p^6\ ^1S_o \rightarrow 4d^95p^6(5f\ ^2F)^1P_1$, respectively. The measured splitting of the fine structure states 3D_1 and 1P_1 is 3.5 eV compared to 3.4 eV in the calculations. Hyperfine structure is observed in the 3D_1 peak (see Figure 7.3). The measured energy splitting between the 3D_1 and 3D_3 states is 0.27 eV, compared to a calculated value of 0.42 eV. A small resonance near the 1P_1 peak at 148.7 eV is attributed to excitation of 4d electrons from the ground state to $4d^95p^6(7p\ ^2P)^1P_1$.

7.3 Double Photoionization of Ce^{4+}

The Ce^{6+} photoion yield was recorded as the photon energy was scanned in the range 130 - 180 eV at a constant resolution of 0.1 eV. The photoion yield was then normalized to absolute cross sections measured at the same resolution. Figure 7.4 shows the double photoionization cross section for Ce^{4+} in the 4d inner-shell excitation region. The structure in the cross section is mostly due to excitation of a 4d electron from the ground state to an nl excited state ($n \geq 6$ for $l = 1$ and $n \geq 5$ for $l = 3$) followed by ejection of two Auger electrons. However, double photoionization contributes much less than single photoionization to the total oscillator strength (see Table 7.1). The following pathway is

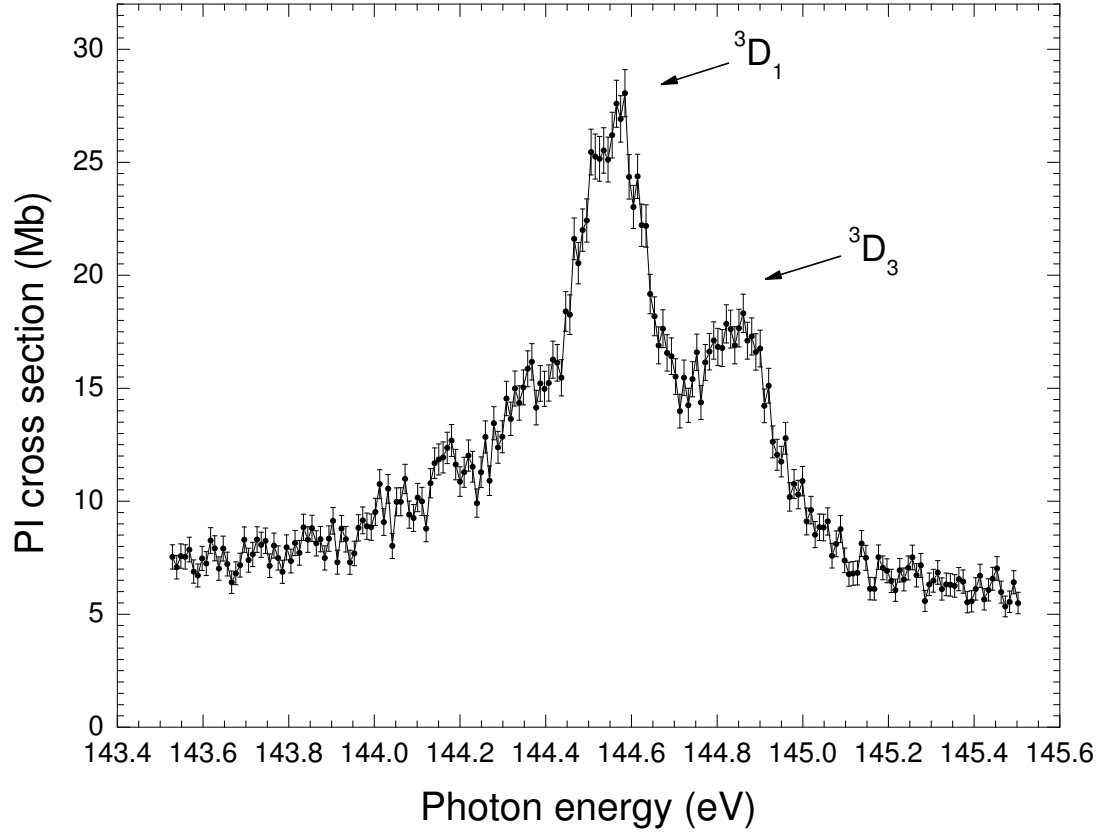
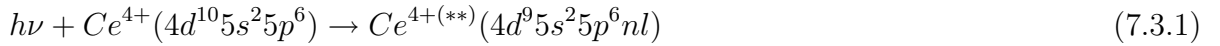


Figure 7.3: $4d \rightarrow 5f$ transitions (3D_1 and 3D_3 final states) in the single photoionization of Ce^{4+} ground state at 0.1 eV energy resolution and 0.01 eV energy steps.

suggested to illustrate this process:



7.4 Comparison with Hartree-Fock Calculations

Figure 7.5 shows a comparison between the calculated resonant photoionization cross sections of Ce^{4+} (bottom panel) from the $4d^{10}5s^25p^54f$ metastable states (top panel) and

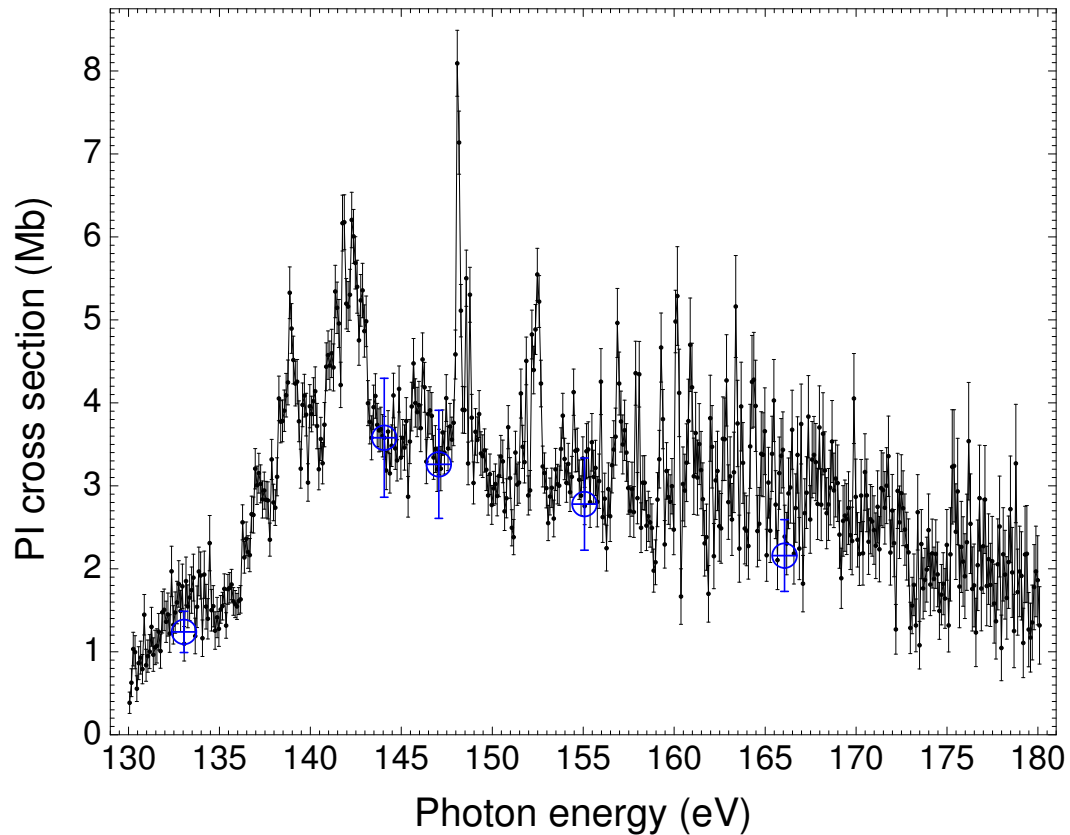


Figure 7.4: Double photoionization cross-section measurements for Ce^{4+} at 0.1 eV energy resolution. The large circles with error bars are absolute measurements.

$4d^{10}5s^25p^6\ ^1S_0$ ground-state (middle panel). The calculated cross sections were convoluted with a Gaussian profile of 0.1 eV full width at half maximum to simulate the experimental resolution. The calculated energies were shifted downward by 0.54 eV and 2.67 eV for calculated photoionization cross sections from the ground-state and the metastable states of Ce^{4+} ions, respectively. The calculations show a fair agreement with the experiment. However, several discrepancies are evident. The calculated oscillator strength is higher than the measured value (17.8 compared to 10.3). In addition, the transitions' lifetimes are overestimated in the calculations, which yield much narrower resonances and thus

Table 7.1: Oscillator strengths (f) of the two photoionization channels of the Xe-like Ce^{4+} .

Final charge state	Energy range (eV)	f	Partial contribution (%)
5	110-150	8.97	86.9
6	130-180	1.35	13.1
Total		10.32	100

higher cross sections than the experiment (9 times higher for the strongest peak). Hence, it was necessary to scale the calculated cross sections by 0.1 to compare them to the experiment on the same scale. Moreover, the calculated energy separation between the ground state and the lowest lying metastable state was lower than the experiment by more than 2 eV.

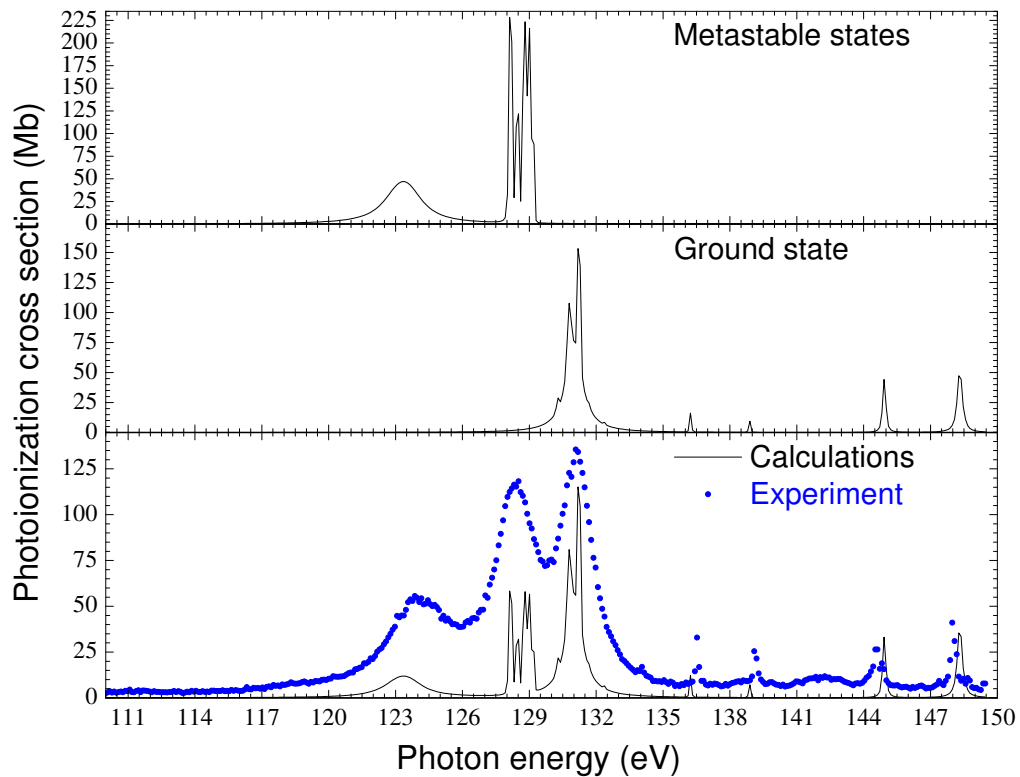


Figure 7.5: Calculated photoionization cross section of Ce^{4+} from the $4d^{10}5s^25p^54f$ metastable states (upper panel) and the ground state (middle panel). The calculated cross sections were convoluted with a Gaussian profile of 0.1 eV FWHM, and the energies for metastable states and the ground state were shifted downward by 2.67 eV and 0.54 eV, respectively. An admixture of 25% metastable states and 75% ground state were used to compare the calculations with the experiment (lower panel). The calculated cross sections are divided by 10 to be compared on the same scale with the experiment.

Chapter 8

Photoionization Measurements for Ce^{5+} , Ce^{6+} , and Ce^{7+}

8.1 Introduction

Absolute photoionization measurements for the three Cerium ions Ce^{5+} , Ce^{6+} , and Ce^{7+} in the 4d excitation region are presented in this chapter. All three ions have the common characteristic of an open 5p outer shell in the ground-state configuration. Their photoionization cross sections are similar to that observed for Ce^{4+} , except that the $4d \rightarrow 4f$ transitions are more dominant in the photoionization of Ce^{5+} , Ce^{6+} and Ce^{7+} . The $^{142}\text{Ce}^{q+}$ isotope ($q = 5, 7$) was used for absolute cross-section measurements because of possible contamination of the parent ion beam using the dominant mass 140 isotope with N_2^+ and CO^+ for Ce^{5+} , and with Ar^{2+} for Ce^{7+} . Their presence in the primary ion beams of isotopic mass 140 did not affect the spectroscopic scans, since their product ions did not reach the detector and hence were not counted in the photoion signal. However, they would affect the measured primary ion beam current and therefore any absolute cross-section measurements made with isotope 140.

8.2 Ce^{5+} Photoionization Measurements

Iodine-like Ce^{5+} has the ground-state electronic configuration $[Kr]4d^{10}5s^25p^5$. The fine structure gives rise to the ground-state term $^2P_{3/2}$ and the metastable state $^2P_{1/2}$ lying 3.22 eV above the ground state [26, 27]. There are additional long-lived metastable states of the configuration $[Kr]4d^{10}5p^44f$ which were likely present in the parent ion beam and were considered in interpreting the experimental data [31].

Figure 8.1 shows the absolute photoionization cross section for Ce^{5+} measured in the energy range from 115 eV to 150 eV at 0.1 eV energy resolution. The total experimental

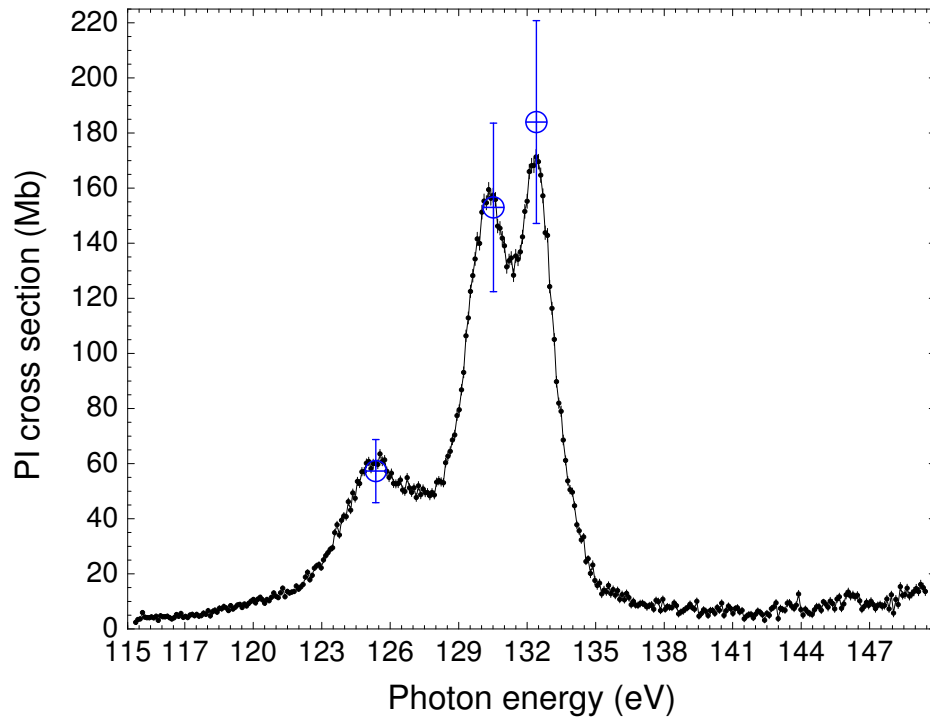


Figure 8.1: Single photoionization cross-section measurements for Ce^{5+} at 0.1 eV energy resolution. The large circles with error bars are absolute measurements to which the spectroscopic scan was normalized.

Table 8.1: Ground state and metastable states of the ground-state configuration of Te-like Ce^{6+} calculated using the online Cowan code [28].

Configuration	Term	Level (eV)	Statistical Weight
$4d^{10}5s^25p^4$	3P_2	0.00	9
$4d^{10}5s^25p^4$	3P_0	1.74	9
$4d^{10}5s^25p^4$	3P_1	2.99	9
$4d^{10}5s^25p^4$	1D_2	4.26	5
$4d^{10}5s^25p^4$	1S_0	8.44	1

oscillator strength is 10.77, which is in agreement with the sum-rule value of 10 within the experimental uncertainty. The structure above 131 eV arises mostly from $4d \rightarrow 4f$ excitation from the $^2P_{3/2}$ ground state and from the $^2P_{1/2}$ metastable state, followed by autoionization. Features below 131 eV are attributed to $4d \rightarrow 4f$ excitation from the $4d^{10}5s^25p^44f$ metastable states of Ce^{5+} followed by autoionization. The measurements suggest that these autoionizing decays occur very rapidly, yielding broad resonances according to Heisenberg's time-energy uncertainty principle.

8.3 Ce^{6+} Photoionization Measurements

Ce^{6+} is a Te-like ion with the ground-state electronic configuration $[Kr]4d^{10}5s^25p^4$ and the ground-state term 3P_2 . The online Cowan Hartree-Fock computer code [28] was used to identify possible metastable states in the primary ion beam. These states and their statistical weights are presented in Table 8.1. Long-lived $[Kr]4d^{10}5s^25p^34f$ metastable states are also relevant to the analysis of the experiment [31].

Absolute photoionization cross-section measurements for Ce^{6+} in the energy range

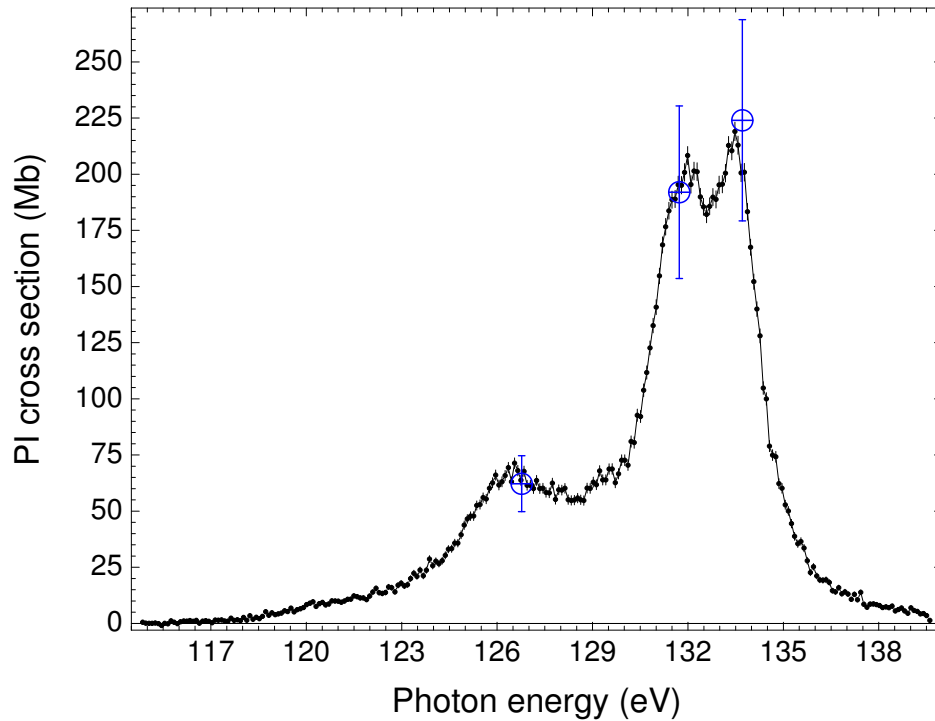


Figure 8.2: Single photoionization cross-section measurements for Ce^{6+} at 0.1 eV energy resolution. The large circles with error bars are absolute measurements.

115 - 140 eV at 0.1 eV resolution are presented in Figure 8.2. Above 132.5 eV, the measured structures are dominated by $4d \rightarrow 4f$ transitions from the ground state 3P_2 and from the metastable states 3P_0 , 3P_1 , 1D_2 , and 1S_0 , followed by autoionization. The structures observed in the range from 115 eV to 132.5 eV are attributed mainly to $4d \rightarrow 4f$ excitation from the $4d^{10}5s^25p^34f$ metastable states of Ce^{6+} , followed by autoionization. The relative contributions of these metastable states to the total measured photoionization oscillator strength of Ce^{6+} (11.4) depends on their proportions in the primary ion beam. For photoionization of a pure ground-state Ce^{6+} ion beam, one would expect only one strong, broad resonance peak centered near 133.5 eV.

Table 8.2: Ground state and metastable states of the ground-state configuration of Sb-like Ce^{7+} calculated using the online Cowan code [28].

Configuration	Term	Level (eV)	Statistical Weight
$4d^{10}5s^25p^3$	$^4S_{3/2}$	0.00	4
$4d^{10}5s^25p^3$	$^2D_{3/2}$	2.95	10
$4d^{10}5s^25p^3$	$^2D_{5/2}$	4.04	10
$4d^{10}5s^25p^3$	$^2P_{1/2}$	5.77	6
$4d^{10}5s^25p^3$	$^2P_{3/2}$	8.30	6

8.4 Ce^{7+} Photoionization Measurements

The Ce^{7+} Sb-like ion has a half-filled 5p outer shell with the ground-state electronic configuration $[Kr]4d^{10}5s^25p^3$ for which the spin-orbit interaction yields the ground-state term $^4S_{3/2}$ and four metastable states, namely, $^2D_{3/2}$, $^2D_{5/2}$, $^2P_{1/2}$, and $^2P_{3/2}$ [28] (see Table 8.2). Long-lived $[Kr]4d^{10}5s^25p^24f$ metastable states were found to be relevant for interpretation of the experimental results [31].

Absolute photoionization cross-section measurements for Ce^{7+} from 115.5 eV to 140.6 eV photon energy at 0.1 eV resolution are presented in Figure 8.3. The structures observed below 128.5 eV are dominated by autoionizing transitions of 4d electrons from the $4d^{10}5s^25p^24f$ metastable states to $4d^95s^25p^24f^2$ excited states. Resonances in the energy range 128.5 - 134 eV are attributed to $4d \rightarrow 4f$ transitions arising from an admixture of the ground state and metastable states. Above 134 eV, the structures are assigned to $4d \rightarrow 4f$ excitations from the $^4S_{3/2}$ ground-state, and $^2D_{3/2}$, $^2D_{5/2}$, $^2P_{1/2}$, and $^2P_{3/2}$ metastable states. The measured photoionization oscillator strength for Ce^{7+} is 12.23, which is larger than the expected value of 10, but not far outside the estimated

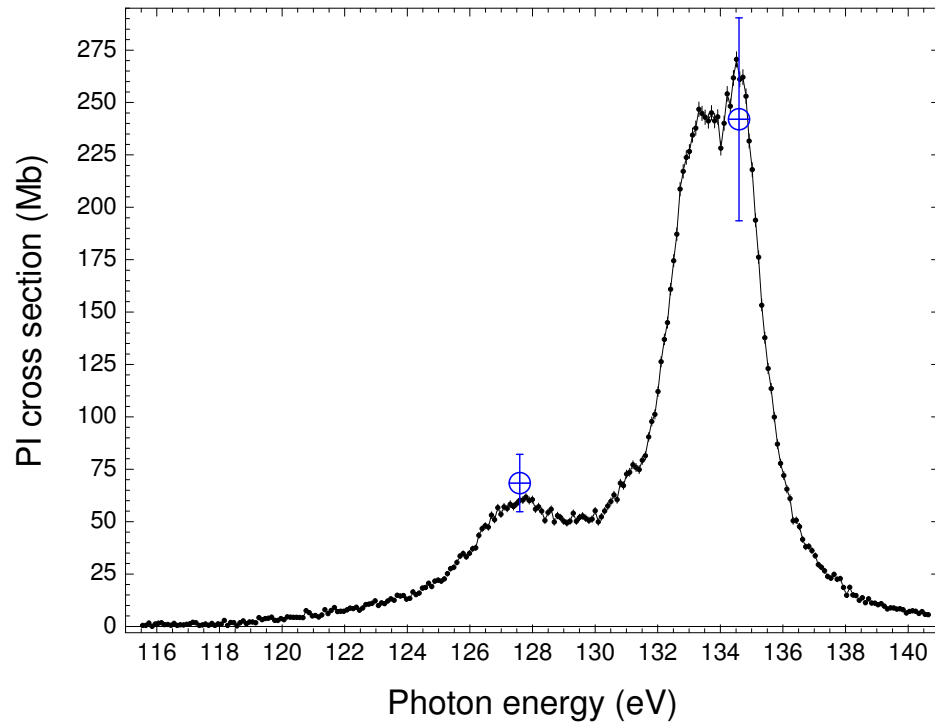


Figure 8.3: Single photoionization cross-section measurements for Ce^{7+} at 0.1 eV energy resolution. The large circles with error bars are absolute measurements.

experimental uncertainty of $\pm 20\%$.

8.5 Analysis and Discussion

The electronic structures of the three ions Ce^{5+} , Ce^{6+} , and Ce^{7+} are similar in their ground states $4d^{10}5s^25p^n$ and their metastable states $4d^{10}5s^25p^{n-1}4f^1$ ($n = 5, 4, 3$, respectively) configurations. That may explain the resemblance of their photoionization cross-section results, as illustrated in Figure 8.4. However, some differences are evident. Figure 8.4 and Table 8.3 present three-Lorentzian curve fits to the experimental photoionization cross sections, which represent the data extremely well. These fits show systematic changes with increasing ionization stage of the parent ion. The increases in

Table 8.3: Comparison of Lorentzian fits to the photoionization cross sections of Ce^{5+} , Ce^{6+} , and Ce^{7+} . Energies, Lorentzian FWHM Γ , maximum cross sections σ_{max} , and oscillator strengths f for each peak and ion charge state are presented.

Peak	Ion Charge	Energy (eV)	Γ (eV)	σ_{max} (Mb)	f
1	5	125.36	4.03	50.30	2.65
	6	126.58	3.67	61.00	2.90
	7	127.66	3.64	52.52	2.48
2	5	130.28	2.42	134.40	4.44
	6	131.75	2.18	179.41	5.24
	7	133.18	2.23	207.30	6.17
3	5	132.45	1.64	138.63	3.15
	6	133.56	1.35	172.17	3.18
	7	134.70	1.34	193.37	3.54

the resonance energies with initial ion charge are expected because of the decrease in screening of the nuclear charge as the number of electrons decrease. In addition, the energy separation ΔE_{23} between the two strongest peaks decreases as the ionic charge increases. As the initial charge state of the ion increases, the maximum cross sections of the higher energy peaks (σ_2 and σ_3) increase. Similarly, the peak cross-section ratios σ_1/σ_2 and σ_1/σ_3 decrease with increasing ion charge. One interpretation of the observed cross-section ratios is that the proportion of the metastable states in the parent ion beam decreases with increasing ionization stage. That might be explained by the increase of the binding energies of the 5p outer-shell electrons with ionic charge along the isonuclear sequence, causing the contributions of metastable states to the total cross section to decrease.

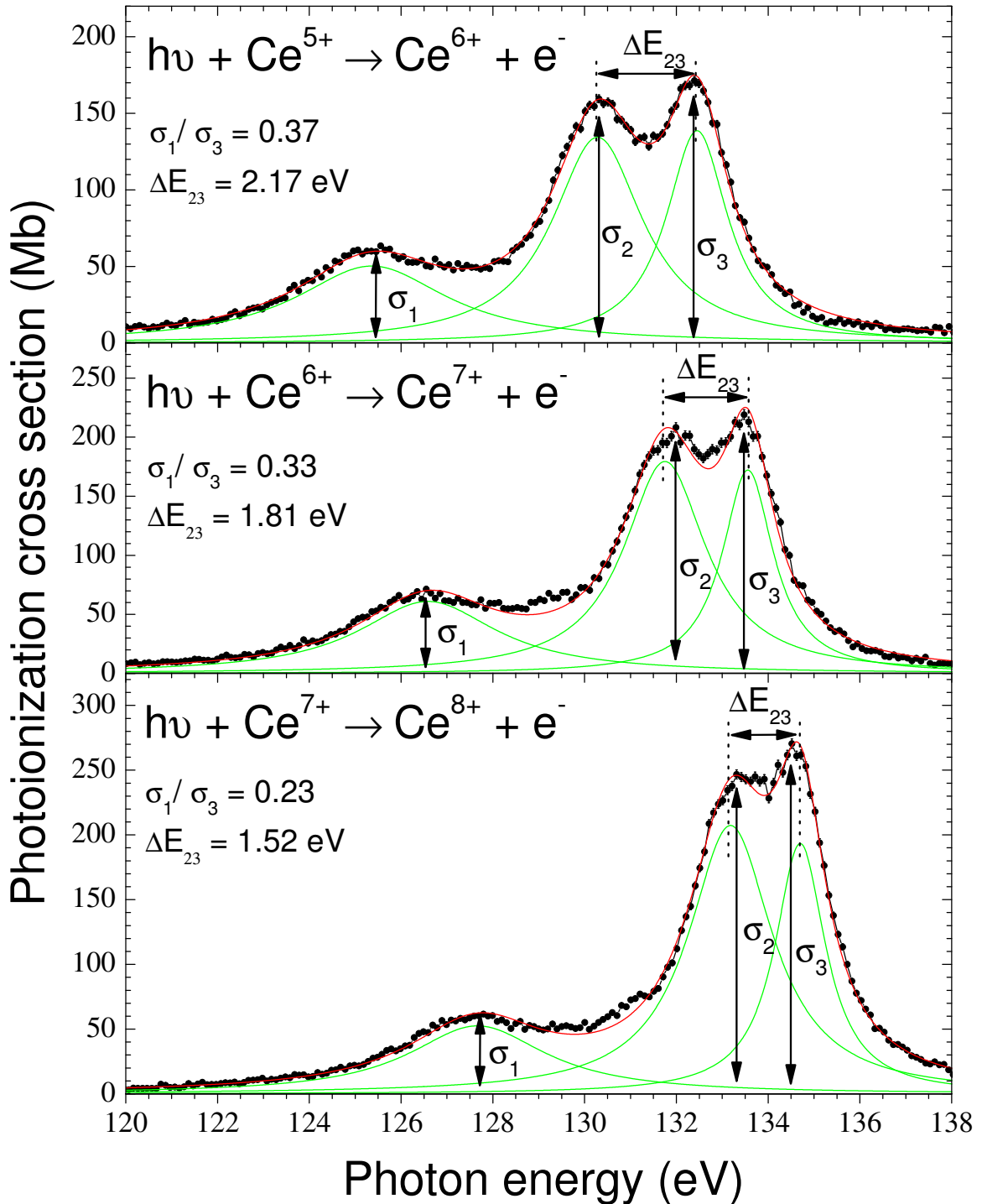


Figure 8.4: Comparison of the photoionization cross sections of Ce^{5+} , Ce^{6+} , and Ce^{7+} . The contribution of metastable states to the cross section decreases with increasing parent ion charge (see text). Lorentzian profiles were used to fit the experimental cross sections.

Chapter 9

Photoionization Measurements for Ce^{8+} and Ce^{9+}

9.1 Introduction

Absolute photoionization cross-section measurements were performed for Ce^{8+} and Ce^{9+} ions in the 4d giant resonance region and are analyzed in this chapter. Both ions have less than half-filled 5p outer shells. In contrast to the lower charge states, narrower resonances become evident in the photoionization cross section of Ce^{8+} and dominate the cross section for Ce^{9+} . The photo-excited states of Ce^{9+} evidently autoionize more slowly than those of Ce^{8+} and much more slowly than the lower charge states. The online Los Alamos National Laboratory (LANL) atomic structure code [28] was used as an aid in identifying the structure in the experimental photoionization cross sections.

9.2 Ce^{8+} Photoionization Measurements

The Sn-like Ce^{8+} ion has the ground-state electronic configuration $[\text{Kr}]4d^{10}5s^25p^2$ for which the Russell-Saunders notation gives the terms 3P_0 for the ground state and 3P_1 , 3P_2 , 1D_2 and 1S_0 for the metastable states. The Cowan code gives a value of 125.2 eV

Table 9.1: Ground state and metastable states of Sn-like Ce^{8+} for the $4d^{10}5s^25p^2$ ground-state and the $4d^{10}5s^25p^14f^1$ metastable-state configurations calculated using the LANL code [28].

Configuration	Term	Statistical Weight	Level (eV)
$5p^2$	3P_0	9	0
$5p^2$	3P_1	9	2.78
$5p^2$	3P_2	9	3.64
$5p^2$	1D_2	5	7.14
$(5p^1\ ^2P)(4f^1\ ^2F)$	3G_3	27	9.25
$(5p^1\ ^2P)(4f^1\ ^2F)$	3F_2	21	9.79
$(5p^1\ ^2P)(4f^1\ ^2F)$	3F_3	21	9.81
$5p^2$	1S_0	1	10.00
$(5p^1\ ^2P)(4f^1\ ^2F)$	3G_4	27	10.02
$(5p^1\ ^2P)(4f^1\ ^2F)$	1F_3	7	12.60
$(5p^1\ ^2P)(4f^1\ ^2F)$	3F_4	21	12.99
$(5p^1\ ^2P)(4f^1\ ^2F)$	3G_5	27	13.52
$(5p^1\ ^2P)(4f^1\ ^2F)$	3D_2	15	13.54
$(5p^1\ ^2P)(4f^1\ ^2F)$	3D_3	15	13.58
$(5p^1\ ^2P)(4f^1\ ^2F)$	3D_1	15	13.97
$(5p^1\ ^2P)(4f^1\ ^2F)$	1G_4	9	14.37
$(5p^1\ ^2P)(4f^1\ ^2F)$	1D_2	5	15.13

for the ionization potential of the ground state [28]. Long-lived $4d^{10}5s^25p^14f^1$ metastable states are also found to be relevant in interpreting the experimental results [31]. These states are presented in Table 9.1.

The Ce^{9+} photoionization signal was recorded in the energy range 110 - 150 eV at a resolution of 0.1 eV and normalized to absolute measurements. The resulting cross section is shown in Figure 9.1. Higher resolution measurements at 0.03 eV resolution in the energy range from 133.25 eV to 136.55 eV are presented in Figure 9.2 (upper panel).

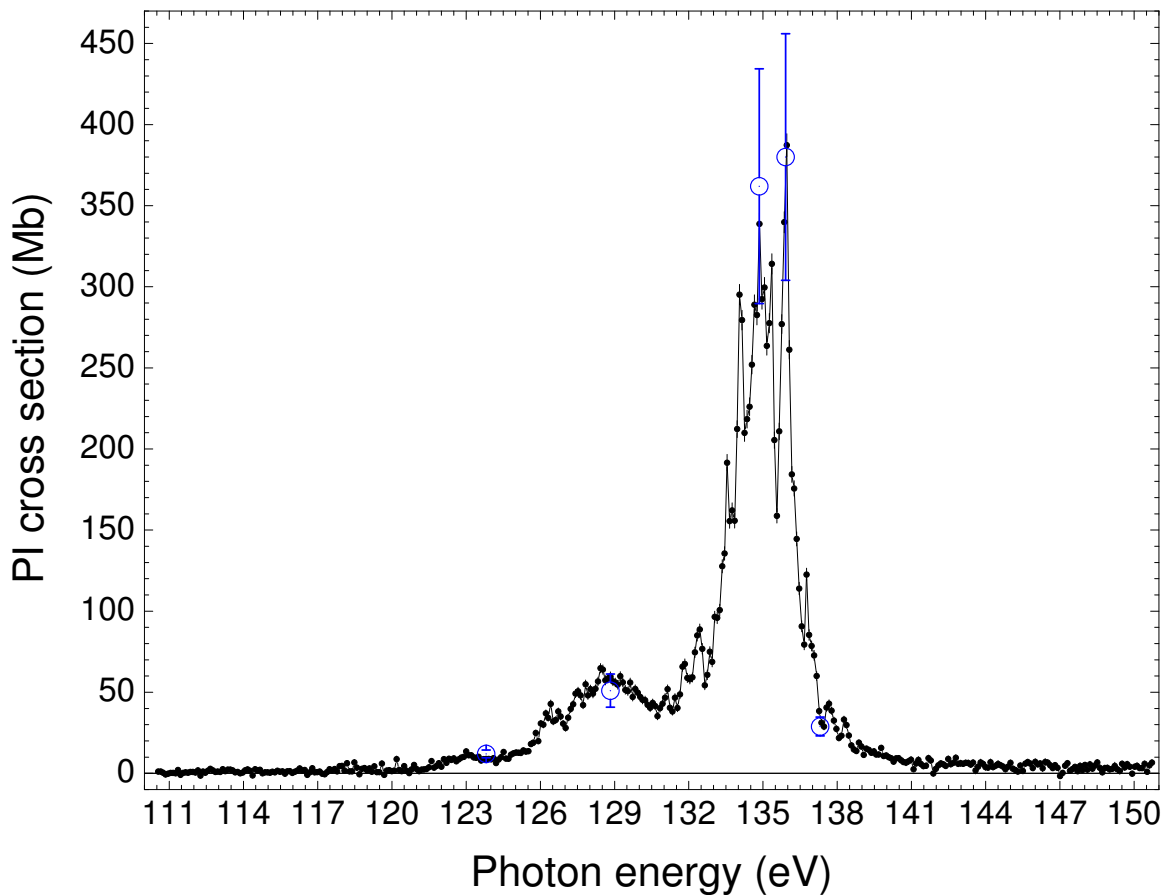


Figure 9.1: Single photoionization cross-section measurements for Ce^{8+} at 0.1 eV energy resolution. The large circles with error bars are absolute measurements to which the spectroscopic data were normalized.

Resonant structure observed below 127 eV is likely due to $5s \rightarrow np$ ($n \geq 8$) transitions. A small step of the cross section near 125 eV is attributed to the opening of the direct photoionization channel of the $5p$ outer shell from the 3P_0 ground state. The cross-section step near 122 eV is interpreted as the photoionization threshold of the 3P_2 metastable state, which lies 3.64 eV above the ground state [28]. However, accurate values of these thresholds could not be determined due to resonances embedded in the cross section

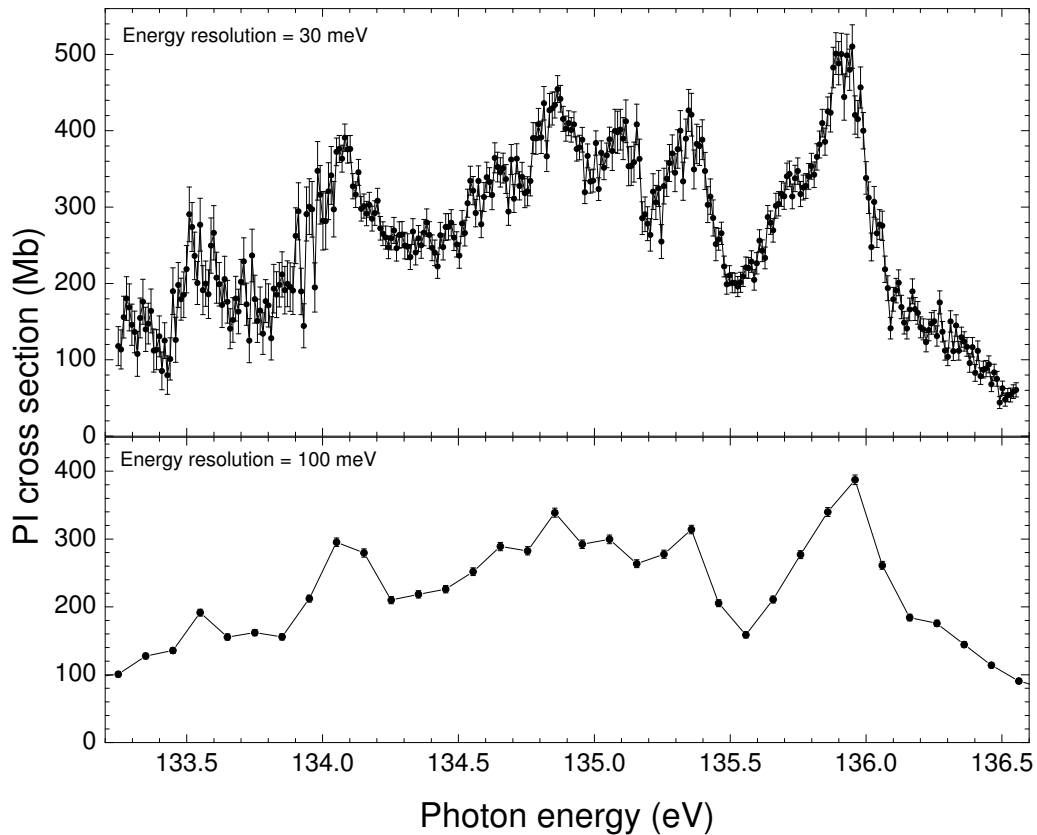


Figure 9.2: Photoionization cross-section measurements for Ce^{8+} at 0.03 eV energy resolution (upper panel) compared to measurements at 0.1 eV resolution (lower panel). The high resolution data were normalized to an absolute scale using the integrated oscillator strength of the low-resolution normalized spectrum (lower panel) in the same energy range.

Table 9.2: Ground state and metastable states of In-like Ce^{9+} ground-state $4d^{10}5s^25p^1$ and metastable-state $4d^{10}5s^24f^1$ configurations calculated using the LANL code [28].

Configuration	Term	Statistical Weight	Level (eV)
$4d^{10}5s^25p^1$	$^2P_{1/2}$	6	0
$4d^{10}5s^25p^1$	$^2P_{3/2}$	6	4.01
$4d^{10}5s^24f^1$	$^2F_{5/2}$	14	7.20
$4d^{10}5s^24f^1$	$^2F_{7/2}$	14	7.57

in this energy range. Features in the energy range 127 - 135.5 eV are attributed to $4d \rightarrow 4f$ transitions from an admixture of the ground state and metastable states, followed by autoionization. The resonances above 135.5 eV are mainly assigned to autoionizing $4d \rightarrow 4f$ excitations from the 3P_0 ground state and the 3P_1 , 3P_2 , 1D_2 and 1S_0 metastable states of the ground-state configuration. Contribution of the direct photoionization of the 5s electrons from the ground state and metastable states is expected above 138 eV [28].

The integrated experimental oscillator strength in the energy range of these measurements is 12.45. A value larger than 10 is to be expected in this case because of direct and resonant contributions to the photoionization cross section from the 5s and 5p subshells.

9.3 Ce^{9+} Photoionization Measurements

Ce^{9+} is an Indium-like ion with the ground-state electronic configuration $[Kr]4d^{10}5s^25p^1$. The spin-orbit interaction gives rise to the terms $^2P_{1/2}$ for the ground state and $^2P_{3/2}$ for the metastable state, for which the calculated fine-structure energy splitting is 4.01 eV [28]. Long-lived $4d^{10}5s^24f^1$ $^2F_{5/2}$ and $^2F_{7/2}$ metastable states are also relevant in interpreting

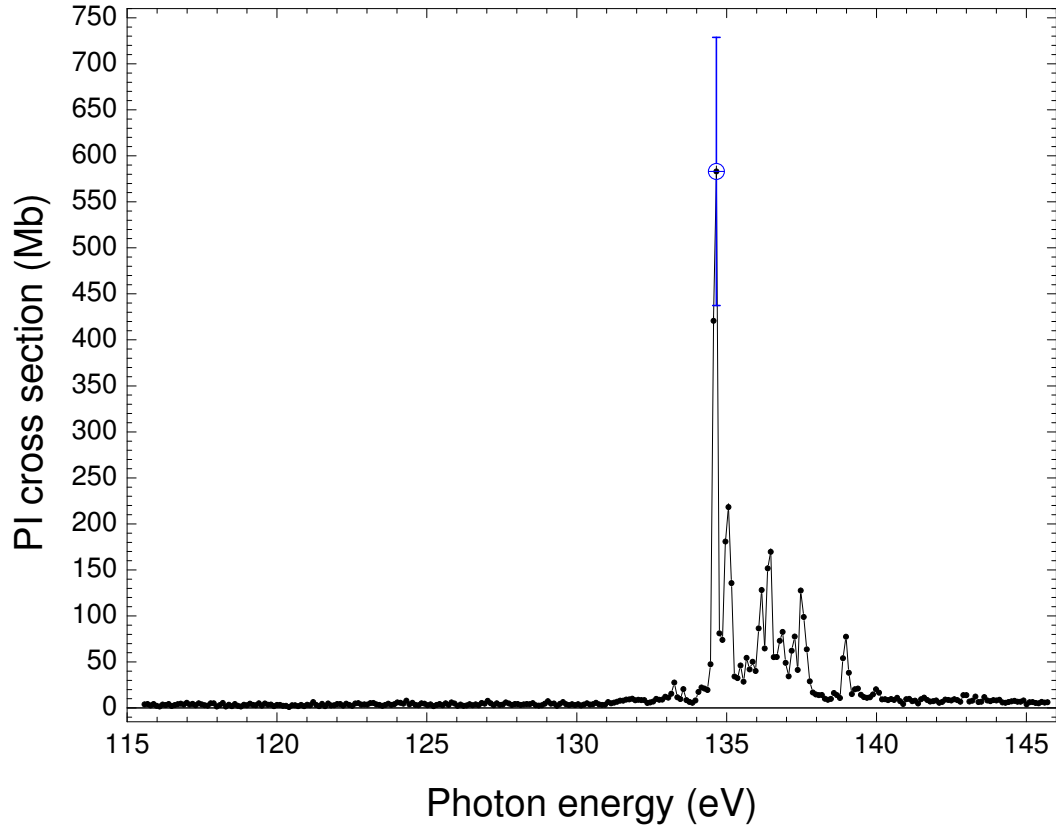


Figure 9.3: Photoionization cross-section measurements for Ce^{9+} at 0.1 eV energy resolution. The large circle with error bar is an absolute measurement.

the experimental results [31]. Table 9.2 shows the calculated energies and configurations of the ground and metastable states. Three sets of cross-section measurements were performed for the photoionization of Ce^{9+} . As an overview, cross-section measurements were made at 0.1 eV energy resolution in the range from 115.6 eV to 145.7 eV. They are shown in Figure 9.3. Measurements were also performed at a higher resolution of 0.05 eV over a narrower energy range (133.7 - 140.6 eV), where strong resonances occur. These measurements are presented in Figure 9.4. Figure 9.5 (upper panel) shows even higher resolution (0.015 eV) measurements for Ce^{9+} in the narrow energy range from 134.533 eV

to 134.716 eV where the strongest resonant feature occurs.

Little evidence for a direct photoionization threshold from the ground state, which is calculated to occur near 140.83 eV [28], was observed in the experimental spectrum. In addition, no structure arising from the ground state was observed in the studied energy range. A step in the cross section near 134 eV is attributed to the photoionization threshold of the $4d^{10}5s^24f^1\ ^2F_{5/2}$ metastable state, which is close to the calculated value of

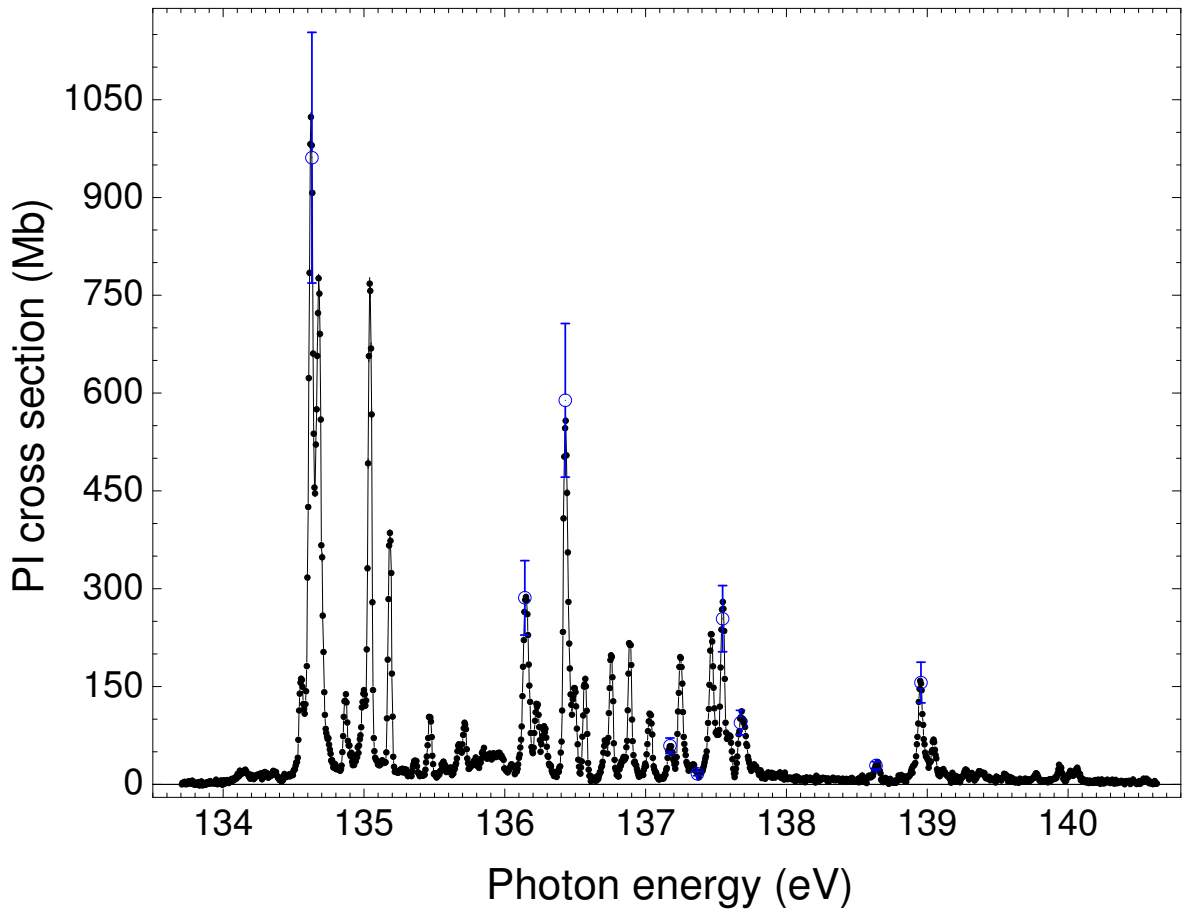


Figure 9.4: Photoionization cross-section measurements for Ce^{9+} at 0.05 eV energy resolution. The large circles with error bars are absolute measurements to which the spectroscopic data were normalized.

133.63 eV [28]. The structures above this threshold up to 136.8 eV are mostly attributed to $4d \rightarrow 4f$ and $4d \rightarrow np$ ($n = 5, 6$) autoionizing excitations from the $^2F_{5/2}$ metastable state, although specific spectroscopic assignments could not be made. A possible small step in the photoionization cross section near 136.8 eV might be due to the onset of direct photoionization of the $4d^{10}5s^25p^1\ ^2P_{3/2}$ metastable state, for which the calculated ionization potential is 136.82 eV [28]. The resonance features above 136.8 eV are assigned

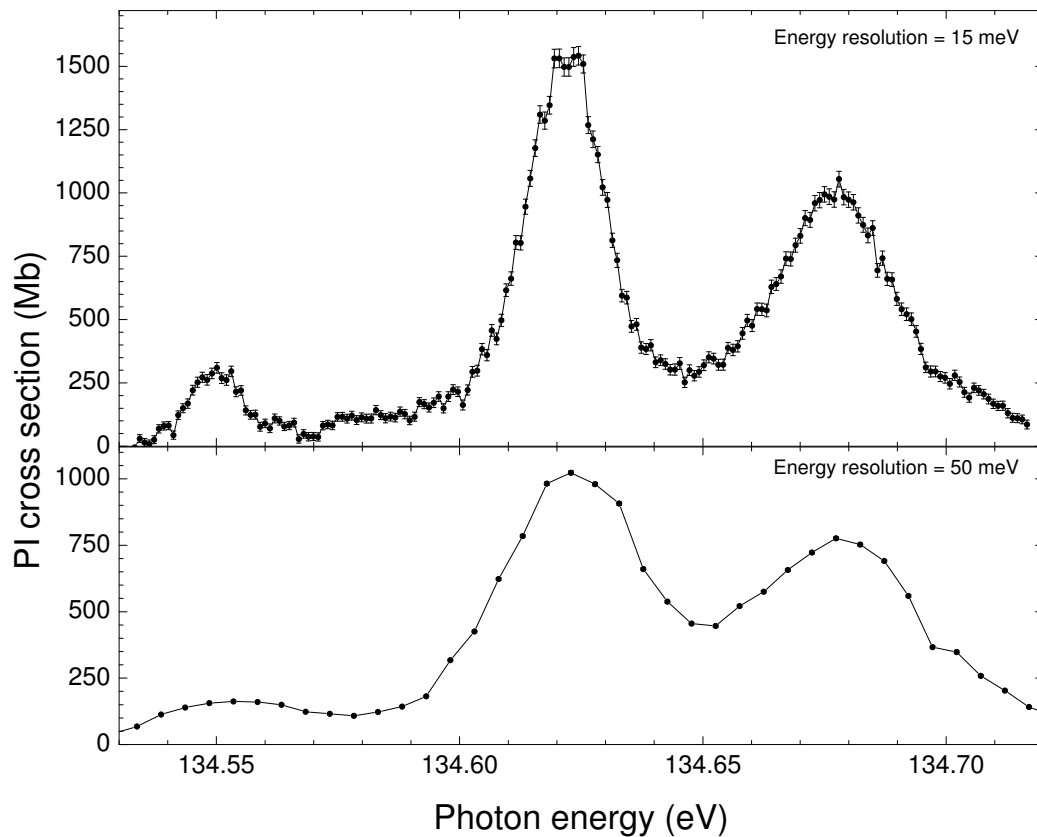


Figure 9.5: Photoionization cross-section measurements for Ce^{9+} at 0.015 eV energy resolution (upper panel) compared to measurements at 0.05 eV resolution (lower panel). The high resolution data were normalized to an absolute scale using the integrated oscillator strength of the low-resolution normalized spectrum (lower panel) in the same energy range.

to autoionizing excitations of 4d electrons to 4f, 5p and 6p from the $4d^{10}5s^25p^1\ ^2P_{3/2}$ metastable state. However, spectroscopic assignments of individual resonance features using the online version of the Cowan code were not possible.

Integration of the photoionization cross section of Ce^{9+} in the energy range 133.7 - 140.6 eV yields an oscillator strength of 3.17. Since the measured photoionization in this energy range originates exclusively from the metastable states, their proportion in the parent ion beam is estimated to be approximately 1/3.

Chapter 10

Photoionization and Photofragmentation Measurements of Endohedral $\text{Ce}@C_{82}^+$

10.1 Introduction

Along with diamond and graphite, fullerenes are distinct allotropes of pure carbon. They are closed-shell molecules composed of 20 or more carbon atoms arranged in a closed geometrical pattern. The most common fullerene is C_{60} , whose discovery in 1985 [32] led to the Nobel prize in chemistry. The carbon atoms form a hollow spherical cage with a diameter of approximately 1 nm. The concept of an atom or a molecule trapped inside a fullerene cage has attracted the interest of experimentalists and theorists in both physics and chemistry. The discovery of the first so-called endohedral fullerene, $\text{La}@C_{60}$, was made by laser vaporization of a lanthanum oxide/graphite composite rod in a flow of Argon gas at 1200 °C by Smalley's group at Rice University [33]. Many theoretical studies and a few experimental measurements have been performed to reveal the characteristics and properties of these exotic species [34, 77, 79].

This chapter presents experimental single and double photoionization cross-section

measurements for the $Ce@C_{82}^+$ endohedral fullerene molecular ion in the energy range of 4d excitations of cerium ions. In addition, photofragmentation cross-section measurements were performed for $Ce@C_{82}^+$ to investigate the 'post decay' interactions of the ejected Auger electrons from the cerium ion with the surrounding carbon atoms of the fullerene cage. For reference, single and double photoionization cross-section measurements were performed for the empty fullerene C_{82}^+ . These and the photoionization measurements for Ce^{q+} ions provide a basis for investigating, by means of comparison, the photoabsorption of the encaged cerium ion [34].

10.2 $Ce@C_{82}^+$ Single Photoionization Measurements

As noted, separate measurements were made of photoionization of endohedral $Ce@C_{82}^+$ and empty C_{82}^+ molecular ions. The $Ce@C_{82}^{2+}$ and C_{82}^{2+} product signals were separately normalized using absolute photoionization measurements for C_{60}^+ [41] in the energy range 80 - 100 eV where no significant contribution of the cerium 4d excitations was expected. This was accomplished on the basis of the Henke model [35], which assumes that the photoabsorption cross section of a molecule is simply given by the sum of the cross sections of each single atom contained in the molecule. Previous cross-section measurements for photoionization of the fullerene molecules C_{84}^+ , C_{80}^+ , C_{70}^+ and C_{60}^+ were consistent with the model prediction that the cross sections for fullerenes scale with the number of carbon atoms. Hence, absolute cross-section values for endohedral $\sigma_{12}(Ce@C_{82}^+)$ and for empty fullerene $\sigma_{12}(C_{82}^+)$ molecular ions were determined from the measured absolute photoionization cross sections for C_{60}^+ such that $\sigma_{12}(C_{82}^+) = \sigma_{12}(Ce@C_{82}^+) = \frac{82}{60} * \sigma_{12}(C_{60}^+)$

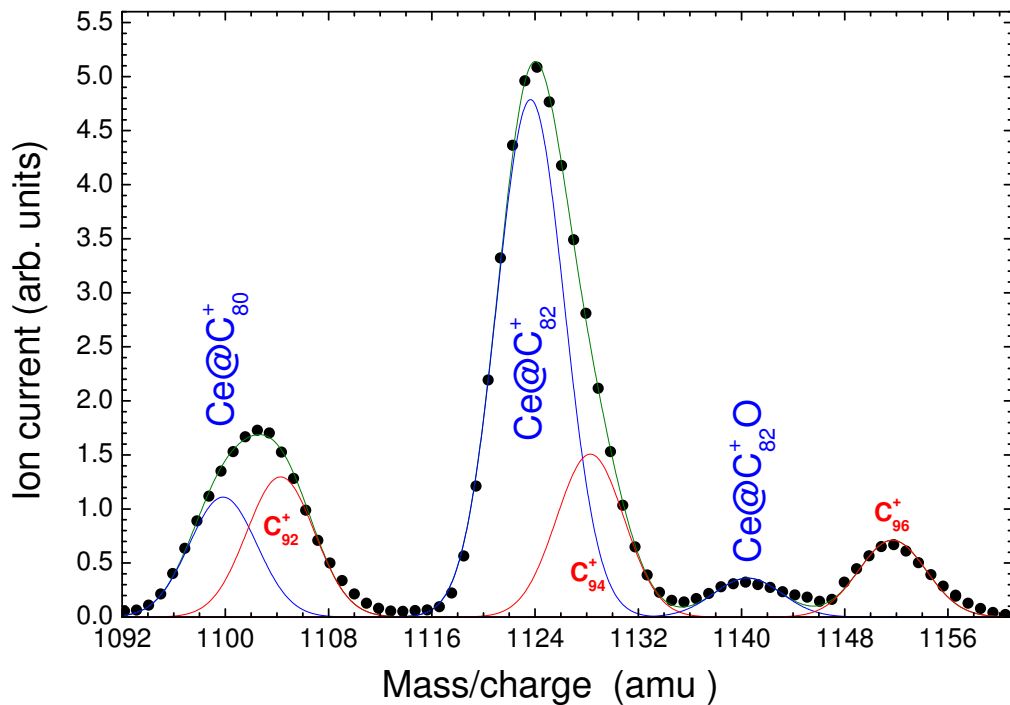


Figure 10.1: Mass spectrum for the endohedral fullerene showing the contamination of $Ce@C_{82}^+$ ion beam with C_{94}^+ . The dots are experimental measurements. The lines present Gaussian fits to the experimental data.

in the energy region where cerium does not contribute significantly to the photoionization cross section.

Based on ion-beam mass spectra obtained under the same conditions as the photon energy scans, the $Ce@C_{82}^+$ ion beam of mass 1124 could not be completely separated from a C_{94}^+ beam of mass 1128. Figure 10.1 presents the mass spectrum with Gaussian fits to the ion current peaks. Taking into account the very small endohedral ion beam current of a few picoAmperes, the mass resolution could not be further increased by closing slits without an unacceptable loss of photoion count rate. From the Gaussian fits, the C_{94}^+ constituent was estimated to be 25% of the primary ion beam. Figure 10.2 shows the

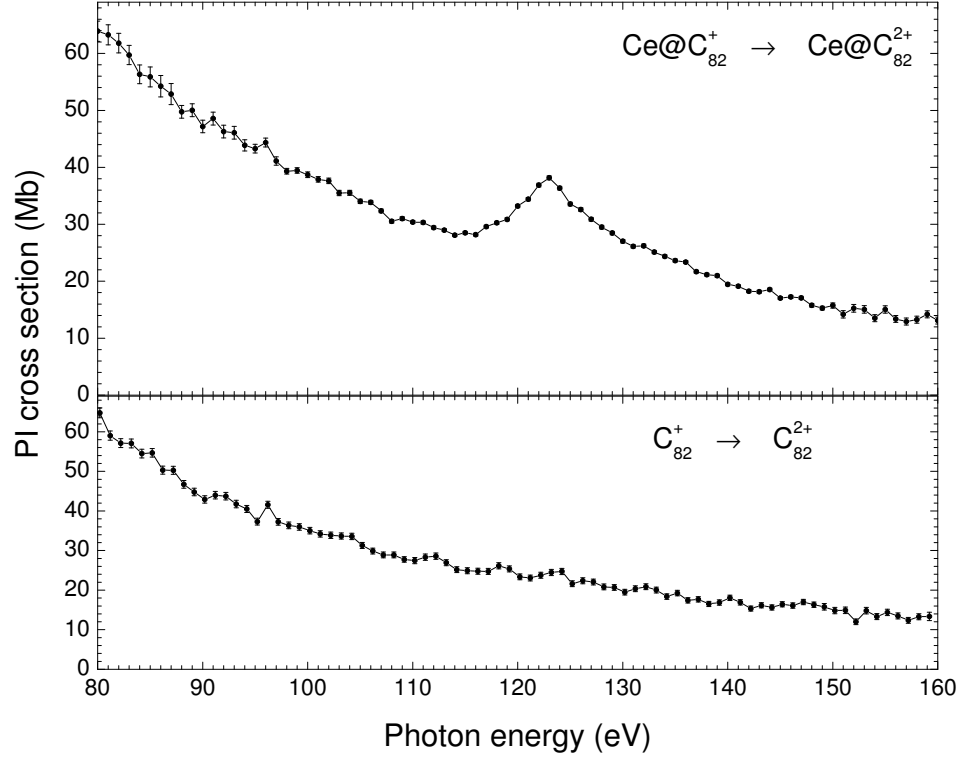


Figure 10.2: Single photoionization cross-section measurements for $Ce@C_{82}^+$ (upper panel) and C_{82}^+ empty fullerene (lower panel). The feature centered at 123 eV (upper panel) is due to $4d \rightarrow nl$ autoionizing excitations of the encapsulated cerium ion.

enhancement in the measured photoionization cross section for the $Ce@C_{82}^+$ (top panel) compared to that for C_{82}^+ (bottom panel) in the cerium 4d giant resonance energy region. The excess in the $Ce@C_{82}^+$ cross section due to the cerium 4d contribution was scaled by $4/3$ to account for the C_{94}^+ component in the primary ion beam.

A detailed analysis of the experimental data was performed to investigate different photoabsorption and decay mechanisms of the encapsulated cerium atom in the reductive environment presented by the fullerene cage. An important issue to be resolved for an

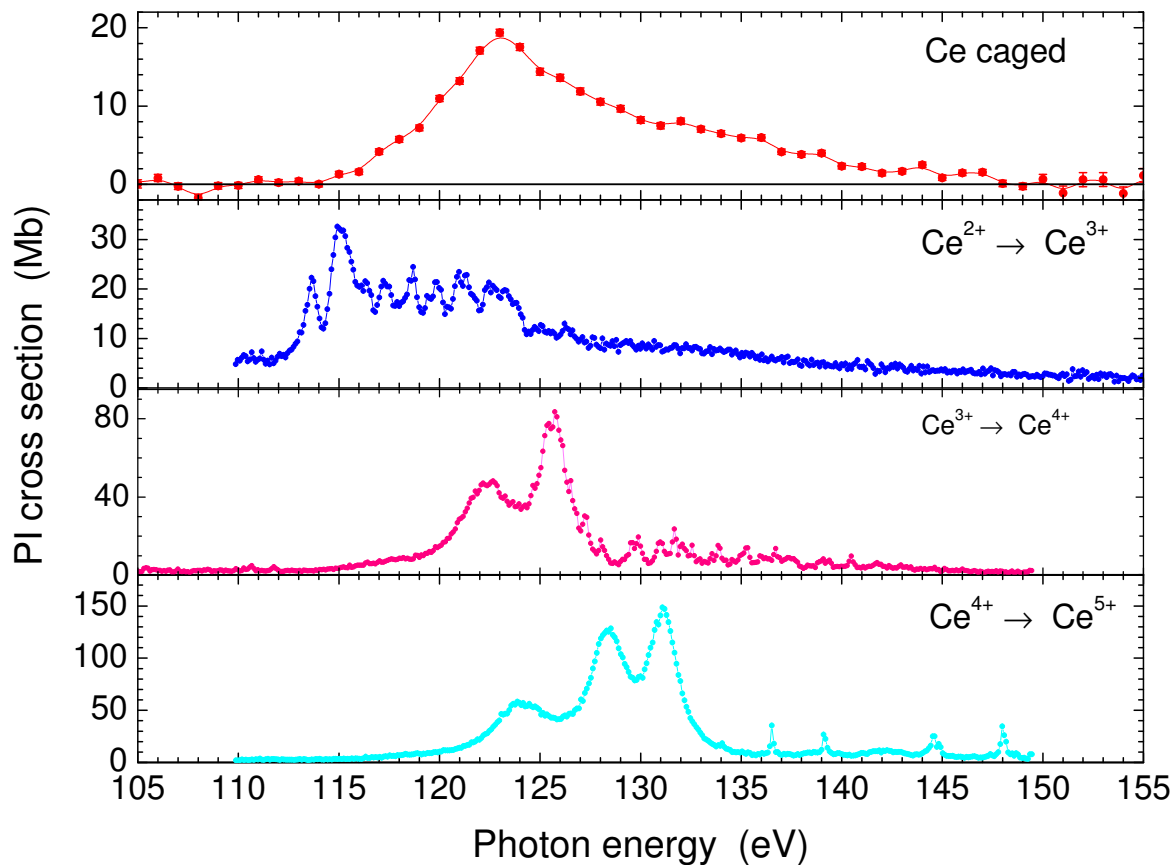


Figure 10.3: Comparison of single photoionization cross sections for Ce^{q+} ions ($q = 2, 3, 4$) and the excess single photoionization cross section of the endohedral fullerene $Ce@C_{82}^+$, to determine the valency of the encapsulated cerium atom.

endohedral molecule is the valence state of the encapsulated atom. A previous experimental study of the electronic properties of $Ce@C_{82}$ in bulk using the time-differential perturbed angular correlation method [39] concluded that the encapsulated cerium atom is trivalent. A comparison between the experimental cross sections for Ce^{q+} ions ($q = 2, 3, 4$) and the excess cross section of the endohedral $Ce@C_{82}^+$ (obtained by subtracting $\sigma(C_{82}^+)$ from $\sigma(Ce@C_{82}^+)$) supports this conclusion. Figure 10.3 indicates that the best match for the endohedral single photoionization excess cross section, in terms of the

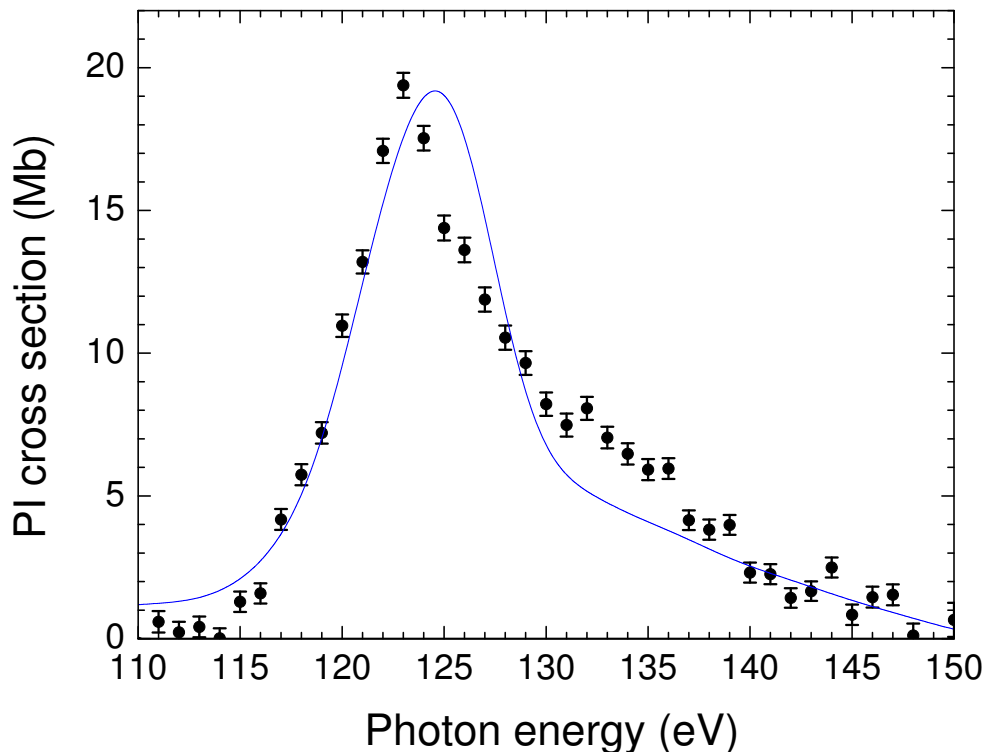


Figure 10.4: Contribution of single photoionization of Ce^{3+} to the excess cross section for single photoionization of $Ce@C_{82}^+$. The solid curve is a convolution of a 5 eV FWHM Gaussian with the measured Ce^{3+} single photoionization cross section, scaled by an empirical factor of 0.45. See text for details.

resonance energy, is that of Ce^{3+} . Furthermore, convoluting the single photoionization cross section for Ce^{3+} with a 5 eV Gaussian, to account for molecular hybridization, and scaling it by a factor of 0.45 represents the measured 4d contribution in σ_{12} of the endohedral fullerene reasonably well, as shown in Figure 10.4. Single ionization accounts for approximately 25% of the total measured photoabsorption oscillator strength of the Ce^{3+} ion ($f = 8.67$).

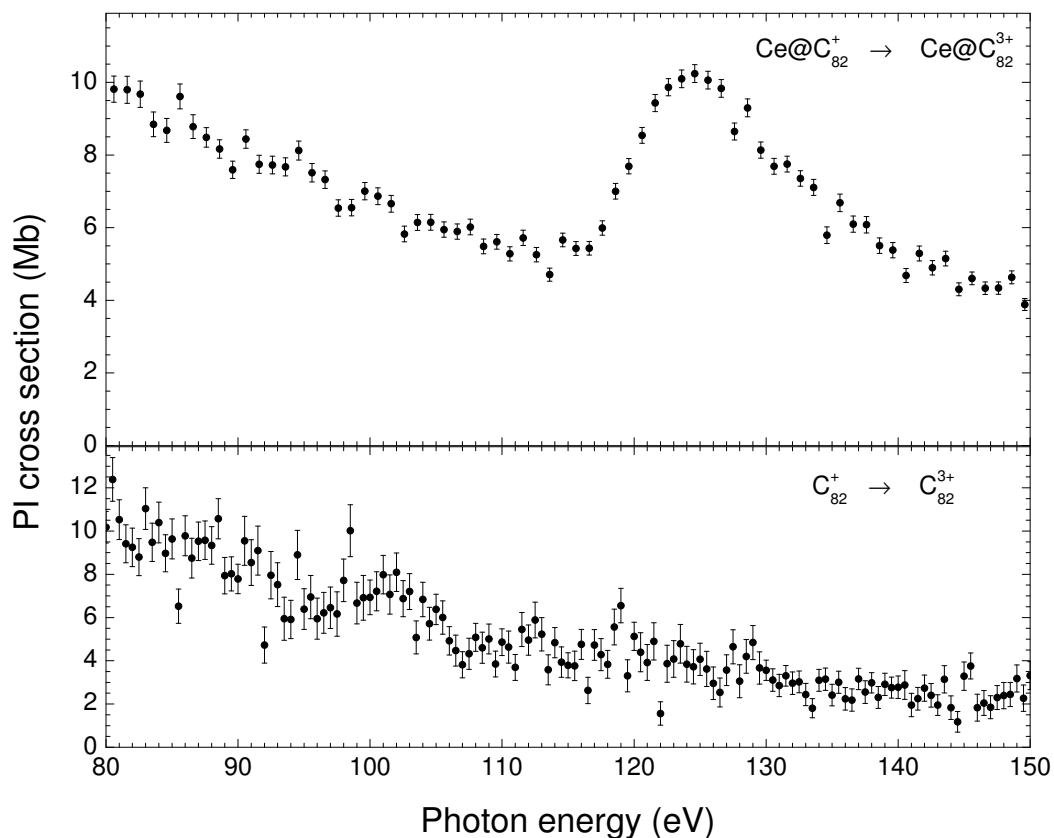


Figure 10.5: Double photoionization cross-section measurements for $Ce@C_{82}^+$ (upper panel) and C_{82}^+ empty fullerene (lower panel). The feature centered at 124.6 eV (upper panel) is due to $4d \rightarrow nl$ autoionizing excitations of the encapsulated cerium ion.

10.3 $Ce@C_{82}^+$ Double Photoionization Measurements

Ratios of photoion yields for single and double photoionization were measured for $Ce@C_{82}^+$ and C_{82}^+ for the purpose of scaling the double photoionization cross sections of both species. Figure 10.5 shows the contribution of $4d$ excitation in the double photoionization cross section of $Ce@C_{82}^+$. The double photoionization spectrum of the empty fullerene is shown in the figure as a comparison to emphasize the cerium $4d$ feature with respect to the empty cage. The single and double photoionization cross sections of Ce^{3+} were

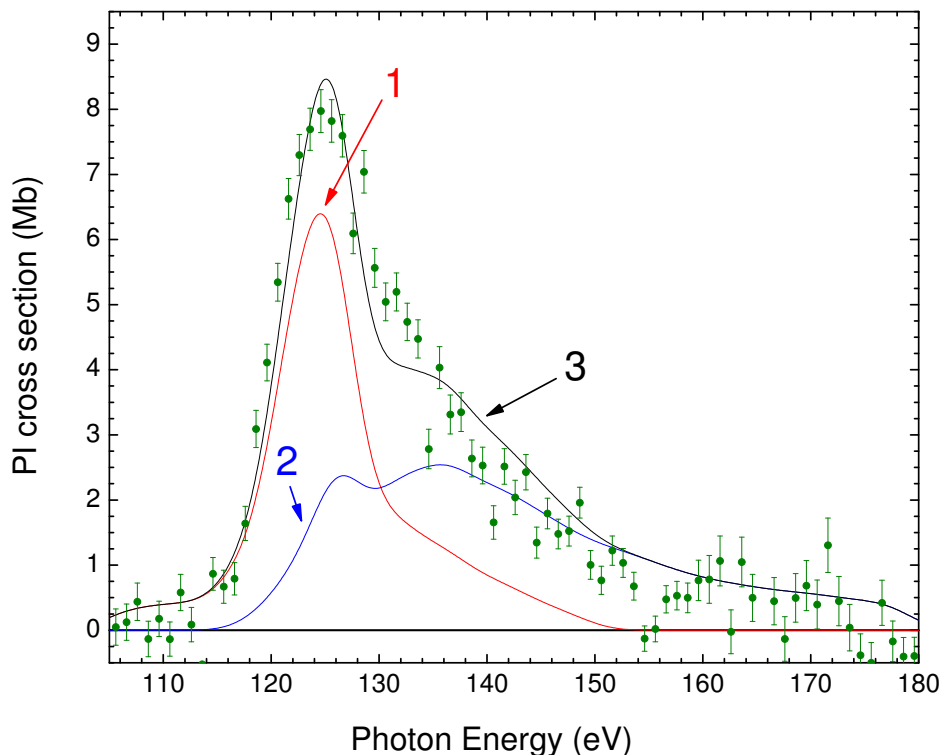


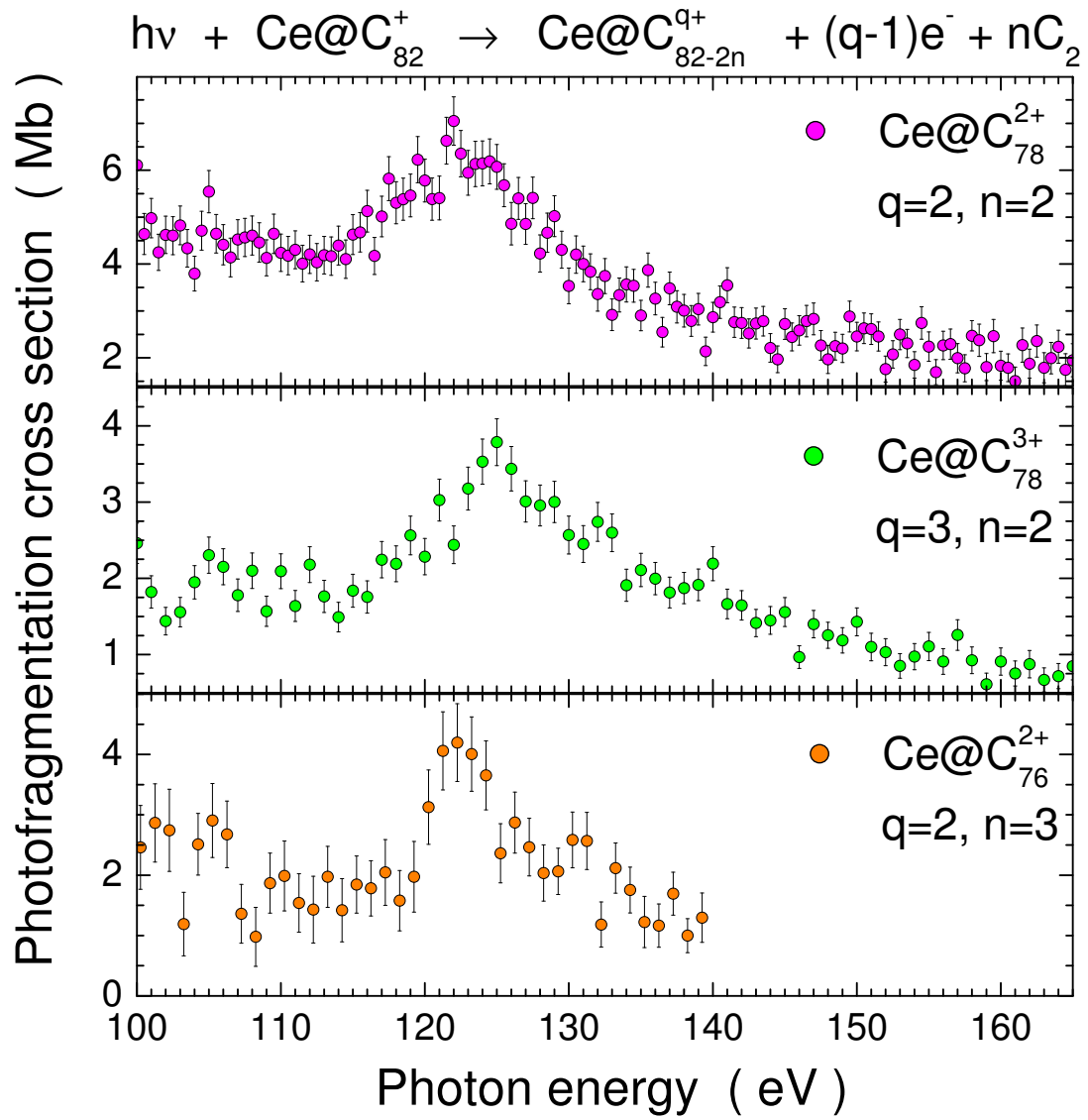
Figure 10.6: Contribution of 4d excitations of Ce^{3+} to the double photoionization cross section of $Ce@C_{82}^+$. The data points with error bars are the difference between the double photoionization cross sections for $Ce@C_{82}^+$ and C_{82}^+ . Curve 1: 15% of single photoionization cross section (σ_{34}) of Ce^{3+} convoluted with a 5 eV Gaussian. Curve 2: 22% of σ_{35} cross section of Ce^{3+} convoluted with a 5 eV Gaussian. Curve 3: sum of curves 1 and 2.

convoluted with a 5 eV Gaussian profile to account for the hybridization effects in the endohedral molecule. An empirical superposition of 15% and 22% of the convoluted cross sections for single and double photoionization of Ce^{3+} , respectively, agrees well with the 4d contribution to the double photoionization cross section of the cerium endohedral (see Figure 10.6). This accounts for 17% of the total measured absorption oscillator strength of Ce^{3+} .

The total integrated excess cross sections over the investigated energy range for single and double photoionizations of the $Ce@C_{82}^+$ endohedral fullerene yields an oscillator strength of 3.6, representing only 42% of the total oscillator strength of the free Ce^{3+} ion. This situation led to other hypotheses to explain the missing 58% of the photoabsorption oscillator strength in the endohedral system.

10.4 $Ce@C_{82}^+$ Photofragmentation Measurements

To explore this issue, other decay channels for the relaxation of the cerium 4d vacancy in the endohedral fullerene were investigated, bearing in mind that additional processes could take place as a result of interaction of the ejected cerium electron with the cage. Electron scattering, electron capture and electron-impact ionization and fragmentation subsequent to photoionization of the encapsulated cerium ion could occur as relaxation processes. Evidence for photofragmentation of the $Ce@C_{82}^+$ endohedral was confirmed by measuring the $Ce@C_{78}^{2+}$, $Ce@C_{78}^{3+}$ and $Ce@C_{76}^{2+}$ product ion yields produced by photofragmentation of the $Ce@C_{82}^+$ parent ion. Photofragmentation cross sections were determined from these measurements for $Ce@C_{82}^+$ in a similar manner to that described above for double photoionization. Figure 10.7 presents some of these measurements, showing the important contributions of these fragmentation-plus-ionization channels. The estimated 4d oscillator strength for these channels is 0.1, accounting for only another 1% of the Ce^{3+} 4d oscillator strength. However, many more fragmentation channels are possible than could be measured in the experiment, for example those yielding neutral heavy fragments.

Figure 10.7: Photofragmentation cross-section measurements for $Ce@C_{82}^+$.

Chapter 11

Summary, Conclusions and Future Outlook

Photoionization cross sections for ions of the cerium isonuclear sequence from Ce^+ through Ce^{9+} and for the cerium endohedral fullerene molecular ion $\text{Ce}@\text{C}_{82}^+$ were investigated by an ion-photon merged-beams technique using monochromatized synchrotron radiation. Competition between continuum and discrete electronic transitions from the filled 4d subshell was observed along this ionic sequence, supporting the theoretical predictions for the collapse of the nf orbitals. Enhancement of the photoionization cross section for $\text{Ce}@\text{C}_{82}^+$ due to 4d excitation/ionization of the encaged cerium ion is evident as a broad resonance feature superimposed on the cross section for empty C_{82}^+ .

11.1 Summary and Conclusions

11.1.1 Cerium Ions

Energy ranges and resolutions used for the photoionization cross-section measurements for cerium ions in the 4d excitation region are summarized in Table 11.1. Absolute cross-section measurements were performed at discrete photon energies for each cerium

ionization stage, except for the quadruple ionization of Ce^+ where it was impossible to collect the parent and the product ion beams simultaneously due to the 4:1 charge ratio of the two beams. The cerium isotope of mass 142 was used for absolute measurements for Ce^{5+} and Ce^{7+} to overcome contamination of the primary ion beam using the 140 mass isotope. Metastable states are present in all the parent ion beams, which complicates the analysis of the cross sections. Fractions of the primary ion beams in metastable states were estimated to be $1/4$ for Ce^{4+} and $1/3$ for Ce^{9+} .

Figure 11.1 compares the total photoionization cross-section measurements for Ce^+ through Ce^{9+} ions and their associated oscillator strengths in the photon energy range of 4d excitations. A broad asymmetric resonance dominates the cross section of Ce^+ , whereas the cross section of Ce^{2+} is characterized by strong resonances below the 4d threshold and a delayed onset of direct photoionization. The Ce^{2+} cross section due to continuum excitations of the 4d electrons decreases monotonically on the high-energy side. Strong and broad peaks dominate the cross section of Ce^{3+} , which also exhibits discrete and narrow, but weaker, resonances. The direct photoionization cross section of Ce^{3+} is much smaller than that for Ce^+ and Ce^{2+} , indicating competition between discrete and continuum photoionization processes with increasing ionization stage. Four Rydberg series were assigned in the single and double photoionization of Ce^{3+} arising from $4d \rightarrow nf$ and $4d \rightarrow np$ transitions. In the Ce^{4+} cross section, the direct photoionization is almost negligible and only discrete transitions are observed, which is the case for all the higher charge states. That indicates the complete collapse of the nf wavefunctions into the inner well of the Coulomb potential that binds the electrons of the 4d subshell.

Table 11.1: Summary of energy ranges and resolutions used in the photoionization cross-section measurements for cerium ions.

Target (eV)	Ionization Degree	Energy Range (eV)	Energy Resolution (eV)
Ce ⁺	Single	105–160	0.1
	Double	105–160	0.1
	Triple	105–160	0.1
	Quadruple	130–160	0.1
Ce ²⁺	Single	105–174	0.1
	Double	105–170	0.1
	Triple	120–160	0.1
Ce ³⁺	Single	105–150	0.1
	Double	105–180	0.1
Ce ⁴⁺	Single	110–150	0.1
	Single	122.8–125.8	0.05
	Single	135.8–139.7	0.05
	Single	143.5–145.5	0.1
	Double	130–180	0.1
Ce ⁵⁺	Single	115–150	0.1
Ce ⁶⁺	Single	115–140	0.1
Ce ⁷⁺	Single	115.5–140.6	0.1
Ce ⁸⁺	Single	110–150	0.1
	Single	133.3–136.5	0.03
Ce ⁹⁺	Single	115.6–145.7	0.1
	Single	133.7–140.6	0.05
	Single	134.533–134.716	0.015

This is a consequence of nuclear attraction dominating over the screening effect due to electron-electron interactions. In the case of Ce^{8+} , strong, narrow resonances arising from $4d \rightarrow 4f$ autoionizing excitations dominate the photoionization cross section. Direct and indirect photoionization of the 5s and 5p subshells are also evident in the Ce^{6+} , Ce^{7+} and Ce^{8+} cross sections, which accounts for the higher photoabsorption oscillator strengths in the experimental energy range for these ions. The Ce^{9+} cross section is dominated by more slowly autoionizing excitations of the 4d electrons originating exclusively from the metastable states of this ion.

11.1.2 Cerium Endohedral Fullerene

Cross-section measurements for single and double photoionization of the $\text{Ce}@C_{82}^+$ endohedral and C_{82}^+ fullerenes were performed in the photon energy range of the cerium 4d giant resonance. On the basis of the Henke model [35], $\text{Ce}@C_{82}^+$ and C_{82}^+ single photoionization spectra were normalized using the absolute photoionization measurements for C_{60}^+ [41] in the range where no cerium 4d excitations are expected. Double-to-single photoionization cross-section ratios of the endohedral and empty fullerene molecular ions were measured in order to scale their double photoionization cross sections. The excess cross section of the endohedral fullerene was reduced by 25% to account for a C_{94}^+ constituent in the parent ion beam. The trivalency of the encapsulated cerium atom predicted by theoretical calculations [43] was verified by the measurements.

Clear signatures due to 4d photoabsorption of the engaged cerium ion were observed

in the single and double photoionization cross sections of the endohedral fullerene molecular ion. The measured 4d photoabsorption oscillator strength of the confined cerium ion is approximately 42% of that measured for the free Ce^{3+} ion. Mechanisms involving the interaction of the ejected electron from the encapsulated cerium ion with the surrounding carbon cage and fragmentation of the cage were postulated to account for this observation [34].

11.2 Outlook

Due to limitations in the beamtime available at ALS, several measurements were performed at photon energy resolutions and step sizes that were not sufficient to identify all the narrow resonance features, especially for the higher ionization stages of cerium. Re-examining these cross sections with higher energy resolution and finer steps would be beneficial in assigning the spectroscopic features. Furthermore, methods for measuring photoionization cross sections of ions in a single initial quantum state, i.e. the ground state, would waive the complications of analyzing experimental data arising from a mixture of initial states. A recent example is the coupling of an ion trap with synchrotron radiation source, which permitted a measurement of the photoionization cross section of Xe^+ in its pure ground state [44].

Endohedral fullerenes are novel forms of fullerene-based materials that have fascinated a broad scientific community during the last twenty years and have potentially important applications. Few quantitative experimental investigations have been conducted for these exotic species. Measurements of photoionization cross section of trapped inert gas atoms

in fullerene molecules would be a great step forward in benchmarking the numerous theoretical calculations that have been performed to examine their properties. Although noble gas endohedral fullerenes have been found in nature in meteor impact craters [57, 58], they are not currently available in quantities sufficient for experiments, and methods for their production on line in ion-atom collisions [59] merit further investigation.

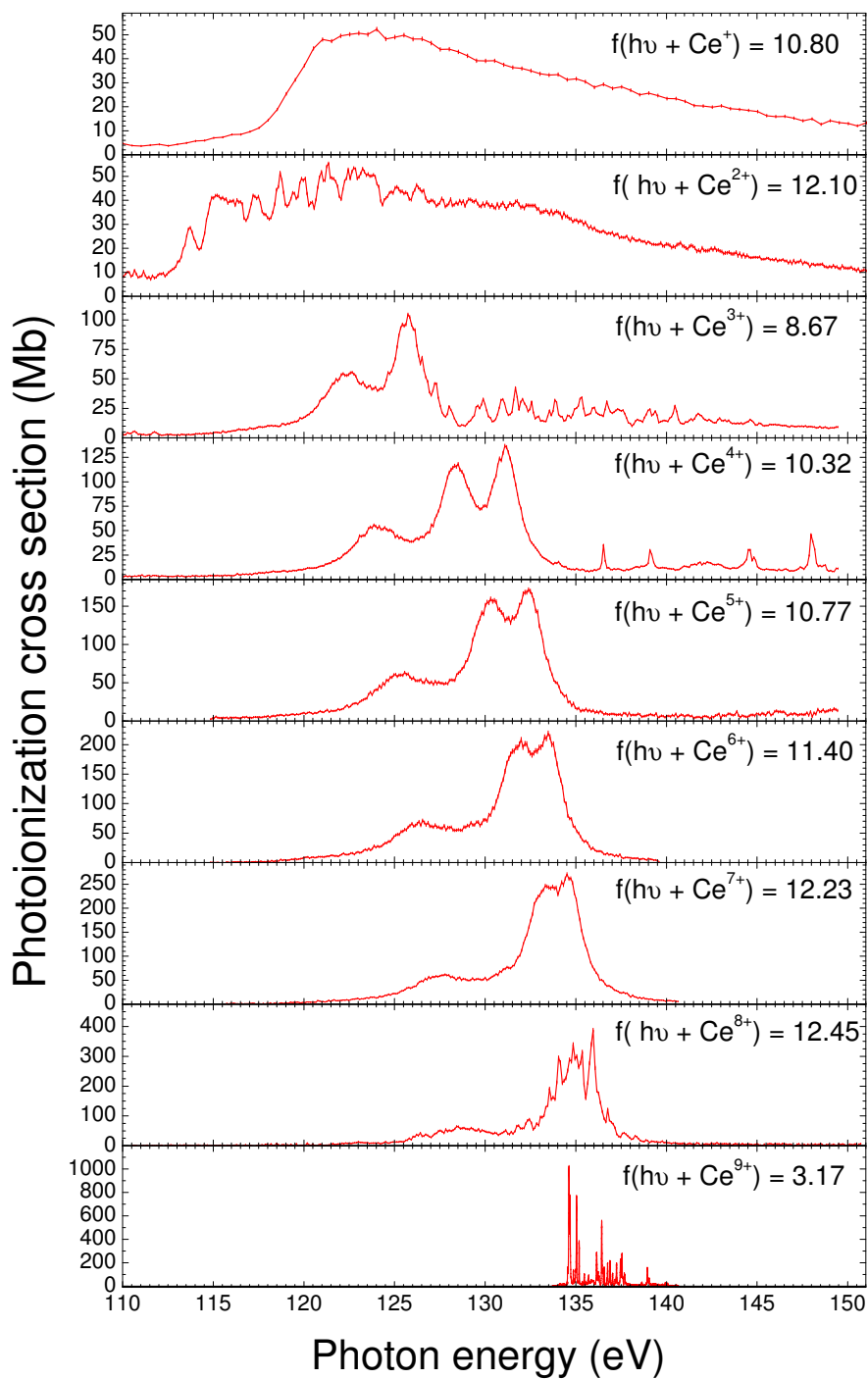


Figure 11.1: Total photoionization cross sections for the cerium isonuclear sequence from Ce^+ through Ce^{9+} with their total photoabsorption oscillator strengths f .

References

- [1] P. Andersen, T. Andersen, F. Folkmann, V. K. Ivanov, H. Kjeldsen, J. B. West. Absolute Cross Sections for the Photoionization of 4d Electrons in Xe^+ and Xe^{2+} Ions. *J. Phys. B: At. Mol. Opt. Phys.*, **34**:2009, 2001.
- [2] S. Baier, U. Koble, T. Luhmann, M. Martins, M. Richter, P. Zimmermann. Photoion Spectroscopy of Atomic Ho, Er and Tm in the Region of the 4d Giant Resonances. *J. Phys. B: At. Mol. Opt. Phys.*, **26**:4091, 1993.
- [3] U. Becker, T. Preshter, B. Sontag, H. E. Wetzel. Decay Channels of the Discrete and Continuum Xe 4d Resonances. *Phys. Rev. A.*, **33**:3891, 1986.
- [4] E. Biémont, P. Quinet. A Database of Astrophysical Interest Covering the UV Region. *J. Elect. Spec. Rel. Phen.*, **144-147**:23-25, 2005.
- [5] E. Biémont, P. Quinet, T. A. Ryabchikova. Core-Polarization Effects in Doubly Ionized Cerium (Ce iii) for Transitions of Astrophysical Interest. *Mon. Not. R. Astron. Soc.*, **336**:1155, 2002.
- [6] E. Biémont, P. Quinet. Recent Advances in Study of Lanthanide Atoms and Ions. *Phys. Scr.*, **T105**:38-54, 2003.
- [7] J. M. Bizau, D. Cubaynes, J. M. Esteva, F. J. Wuilleumier, C. Blancard, J. Bruneau, J. P. Champeaux, A. Compant La Fontaine, C. Couillaud, R. Marmoret, C. Rémond, D. Hitz, M. Delaunay, N. Haque, P. C. Deshmukh, H. L. Zhou, S. T. Manson. Absolute Measurements and Theoretical Calculations of Photoionization Cross Sections Along the Isonuclear Sequence of Multiply Charged Barium Ions. *Phys. Rev. Lett.*, **87**:273002, 2001.
- [8] J. M. Bizau, D. Cubaynes, M. Richter, F. J. Wuilleumier, J. Obert, J C Putaux, T J Morgan, E Källne, S Sorensen, A Damany. First Observation of Photoelectron Spectra Emitted in the Photoionization of a Singly Charged-Ion Beam with Synchrotron Radiation. *Phys. Rev. Lett.*, **67**:576, 1991.

- [9] J. M. Bizau, D. Cubaynes, P. Gérard, and F. J. Wuilleumier. Photoionization of Atomic Barium Ba Atoms in the Ground State. *Phys. Rev. A*, **40**:3002, 1989.
- [10] J. M. Bizau, J. M. Esteva, D. Cubaynes, F. J. Wuilleumier, C. Blancard, A. Compant La Fontaine, C. Couillaud, J. Lachkar, R. Marmoret, C. Rémond, J. Bruneau, D. Hitz, P. Ludwig, M. Delaunay. Photoionization of Highly Charged Ions Using an ECR Ion Source and Undulator Radiation. *Phys. Rev. Lett.*, **84**:435, 2000.
- [11] J. M. Bizau, C. Blancard, D. Cubaynes, F. Folkmann, J. P. Champeaux, J. L. Lemaire, F. J. Wuilleumier. Absolute Photoionization Cross Sections Along the Xe Isonuclear Sequence Xe^{3+} to Xe^{6+} . *Phys. Rev. A*, **73**:022718, 2006.
- [12] J.M. Bizau, E. Bouisset, C. Blancard, J.P. Champeaux, A. Compant la Fontaine, C. Couillaud, D. Cubaynes, D. Hitz, C. Vinsot, F.J. Wuilleumier. Recent Results on the Photoionization of Multiply-Charged Ions. *Nuc. Inst. Meth. Phys. Res. B*, **205**:290, 2003.
- [13] C. Bonnelle, P. Motais. 4f-3d Emission Spectra of the Rare Earths: An Interpretation of the Lines Observed on Both Sides of the Resonances. *Phys. Rev. A*, **73**:042504, 2006.
- [14] Donald J. Bord, Charles R. Cowley, Peggy L. Norquist. Oscillator Strength Calculations in Ce III: Application to HD 200311. *Mon. Not. R. Astron. Soc.*, **284**:869, 1997.
- [15] F. Broetz, R. Trassel, R. W. McCullough, W. Arnold, E. Salzborn. Design of Compact All-Permanent Magnet Electron Cyclotron Resonance (ECR) Ion Sources for Atomic Physics Experiments. *Phys. Scripta.*, **T92**:278, 2001.
- [16] K. T. Cheng, C. Froese Fisher. Collapse of the 4f Orbital for Xe-like Ions. *Phys. Rev. A*, **28**:2811, 1983.
- [17] K. T. Cheng, W. R. Johnson. Orbital Collapse and the Photoionization of the Inner 4d Shells for Xe-like Ions. *Phys. Rev. A*, **28**:2820, 1983.

- [18] John W. Cooper. Interaction of Maxima in the Absorption of Soft X Rays. *Phys. Rev. Lett.*, **13**:762, 1964.
- [19] Robert D. Cowan. Atomic Self-Consistent-Field Calculations Using Statistical Approximations for Exchange and Correlation. *Phys. Rev.*, **163**:54, 1976.
- [20] Robert D. Cowan. Theoretical Calculation of Atomic Spectra Using Digital Computers. *J. Opt. Soc. Am.*, **58**:808, 1968.
- [21] Charles R. Cowley. Yttrium, Barium, and the Lanthanides in AP and AM Stars. *Astr. Phys. J. Suppl. Series*, **32**:631, 1976.
- [22] A. Cummings, C. McGuinness, G. O'Sullivan, J. T. Costello, J. P. Mosnier, E. T. Kennedy. Wave-Function Collapse with Increasing Ionization 4d Photoabsorption of Cs through Cs⁴⁺. *Phys. Rev. A*, **63**:022702, 2001.
- [23] J. L. Dehmer, A. F. Starace. Potential-Barrier Effects in Photoabsorption: III. Application to 4d-Shell Photoabsorption in Lanthanum. *Phys. Rev. B*, **5**:1792, 1972.
- [24] M. Dolg, H. Stoll, A. Savin, H. Preuss. Energy-Adjusted Pseudopotentials for the Rare Earth Elements. *Theor. Chim. Acta*, **75**:173, 1989.
- [25] Henrik Kjeldsen. Photoionization Cross Sections of Atomic Ions from Merged-Beam Experiments. *J. Phys. B: At. Mol. Opt. Phys.*, **39**:R325, 2006.
- [26] S. S. Churilov and Y. N. Joshi. Analysis of the Sixth Spectrum of Cerium Ce VI. *J. Opt. Soc. Am. B*, **17**:2081, 2000.
- [27] Yu. Ralchenko, A. E. Kramida, J. Reader, and NIST ASD Team (2008). *NIST Atomic Spectra Database (version 3.1.5)*.
- [28] R. D. Cowan. Cowan Atomic Structure Code. <http://aphysics2.lanl.gov/cgi-bin/ION/runlanl.pl>.
- [29] R. Geller. Electron Cyclotron Resonance Ion Sources and ECR Plasmas. Institute of Physics Publishing, Bristol UK and Philadelphia USA, 1996.

- [30] M. Schlapp, R. Trassl, E. Salzborn, R.W. McCullough, T.K. McLaughlin, H.B. Gilbody. An Ultra Compact 10 Ghz Electron-Cyclotron-Resonance Ion Source (ECRIS) for Multiply Charged Ion Production. *Nucl. Inst. and Meth. B*, **98**:525–527, 1995.
- [31] U. Safronova. Hartree-Fock and RMBPT Calculations for Photoionization Cross Section of Cerium Ions in the 4d Region. *Unpublished*.
- [32] H. W. Kroto, J. R. Heath, S. C. O'Brien, R. F. Curl, and R. E. Smalley. C₆₀: Buckminsterfullerene. *Nature (London)*, **318**:162, 1985.
- [33] Y. Chai, T. Cuo, C. Jin, R. E. Haufler, L. P. Felipe Chibante, J. Fure, L. Wang, J. M. Alford, and R. E. Smalley. Fullerenes with Metal Inside. *J. Phys. Chem.*, **95**:7564, 1991.
- [34] A. Müller, S. Schippers, M. Habibi, D. Esteves, J. C. Wang, R. A. Phaneuf, A. L. D. Kilcoyne, A. Aguilar, and L. Dunsh. Significant Redistribution of Ce 4d Oscillator Strength Observed in Photoionization of Endohedral Ce@C₈₂⁺ Ions. *Phys. Rev. Lett.*, **101**:133001, 2008.
- [35] B. L. Henke, E. M. Gullikson, and J. C. Davis. *At. Data Nucl. Data Tables*, **54**:181, 1993.
- [36] H. Kjeldsen, P. Andersen, F. Folkman, J. E. Hansen, M. Kitajima, and T. Andersen. Experimental Study of 4f Wavefunction Contraction: 4d-Photoionization of Low-Charged Ions of I, Xe, Cs and Ba. *J. Phys. B: At. Mol. Opt. Phys.*, **35**:2845, 2002.
- [37] T. B. Lucatorto, T. J. McIlrath, J. Sugar, and S. M. Younger. Radical Redistribution of the 4d Oscillator Strength Observed in the Photoabsorption of the Ba, Ba⁺, and Ba⁺⁺ Sequence. *Phys. Rev. Lett.*, **47**:1124, 1981.
- [38] G. O'Sullivan, C. McGuinness, J. T. Costello, E. T. Kennedy, and B. Weinmann. Trends in 4d-subshell Photoabsorption Along the Iodine Isonuclear Sequence: I, I⁺, and I²⁺. *Phys. Rev. A*, **53**:3211, 1996.

- [39] W. Sato, K. Sueki, K. Kikuchi, K. Kobayashi, S. Suzuki, Y. Achiba, H. Nakahara, Y. Ohkubo, F. Ambe, and K. Asai. Electronic State of Ce@C₈₂. *J. Radioa. Nucl. Chem.*, **239**:187, 1999.
- [40] Scott E. Bisson, Brian Comaskey, Earl F. Worden. Method to Measure Excited-Level-to-Excited-Level Branching Ratios and Atomic Transition Probabilities by Time-Resolved Laser Photoionization Spectroscopy. *J. Opt. Soc. Am. B*, **12**:193, 1995.
- [41] S. W. J. Scully, E. D. Emmons, M. F. Gharaibeh, R. A. Phaneuf, A. L. D. Kilcoyne, A. S. Schlachter, S. Schippers, A. Müller, H. S. Chakraborty, M. E. Madjet, and J. M. Rost. *Phys. Rev. Lett.*, **94**:065503, 2005.
- [42] M. J. Seaton. Quantum Defect Theory. *Rep. Prog. Phys.*, **46**:167, 1983.
- [43] K. Muthukumar and J. A. Larsson. A Density Functional Study of Ce@C₈₂: Explanation of the Ce Preferential Bonding Site. *J. Phys. Chem. A*, **112**:1071, 2008.
- [44] R. Thissen, J. M. Bizau, C. Blancard, M. Coreno, C. Dehon, P. Franceschi, A. Giuliani, J. Lemaire, and C. Nicolas. Photoionization Cross Section of Xe⁺ Ion in the Pure 5p⁵ ²P_{3/2} Ground Level. *Phys. Rev. Lett.*, **100**:223001, 2008.
- [45] A. Aguilar, J. D. Gillaspay, G. F. Gribaken, R. A. Phaneuf, M. F. Gharaibeh, M. G. Kozlov, J. D. Bozek, and A. L. D. Kilcoyne. Absolute Photoionization Cross Sections for Xe⁴⁺, Xe⁵⁺, and Xe⁶⁺ near 13.5 nm: Experiment and Theory. *Phys. Rev. A*, **73**:032717, 2006.
- [46] R. D'Arcy, J. T. Costello, E. T. Kennedy, C. McGuinness, J. P. Mosnier, and G. OSullivan. The Evolution of 4d Photoabsorption in Sb with Increasing Ionization. *J. Phys. B: At. Mol. Opt. Phys*, **33**:1383, 2000.
- [47] H. Kjeldsen, P. Andersen, F. Folkmann, H. Knudsen, B. Kristensen, J. B. West, and T. Andersen. Absolute Photoionization Cross Sections of I⁺ and I²⁺ in the 4d Ionization Region. *Phys. Rev. A*, **62**:020702(R), 2000.

- [48] E. D. Emmons, A. Aguilar, M. F. Gharaibeh, S. W. J. Scully, R. A. Phaneuf, A. L. D. Kilcoyne, A. S. Schlachter, I. Álvarez, C. Cisneros, and G. Hinojosa. Photoionization and Electron-Impact Ionization of Xe^{3+} . *Phys. Rev. A*, **71**:042704, 2005.
- [49] Y. Itoh, A. Ito, M. Kitajima, T. Koizumi, T. M. Kojima, H. Sakai, M. Sano, and N. Watanabe. Absolute Photoionization Cross Section Measurements of Xe^+ Ions in the 4d Threshold Energy Region. *J. Phys. B: At. Mol. Opt. Phys.*, **34**:3493, 2001.
- [50] H. Kjeldsen, P. Andersen, F. Folkmann, J. E. Hansen, M. Kitajima, and T. Andersen. Experimental Study of 4f Wavefunction Contraction: 4d-Photoionization of Low-Charged Ions of I, Xe, Cs and Ba. *J. Phys. B: At. Mol. Opt. Phys.*, **35**:2845, 2002.
- [51] U. Köble, L. Kiernan, J. T. Costello, J-P. Mosnier, E. T. Kennedy, V. K. Ivanov, V. A. Kupchenko, and M. S. Shendrik. 4f(1P) Giant Dipole Resonance in La^{3+} . *Phys. Rev. Lett.*, **74**:12, 1995.
- [52] T. Koizumi, Y. Itoh, M. Sano, M. Kimura, T. M. Kojima, S. Kravist, A. Matsumoto, M. Oura, T. Sekioka, and Y. Awaya. Photoionization of Ba^+ Ions Due to Creation of 4d Hole States. *J. Phys. B: At. Mol. Opt. Phys.*, **28**:609, 1995.
- [53] T. Koizumi, Y. Awaya, M. Gonno, Y. Itoh, M. Kimura, T. M. Kojima, S. Kravis, M. Oura, M. Sano, T. Sekioka, Naoki Watanabe, H. Yamaoka, and F. Koike. 4d Photoionization of Singly-Charged Xe, Ba, and Eu Ions. *J. Elec. Spec. Rel. Phen.*, **79**:289, 1996.
- [54] T. M. Kojima, F. Chenb, M. Kitajima, T. Koizumi, Y. Nakaia, H. Yamaoka, and N. Watanabe. Observation of Resonance Structures in 4d Photoionization of Eu^+ . *J. Elec. Spec. Rel. Phen.*, **114-147**:71, 2005.
- [55] M. Sano, Y. Itoh, T. Koizumi, T. M. Kojima, S. D. Kravis, M. Oura, T. Sekioka, N. Watanabe, Y. Awaya, and F. Koike. Photoionization of 4d-Electrons in Singly Charged Xe Ions. *J. Phys. B: At. Mol. Opt. Phys.*, **29**:5305, 1996.

- [56] N. Watanabe, Y. Awaya, A. Fujino, Y. Itoh, M. Kitajima, T. M. Kojima, M. Oura, R. Okuma, M. Sano, T. Sekioka, and T. Koizumi. Photoion-Yield Spectra of Xe^{2+} in the 4d-Threshold Energy Region. *J. Phys. B: At. Mol. Opt. Phys.*, **31**:4137, 1998.
- [57] L. Becker, R. J. Poreda, and T. E. Bunch. Fullerenes: An Extraterrestrial Carbon Carrier Phase for Noble Gases. *Science*, **272**:249, 1996.
- [58] L. Becker, R. J. Poreda, A. G. Hunt, T. E. Bunch, and M. Rampino. Impact Event at the Permian-Triassic Boundary: Evidence from Extraterrestrial Noble Gases in Fullerenes. *Science*, **291**:1530, 2001.
- [59] E. E. B. Campbell, R. Rhlich, A. Hielscher, J. M. A. Frazao, and I. V. Hertel. Collision Energy Dependence of He and Ne Capture by C_{60}^+ . *Z. Phys. D-Atoms Mol. Clust.*, **23**:1, 1992.
- [60] B. H. Bransden and C. J. Joachain. Physics of Atoms and Molecules. (*Prentice Hall Harlow, England, 2003*), *Second Edition*.
- [61] U. Fano. Effects of Configuration Interaction in Intensities and Phase Shifts. *Phys. Rev.*, **124**:1866, 1961.
- [62] F. Broetz, R. Trassl, R. W. McCullough, W. Arnold, and E. Salzbom. Design of Compact All-Permanent Magnet Electron Cyclotron Resonance (ECR) Ion Sources for Atomic Physics Experiments. *Phys. Scripta*, **T92**:278, 2001.
- [63] R. Trassl, W. R. Thompson, F. Broetz, M. Pawlowsky, R. W. McCullough, and E. Salzbom. Development of a 10 GHz "Multi-Mode" ECR, Ion Source for the Production of Multiply Charged Ions from Metallic Elements. *Phys. Scripta*, **T80**:504, 1999.
- [64] Z. Q. Xie. State of the Art of ECR Ion Source. URL: <http://accelconf.web.cern.ch/AccelConf/pac97/papers/pdf/2C003.PDF>.
- [65] J. Schwinger. On the Classical Radiation of Accelerated Electrons. *Phys. Rev.*, **75**:1912, 1949.

- [66] URL: <http://www.als.lbl.gov/als/quickguide/vugraph.html>.
- [67] A. Aguilar. Photoionization of Positive Ions: the Nitrogen Isoelectronic Sequence. *Ph.D. Dissertation*, University of Nevada, Reno, 2003.
- [68] R. Trassl. Development of ECR Ion Sources. URL: http://www.strz.uni-giessen.de/ezr/english/10ghz_perm.html, 2002.
- [69] R. D. Cowan. Atomic Theory of Atomic Structure and Spectra. *University of California Press*, Berkeley, 1981.
- [70] G. C. Baldwin and G. S. Klaiber. Photo-Fission in Heavy Elements. *Phys. Rev.*, **71**:3, 1947.
- [71] G. C. Baldwin and G. S. Klaiber. X-Ray Yield Curves for γ -n Reactions. *Phys. Rev.*, **73**:1156, 1948.
- [72] A. P. Lukirskii and T. M. Zimkina. *Bull. Acad. Sci. USSR Phys. Ser.*, **27**:808, 1963.
- [73] J. P. Connerade, J. M. Esteve, and R. C. Karnatak, Ed. Giant Resonances in Atoms, Molecules, and Solids. *Plenum Press*, New York and London, 1987.
- [74] J. B. West and J. Morton. Absolute Photoionization Cross-Section Tables for Xenon in the VUV and the Soft X-Ray Regions. *At. Data Nucl. Data Tables*, **22**:103, 1978.
- [75] David Attwood. Soft X-Rays and Extreme Ultraviolet Radiation.
- [76] G. C. King, M. Tronc, F. H. Read, and R. C. Bradford. An Investigation of the Structure Near the $L_{2,3}$ Edges of Argon, the $M_{4,5}$ Edges of Krypton and the $N_{4,5}$ Edges of Xenon, Using Electron Impact with High Resolution. *J. Phys. B: Atom. Molec. Phys.*, **10**:2479, 1977.
- [77] M. Ya. Amusia. Photoionization and Vacancy Decay of Endohedral Atoms. *J. Elec. Spec. Rel. Phen.*, **161**:112, 2007.
- [78] A. M. Covington, A. Aguilar, I. R. Covington, M. F. Gharaibeh, G. Hinojosa, C. A. Shirly, R. A. Phaneuf, I. Álvarez. C. Cisneros, I. Dominguez-Lopez, M. M.

- Sant'Anna, A. S. Schlachter, B. M. McLaughlin and A. Dalgarno. Photoionization of Ne^+ Using Synchrotron Radiation. *Phys. Rev. A*, **66**:062710, 2002.
- [79] A. Müller, S. Schippers, R. A. Phaneuf, M. Habibi, D. Esteves, J. C. Wang, A. L. D. Kilcoyne, A. Aguilar, S. Yang and L. Dunsch. Photoionization of the Endohedral Fullerene Ions $\text{Sc}_3\text{N@C}_{80}^+$ and Ce@C_{82}^+ by Synchrotron Radiation *J. Phys.: Conf. Ser.*, **88**:012038, 2007.

1

Publications

During the period of this research project, I have had the opportunity to be involved in several experiments conducted at the ALS about which many papers were published. The following is a complete list of those publications in chronological order.

1. “photoionization cross section for Ce^{4+} : experiment and theory”, M. Habibi, R. A. Phaneuf, D. Esteves, U. I. Safronova, A. Aguilar, A. L. D. Kilcoyne, C. Cisneros, and I. M. Savukov. *In progress*.
2. “Significant redistribution of Ce 4d oscillator strength observed in photoionization of endohedral $\text{Ce}@\text{C}_{82}^+$ ions”, A. Müller, S. Schippers, M. Habibi, D. Esteves, J. C. Wang, R. A. Phaneuf, A. L. D. Kilcoyne, A. Aguilar and L. F. Dunsch. *Phys. Rev. Lett.*, **101**:133001, 2008.
3. “Photoionization of the endohedral fullerene ions $\text{Sc}_3\text{N}@\text{C}_{80}^+$ and $\text{Ce}@\text{C}_{82}^+$ by synchrotron radiation”, A. Müller, S. Schippers, R. A. Phaneuf, M. Habibi, D. Esteves, J. C. Wang, A. L. D. Kilcoyne, A. Aguilar, S. Yang and L. Dunsch. *J. Phys.: Conf. Ser.*, **88**:012038, 2007.
4. “Photoionization and electron-impact ionization of Ar^{5+} ”, Jing Cheng Wang, M. Lu, D. Esteves, M. Habibi, G. Alna’washi, R. A. Phaneuf, and A. L. D. Kilcoyne. *Phys. Rev. A*, **75**:062712, 2007.
5. “Photoionization and electron-impact ionization of Kr^{3+} ”, M. Lu, G. Alna’washi, M. Habibi, M. F. Gharaibeh, R. A. Phaneuf, A. L. D. Kilcoyne, E. Levenson, A.

S. Schlachter, C. Cisneros and G. Hinojosa. *Phys. Rev. A*,**74**:062701, 2006.

The first three papers are the most relevant publications to this dissertation.

Significant Redistribution of Ce 4*d* Oscillator Strength Observed in Photoionization of Endohedral Ce@C₈₂⁺ Ions

A. Müller,¹ S. Schippers,¹ M. Habibi,² D. Esteves,² J. C. Wang,² R. A. Phaneuf,² A. L. D. Kilcoyne,³
A. Aguilar,³ and L. Dunsch⁴

¹*Institut für Atom- und Molekülphysik, Justus-Liebig-Universität, 35392 Giessen, Germany*

²*Department of Physics, MS 220, University of Nevada, Reno, Nevada 89557-0058, USA*

³*Advanced Light Source, Lawrence Berkeley National Laboratory, MS 7-100, Berkeley, California 94720, USA*

⁴*Leibniz-Institut für Festkörper- und Werkstofforschung Dresden, D-01171 Dresden, Germany*

(Received 4 June 2008; published 24 September 2008)

Mass-selected beams of atomic Ce^{*q*+} ions (*q* = 2, 3, 4), of C₈₂⁺ and of endohedral Ce@C₈₂⁺ ions were employed to study photoionization of free and encaged cerium atoms. The Ce 4*d* inner-shell contributions to single and double ionization of the endohedral Ce@C₈₂⁺ fullerene have been extracted from the data and compared with expectations based on theory and the experiments with atomic Ce ions. Dramatic reduction and redistribution of the ionization contributions to 4*d* photoabsorption is observed. More than half of the Ce 4*d* oscillator strength appears to be diverted to the additional decay channels opened by the fullerene cage surrounding the Ce atom.

DOI: 10.1103/PhysRevLett.101.133001

PACS numbers: 32.80.Fb, 33.80.Eh, 36.40.Cg

Since the discovery of endohedral La@C₆₀ fullerene [1] the concept of an atom inside a fullerene molecule has fascinated chemists and physicists alike. Encapsulating an atom within a sphere of subnanometer size is of highest fundamental and applied interest. Endohedral fullerenes [2] have thus stimulated the imaginations of researchers from many different fields concerning what could happen to an atom in the unique environment of a carbon cage. New possibilities for applications in nanostructure science and technology are being vigorously explored. For example, confinement within a fullerene could have some unique advantages in isolating an atom from its environment, thereby providing a building block for the qubits of a quantum computer [3]. The chemical isolation of reactive and poisonous atoms may also open up new possibilities in medical imaging and cancer therapy [4,5].

Numerous theoretical studies have explored the response of atoms encapsulated in fullerene cages to ionizing electromagnetic radiation. While there are almost no experimental results available for endohedral molecules in the gas phase, theoretical work flourishes without constraints [6]. Clearly, experiments are needed to test and guide the theoretical developments; however, measurements with free endohedral molecules in the gas phase are almost prohibitively difficult. Challenges include the availability of sufficient amounts of target material for gas phase experiments and the purity of the samples to be investigated. Obtaining absolute cross sections for interactions of endohedral species with any kind of radiation is presently close to impossible. The only gas phase experiments with endohedral fullerenes reported to date were conducted by Mitsuke and co-workers on vapors of Ce@C₈₂ [7], Dy@C₈₂ [8] and Pr@C₈₂ [9] exposed to synchrotron light. Cross sections for photoionization with different exit channels have been inferred and evidence

was claimed for oscillations as predicted in the 4*d* – 4*f* atomic inner-shell contributions to photoionization of Xe@C₆₀ [6].

The present experiment employs a different approach to overcome problems with the characterization of the endohedral fullerene target and with quantifying its properties. Evaporated fullerenes are efficiently ionized in a low-power plasma of an electron cyclotron resonance (ECR) ion source. The ions are extracted and accelerated by several kV and a beam with defined particle energies is formed. Mass selection by a subsequent dipole magnet provides the desired ion species in the form of a well-characterized fullerene ion beam which then serves as the target for a beam of synchrotron radiation from undulator beam line 10.0.1 of the Advanced Light Source (ALS) in a merged beam geometry. The merged-beams technique for photon-ion interactions is well established [10] and can provide absolute cross sections taking advantage of the availability of energetic projectile and target beams in the experiments. Density profiles and intensities are readily measured for such beams and complete registration of product ions in a suitable detector can be ensured [11]. Different product ion beams are dispersed by a second dipole analyzing magnet and a subsequent electrostatic spherical 90° deflector, thereby sorted with respect to their energy, mass and charge state. By using merged beams, many systematic problems with measurements on static neutral endohedral species can be avoided. However, the availability and sufficient quantities of the desired species remain a problem. Efficient production and purification processes of the endohedral fullerenes [2] have to be combined with high ion yield from dilute vapors (~10⁻⁶ hPa), high detection probabilities (close to 100%) and low levels of detector background [12]. For the present experiments cerium fullerene soot was prepared by a standard arc

burning process [13]. Given the mass separation capability of the photoionization experiment, the purification process was limited to the 20% level of the Ce@C₈₂ component. Milligram quantities of endohedral Ce@C₈₂ fullerenes were sufficient to provide picoAmpere ion currents continuously over several days.

The goal of the present experiment was to investigate possible differences in the behavior of free and of caged atomic ions exposed to monochromatic ultraviolet radiation, a topic that is presently of utmost interest [14,15]. In particular, the decay of 4*d* vacancies in the encapsulated cerium is the focus of the present study, relating to theoretical considerations recently summarized by Amusia [6]. For the purpose of comparison, cross sections for single and double photoionization of Ce@C₈₂⁺, C₈₂⁺ as well as of Ce²⁺, Ce³⁺, and Ce⁴⁺ ions were determined.

One of the first questions to be answered when studying metal atoms encapsulated within a fullerene is that of the valence state of the atom in the reductive environment of the cage. Previous investigations showed that the cerium atom in Ce@C₈₂ is trivalent [16]. As a result, the endohedral fullerene, although electrically neutral as a whole, can be described as Ce³⁺@C₈₂³⁻. A recent density functional study [17] explains details of the charge transfer from and to the different subshells of the cerium atom within Ce@C₈₂ and provides an explanation to the preferential Ce off-center bonding site on the inner surface of the carbon sphere. Since the present object of investigation is the singly charged Ce@C₈₂⁺ ion, the effective charge state of the encaged Ce atom might be higher than *q* = +3. Therefore, several charge states of atomic Ce were included in this study. Photoionization of Ce atoms and low charge ions is dominated by resonance features associated with excitation of the 4*d* shell [10]. Modification of the cross section of the Ce@C₈₂⁺ ion by the encapsulated Ce atom is to be expected, especially in the energy region of 4*d* → *nl* resonances. The photon energy range covered in the experiments was between 17 eV and about 190 eV depending on the observable signals. Photon energy spreads were below 0.5 eV. Special attention was devoted to the energy range 80 to 190 eV where the 4*d* spectral fingerprints of cerium occur.

Mass spectra recorded for the endohedral fullerene ion beam showed that Ce@C₈₂⁺ ions with mass number 1124 could not be completely separated from C₉₄⁺ with mass number 1128. By increasing the resolution of the analyzer, i.e., by narrowing slits, the contamination of the primary ion beam could be estimated to be about 25%. Considering the presence of an admixture to the parent ion beam and the fact that measurements of cross sections at the low ion currents available for the measurements imply large uncertainties of at least 30%, the experimental data were normalized to scaled cross sections for C₆₀⁺ ions obtained with the identical apparatus [18]. At energies from about 50 eV up to the carbon *K*-shell threshold the measurements

for single ionization of C₆₀⁺ ions are found [19] to have an energy dependence as predicted by the Henke model [20] where the photoabsorption of a molecule is just given by the sum of the cross sections for each single atom in the molecule. For C₆₀ this implies 60 times the absorption of a carbon atom. The cross sections found for single ionization of C₆₀⁺ are 12% below the absorption cross section predicted by the model calculation. Previous experiments with higher fullerenes [19] agreed with the prediction that cross sections of empty fullerenes scale with the number of carbon atoms. Hence, the expected cross section for the empty C₈₂ is 82/60 times that of C₆₀ and, accordingly, the measured yields for single ionization of C₈₂⁺ and of Ce@C₈₂⁺ were normalized to the expectation in the energy range 80 to 100 eV where cerium does not significantly contribute. Much care was taken to measure the ratios of double versus single ionization cross sections for both the endohedral and the empty-fullerene ion, thus providing the basis for normalizing the double-ionization yields to the scaled C₆₀⁺ results.

Figure 1 shows the cross sections obtained for single and double ionization of Ce@C₈₂⁺ ions together with data for single ionization of the empty C₈₂⁺ fullerene ion. The cross section for the empty cage ion is smooth in the present

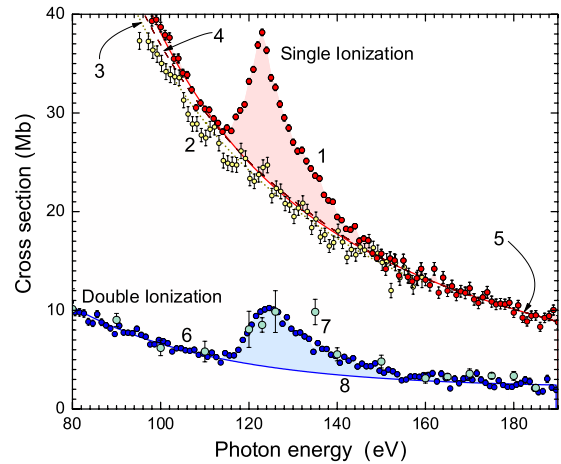


FIG. 1 (color online). Cross sections $\sigma_{i,j}$ for photoionization from initial charge state *i* to final charge state *j* in the energy region of Ce 4*d* excitation: (1) $\sigma_{1,2}$ of Ce@C₈₂⁺; (2) $\sigma_{1,2}$ of C₈₂⁺; (3) $\sigma_{1,2}$ of C₆₀⁺ scaled from results for C₆₀⁺ (see text); (4) scaled $\sigma_{1,2}$ of Ce@C₈₂⁺ accounting for a 25% contamination of the parent ion beam with C₉₄⁺; (5) fit curve representing the empty-fullerene background under the Ce 4*d* contribution to single ionization of Ce@C₈₂⁺; (6) scan measurement of $\sigma_{1,3}$ of Ce@C₈₂⁺ normalized to (7), i.e., data points (with larger error bars) obtained from measured cross section ratios $\sigma_{1,2}/\sigma_{1,3}$ and the normalized data set (1); (8) fit curve representing the empty-fullerene background under the Ce 4*d* contribution to double ionization of Ce@C₈₂⁺. Error bars are statistical only.

energy range of interest which is also true for the double ionization (not shown). Because of the 25% contamination of the primary $\text{Ce}@C_{82}^+$ ion beam, the expected “background” corresponding to 75% C_{82}^+ and 25% C_{94}^+ is enhanced by only 3.7% (curve 4 in Fig. 1). The effects of $4d$ excitation of the encapsulated cerium atom on the ionization cross sections of $\text{Ce}@C_{82}^+$ are clearly seen.

For clarification of the valency of the Ce atom residing within the $\text{Ce}@C_{82}^+$ ion, data obtained for single ionization of atomic Ce^{2+} , Ce^{3+} and Ce^{4+} are compared in Fig. 2 with the Ce $4d$ excess cross section in single ionization of the endohedral $\text{Ce}@C_{82}^+$ ions. The difference between the data set (1) in Fig. 1 and the background fit (curve 5) was divided by the fraction (0.75) of $\text{Ce}@C_{82}^+$ ions in the parent beam. The excess cross section is relatively structureless indicating the hybridization of the outer levels of the Ce atom and the fullerene cage and the resulting increase of resonance widths. In spite of this difference, the comparison clearly shows the best match of resonance energies for the endohedral Ce atom with $\sigma_{3,4}$ for atomic Ce^{3+} . As in the neutral $\text{Ce}@C_{82}$ molecule the valency of Ce in the $\text{Ce}@C_{82}^+$ ion is 3. A similar comparison for double ionization of the same ions with the best match for Ce^{3+} confirms this conclusion.

For atomic Ce^{3+} ions, photoabsorption in the present energy range is expected to be dominated by $4d$ -shell excitations resulting in single and double ionization of the absorbing ion. Triple ionization with a threshold near 180 eV is energetically not allowed and radiative stabilization of a $4d$ vacancy can be neglected. On that basis one would expect a total oscillator strength f_a of 10 for the absorption by ten $4d$ electrons. Integration of the cross section sum $\sigma_{3,4} + \sigma_{3,5}$ for Ce^{3+} ions (see the upper chain

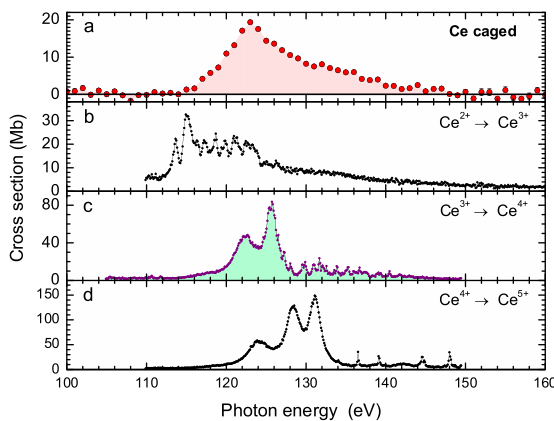


FIG. 2 (color online). Comparison of absolute cross sections for single photoionization of atomic Ce^{q+} ions $q = 2$ (b), $q = 3$ (c), $q = 4$ (d) with the excess cross section (a) obtained by subtracting curve (5) in Fig. 1 from the data set (1) and correcting for the contamination of the parent ion beam.

curve in Fig. 3) in the energy range 100 to 170 eV yields $f_a = 8.5$. With the limitation of the integration range, a possible small contribution of fluorescence stabilization and the expected total uncertainty of the ionization cross sections for atomic Ce^{3+} of at least 20% the total experimental oscillator strength is in good agreement with the expectation. In strong contrast to that, absorption by the encapsulated Ce atom involving $4d$ excitation and subsequent ionization is much smaller (see Fig. 3). The excess cross sections for single and double ionization of the endohedral fullerene obtained from Fig. 1 and their sum are much smaller than the corresponding data for atomic Ce^{3+} . Integration over the investigated energy range is shown by the lower chain curve in Fig. 3. The difference is more than a factor of 2. Integration of the endohedral data to 180 eV results in $f_a = 3.6$, i.e., only 36% of the expected total oscillator strength or 42% of the number observed in photoionization of Ce^{3+} . The missing strength cannot be explained by uncertainties in the normalization procedures used here. Actually, the total absorption expected for 82 carbon atoms must be considered an upper limit for the empty-endohedral background ionization cross section. In that respect, the derived Ce $4d$ contributions to single and double ionization of endohedral $\text{Ce}@C_{82}^+$ are also at their upper limits. Apparently, $4d$ vacancy decay via autoionizing channels is greatly sup-

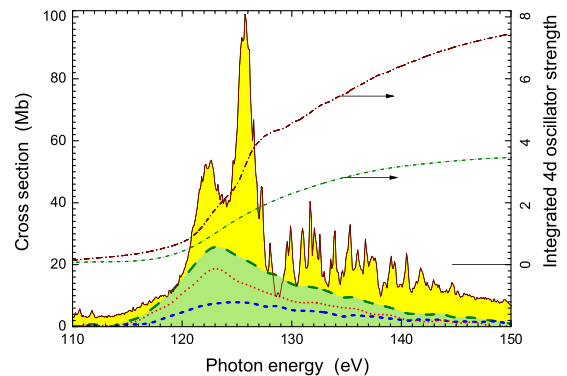


FIG. 3 (color online). Cross sections and integrated oscillator strengths for photoionization of atomic Ce^{3+} ions and for the Ce $4d$ contributions to single and double ionization of $\text{Ce}@C_{82}^+$. Solid (brown) line with shading (yellow): $\sigma_{3,4} + \sigma_{3,5}$ for Ce^{3+} ; long-dashed (green) line with shading (light green): sum of the Ce $4d$ contributions to single ionization, represented by the dotted (red) line, and double ionization of $\text{Ce}@C_{82}^+$, represented by the short-dashed (blue) line. The chain curves correspond to the oscillator strength scale on the right (note the offset). The upper (brown) curve is the energy-integrated total absorption oscillator strength of Ce^{3+} in the energy region of $4d$ excitations, and the lower (green) curve results from the integration of the long-dashed (green) curve, i.e., from the $4d$ contributions to single and double ionization of $\text{Ce}@C_{82}^+$.

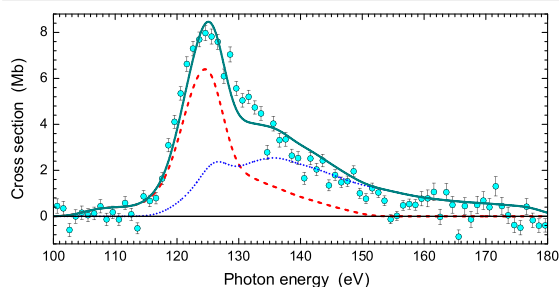


FIG. 4 (color online). Cross section [(cyan) shaded circles with statistical error bars] for the Ce $4d$ contribution to double ionization of Ce@C_{82}^+ obtained by subtracting curve (8) from the data set (6) shown in Fig. 1. The dashed (red) curve is the cross section $\sigma_{3,4}$ for atomic Ce^{3+} convoluted with a 5-eV Gaussian and multiplied by a factor 0.15, the dotted (blue) curve is the cross section $\sigma_{3,5}$ for atomic Ce^{3+} convoluted with a 5-eV Gaussian and multiplied by a factor 0.22. The solid (dark cyan) line is the sum of the two latter curves.

pressed for Ce^{3+} encapsulated inside a fullerene cage relative to free Ce^{3+} .

Since the cage of the endohedral fullerene is transparent to the incident EUV photons, one has to conclude that most of the absorption oscillator strength of the $4d$ electrons in the encapsulated Ce is diverted to decay channels other than net single and double ionization which were isolated and individually observed in the present experiment. A test measurement showed that triple ionization, though energetically possible in the endohedral fullerene, does not significantly contribute to the total $4d$ absorption cross section. It is hypothesized that the most likely additional decay channels for the relaxation of the Ce $4d$ vacancy in the endohedral Ce@C_{82}^+ ions opened up by the presence of the fullerene cage are related to ionization with fragmentation. First evidence for this hypothesis was obtained by observing a Ce $4d$ enhancement in the photo-ion yield of mass/charge separated Ce@C_{28}^{2+} produced from the parent Ce@C_{82}^+ beam.

In an attempt to quantify the $4d$ suppression for single and double ionization of Ce@C_{82}^+ the cross sections for atomic Ce^{3+} ions were convoluted with a 5 eV Gaussian which appears to give a reasonable representation of the smearing effect of the hybridization in the endohedral system. It turns out that 45% of the resulting convoluted cross section $\sigma_{3,4}$ gives a fairly good representation of the measured $4d$ single ionization contribution in Ce@C_{82}^+ (the dotted curve in Fig. 3), which is well compatible with the overall 42% of the total absorption contribution. Trying the same with double ionization immediately shows that the measured 5-eV Gaussian-convoluted cross section $\sigma_{3,5}$ (dotted curve in Fig. 4) contributes only 22% to the inferred $4d$ double-ionization contribution (short-dashed line

in Fig. 3 and circles in Fig. 4) in Ce@C_{82}^+ . Reasonable agreement with the measured $4d$ double-ionization function is only obtained by including an additional 15% contribution of the 5-eV Gaussian-convoluted cross section $\sigma_{3,4}$ (dashed curve in Fig. 4). This redistribution of partial oscillator strengths is a consequence of “post-decay” interactions of the ejected Auger electrons with the fullerene cage. Possibilities are electron scattering, electron capture, electron-impact ionization and fragmentation subsequent to ionization of the encapsulated Ce atom.

In summary, clear spectral fingerprints of $4d$ excitation of Ce atoms encapsulated in a fullerene have been observed both in single and double photoionization. For the first time, the anticipated redistribution of decay probabilities of a caged atom versus its free counterpart has been clearly demonstrated. Detailed energy-dependent information has been obtained on the effects of the electrons ejected from the encapsulated atom on the surrounding carbon sphere.

This research was funded by the Office of Basic Energy Sciences of the U.S. Department of Energy and by the Deutsche Forschungsgemeinschaft. Thanks go to Christian Kästner for his work in the fullerene production.

- [1] Y. Chai *et al.*, *J. Phys. Chem.* **95**, 7564 (1991).
- [2] L. Dunsch and S. Yang, *Small* **3**, 1298 (2007).
- [3] W. Harnett *et al.*, *Phys. Rev. Lett.* **98**, 216601 (2007).
- [4] C.-Y. Shu *et al.*, *Bioconjugate Chemistry* **19**, 651 (2008).
- [5] K. B. Hartman, L. J. Wilson, and M. G. Rosenblum, *Molecular Diagnosis & Therapy* **12**, 1 (2008).
- [6] M. Ya. Amusia, *J. Electron Spectrosc. Relat. Phenom.* **161**, 112 (2007).
- [7] K. Mitsuke *et al.*, *J. Chem. Phys.* **122**, 064304 (2005).
- [8] K. Mitsuke *et al.*, *Int. J. Mass Spectrom.* **243**, 121 (2005).
- [9] H. Katayanagi *et al.*, *J. Quant. Spectrosc. Radiat. Transfer* **109**, 1590 (2008).
- [10] H. Kjeldsen, *J. Phys. B* **39**, R325 (2006).
- [11] A. M. Covington *et al.*, *Phys. Rev. A* **66**, 062710 (2002).
- [12] A. Müller *et al.*, *J. Phys. Conf. Ser.* **88**, 012038 (2007).
- [13] L. Dunsch *et al.*, *Synth. Met.* **121**, 1113 (2001).
- [14] V. Averbukh and L. S. Cederbaum, *Phys. Rev. Lett.* **96**, 053401 (2006).
- [15] M. E. Madjet, H. S. Chakraborty, and S. T. Manson, *Phys. Rev. Lett.* **99**, 243003 (2007).
- [16] W. Sato *et al.*, *J. Radiol. Nucl. Chem.* **239**, 187 (1999).
- [17] K. Muthukumar and J. A. Larsson, *J. Phys. Chem. A* **112**, 1071 (2008).
- [18] S. W. J. Scully *et al.*, *Phys. Rev. Lett.* **94**, 065503 (2005).
- [19] A. Müller *et al.*, in *Latest Advances in Atomic Cluster Collisions*, edited by J.-P. Connerade and A. V. Solov'yov [Imperial College Press, London, (to be published)].
- [20] B. L. Henke, E. M. Gullikson, and J. C. Davis, *At. Data Nucl. Data Tables* **54**, 181 (1993).